UCLouvain

FACULTE DES SCIENCES

Faculté des sciences

Impact of a decrease in the intensity of deep ocean circulation in the North Atlantic on the climate of Western Europe

Mémoire présenté en vue de l'obtention du grade académique de Master [60] en sciences physiques

Auteur : Mathéo Ketels
Promoteur : Prof. Hugues Goosse
Lecteurs : Prof. François Massonnet, Prof. Thierry Fichefet
École de Physique
Année académique 2025 - 2026

Abstract

The Atlantic Meridional Overturning Circulation (AMOC) plays a fundamental role in shaping European climate through northward heat transport, while European atmospheric circulation is strongly regulated by the North Atlantic Oscillation (NAO). Using the Canadian Earth System Model version 5 (CanESM5) under the NAHosMIP framework, this thesis examines the influence of the NAO on European temperatures under AMOC weakening and the physical mechanisms governing the changes in European temperature standard deviation. The findings reveal that an AMOC decline causes widespread continental cooling (from -1.17°C to -2.62°C on average), which is most severe across Northern Europe and during winter. Under this low-AMOC state, the relative contribution of the NAO to European temperatures increases substantially, with its influence becoming especially dominant during winter over Northern Europe. Negative NAO phases amplify this cooling via expanded sea ice and displaced thermal gradients, while positive phases dampen it. The NAO contribution to European temperatures becomes more important under AMOC weakening. Furthermore, a weakened AMOC enhances North Atlantic temperature standard deviation in regions similar to those of sea ice expansion and to the southward shift of thermal gradients, affecting the Northern European region and the winter season as well. An advection analysis shows this increase to be thermodynamically driven by increased horizontal temperature gradient fluctuations rather than wind volatility. These results demonstrate that European temperatures under low-AMOC state are governed by coupled interactions between oceanic heat transport, atmospheric circulation, and sea ice feedback.

Acknowledgements

I feel deeply grateful to my family and friends who supported me in completing this thesis.

I would also like to express my sincere thanks to my supervisor, Professor Hugues Goosse, for offering me the opportunity to work on such an interesting topic, as well as for his availability and invaluable advice throughout this past year. Additionally, I would like to thank researchers Cécile Davrinche and Shivangi Tiwari for their technical support and constant availability.

This last year has been an exciting learning experience at the School of Physics, marking the completion of six years of study at UCLouvain, an adventure I won't soon forget.

Use of AI

AI tools such as Gemini and Claude have been used to improve the quality of the writing, to better understand the CanESM5 database, and to plot numerical data provided by the models with Python scripts.

AI has always been used with a critical eye regarding the information provided.

Contents

1 Introduction **4**

2 State of the Art **6**
2.1 Atlantic Meridional Overturning Circulation 6
2.1.1 General dynamics 7
2.1.2 AMOC variability 8
2.1.3 AMOC stability 9
2.2 North Atlantic Oscillation 12
2.3 Baroclinic instabilities 13
2.4 Impact of the AMOC weakening 14

3 Materials and methods **16**
3.1 Experimental Design: NAHosMIP 16
3.2 Model Description: CanESM5 17
3.3 Statistical Approach and Variables 18
3.4 Model validation 20

4 Results **24**
4.1 Experiments and Global View 24
4.1.1 European Climate under low-AMOC state 26
4.2 NAO contribution 31
4.2.1 Linear temperature model 40
4.3 Temperature volatility in Europe 45
4.3.1 Temporal volatility analysis 46
4.3.2 Spatial volatility analysis 51
4.3.3 Advection volatility analysis 54
4.4 Schematic summary 65

5 Conclusions **66**

A Nomenclature **68**

B Additional graphs **69**

Bibliography **88**

Chapter 1

Introduction

Since the Industrial Revolution, human activities have continuously increased the concentration of greenhouse gases in the atmosphere, especially CO_2, which drives a global rise in surface air temperatures (IPCC 2021 [1]). However, this warming is not uniform across the globe. While most of the planet warms, a distinct region in the subpolar North Atlantic has shown a cooling anomaly, commonly known as the "cold blob" (Rahmstorf 2024 [2]). Although this phenomenon is not yet fully understood, the main hypothesis is that it results from a decrease in the intensity of the Atlantic Meridional Overturning Circulation (AMOC).

The AMOC is a large-scale oceanic circulation system that transports warm, salty water northward at the surface and returns cold, dense water southward at depth. By carrying approximately 1.2 PW of heat northward at 26.5°N, the AMOC releases significant heat into the atmosphere, making Western Europe and the North Atlantic region much warmer than they would be otherwise (Rahmstorf 2024 [2], Johns et al. 2023 [3], Jackson et al. 2022 [4]). Geological proxy records show that a slowdown or shutdown of this circulation has already triggered massive climate perturbations in Earth's history, such as during Heinrich Event 1 in the last deglaciation (Otto-Bliesner and Brady. 2010 [5], Liu et al. 2015 [6]). Furthermore, a future collapse or weakening of the AMOC could produce a chain reaction across other major systems, such as the oceanic carbon sink, global precipitation and sea level (Frajka-Williams et al. 2019 [7], Jackson et al. 2015 [8]). Given these potential consequences, studying the mechanisms and impacts of an AMOC weakening is crucial.

More specifically, this thesis focuses on the thermal response across the European continent. While many studies have analyzed the direct impact of the AMOC on North Atlantic sea surface temperatures, atmospheric circulation over this region is strongly governed by the North Atlantic Oscillation (NAO) and is rarely linked to European temperatures. Simulations from the Canadian Earth System Model version 5 (CanESM5) under the North Atlantic Hosing Model Intercomparison Project (NAHosMIP) framework show key interactions between the NAO and European temperatures. Accordingly, this work investigates how the AMOC and NAO couple to drive European temperature variations on decadal timescales.

To provide a comprehensive assessment, this study also investigates changes in temperature standard deviation to evaluate climate volatility under a weakened AMOC. Using a temperature advection framework, the physical sources of standard deviation anomalies are analyzed to distinguish between dynamical contributions from geostrophic wind variations and thermodynamical contributions driven by changes in horizontal temperature gradients.

The primary objective of this thesis is to evaluate the European climate response to an AMOC weakening, based on simulations from the CanESM5 model within the NAHosMIP framework. Specifically, this work addresses two central research questions:

- How does the influence of the NAO on European temperatures vary with AMOC strength on decadal timescales?
- What physical mechanisms govern changes in European temperature standard deviation under a weakened AMOC state?

Chapter 2

State of the Art

2.1 Atlantic Meridional Overturning Circulation

This first section focuses on the dynamics of Atlantic circulation, which plays a crucial role in the climate of Western Europe. Consequently, this section will primarily concern the Northern Hemisphere, even though the overturning circulation influences the Southern Hemisphere climate as well. The Atlantic Meridional Overturning Circulation (AMOC), illustrated in Figure 2.1, constitutes the central physical system analyzed in this thesis. The AMOC is composed of a northward flow of warm surface water and a southward return flow of cold deep water, connected through overturning regions in the Nordic Seas. The AMOC transports a substantial amount of heat which is delivered all the way up to the region of south Greenland and Iceland. The heat released into the atmosphere makes certain North Atlantic regions, such as Europe, much warmer for their latitude than they would otherwise be (Rahmstorf 2024 [2]). At 26.5°N, the Atlantic Ocean circulation carries about 1.2PW (1PW = 10^{15}W) of heat northward. This represents approximately 60% of the net poleward heat flux carried by the global oceans and 30% of the total flux transported by the ocean and the atmosphere at this latitude (Johns et al. 2023 [3], Jackson et al. 2022 [4]).

The AMOC also plays an essential role in transporting carbon and nutrients across the global ocean. The overturning circulation forms a critical carbon sink through two primary mechanisms, the solubility pump and the biological pump. The solubility pump relies on the fact that cold water can dissolve significantly more CO_2 than warm water. This temperature dependence is governed by Henry's Law, as warm waters flow northward and release heat into the atmosphere, their molecular kinetic energy decreases. This cooling allows gas molecules to remain bound within the water rather than escaping back into the air.

Once dissolved at the ocean-atmosphere interface, the CO_2 follows a chemical chain reaction 2.1.

$$\begin{aligned} CO_{2(g)} &\rightleftharpoons CO_{2(aq)} \\ CO_{2(aq)} + H_2O &\rightleftharpoons H_2CO_3 \\ H_2CO_3 &\rightleftharpoons H^+ + HCO_3^- \\ HCO_3^- &\rightleftharpoons H^+ + CO_3^{2-} \end{aligned} \tag{2.1}$$

At the same time, this vertical overturning dynamic drives nutrients up to the surface layer, where phytoplankton assimilate these nutrients along with dissolved inorganic carbon to perform photosynthesis. Furthermore, phytoplankton utilize the products of the carbonate ions

(CO_3^{2-}) and combine them with calcium (Ca^{2+}) to construct protective calcium carbonate ($CaCO_3$) shells (Frajka-Williams et al. 2019 [7], Schaumann and Asenjo 2025 [9], Doney et al. 2009 [10]).

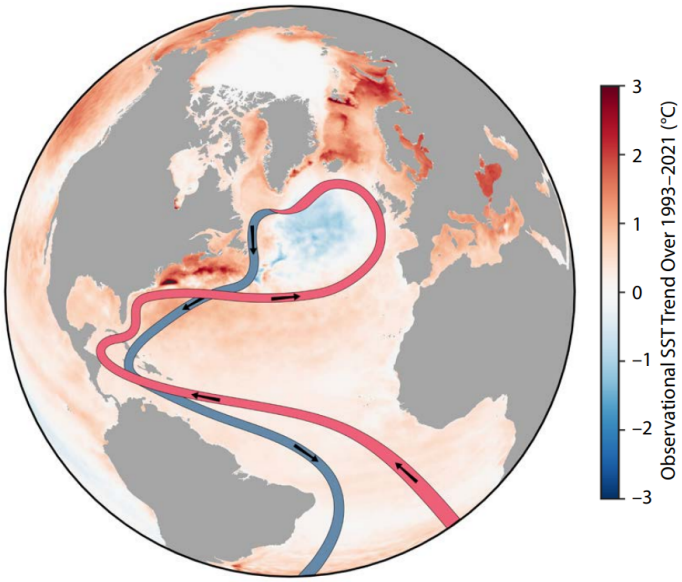


Figure 2.1: A schematic of a highly simplified AMOC and the sea surface temperature trend from 1993 to 2021 [2].

While the AMOC is central to this study due to its profound influence on global climate, its impact extends across multiple Earth system domains. Beyond regulating atmospheric climate patterns, the AMOC plays a vital role in the wider Earth system by redistributing ocean nutrients, driving global carbon cycles, and sustaining marine ecosystems.

Key empirical evidence that the AMOC may be weakening arises from observed sea surface temperatures in the subpolar North Atlantic. While almost the entire North Atlantic has warmed since 1900, this particular region (known as the "cold blob") has cooled, as shown in Figure 2.1. A broad scientific consensus attributes localized cooling to a reduction in oceanic heat transport (OHT) associated with a decline in AMOC intensity. However, a recent study suggests that radiative processes may also contribute to the cold blob's formation (Fan et al. 2024 [11]). Even though direct measurements have not yet captured a clear long-term decline, the emergence of the cold blob, supported by climate model simulations, provides warning indicators that the circulation may be weakening.

2.1.1 General dynamics

The main driving factor of the AMOC is water density, which is modulated by sea surface temperature (SST) and sea surface salinity (SSS). For this reason, the AMOC is also called a thermohaline circulation. This circulation is driven by deep convection occurring at high latitudes in the North Atlantic, which plays a central role in setting abyssal ocean properties such as heat and carbon storage (Patara and Böning 2014 [12], Bil´o et al. 2024 [13]) as well as meridional ocean heat transport (Johns et al. 2023 [3]). The SSS is strongly related to freshwater fluxes. A net inflow of freshwater (from rivers, precipitation, ice melting, etc) dilutes the salt present in the water and decreases its salinity, whereas net evaporation removes

freshwater from the surface thereby increasing salinity. In the subtropics, surface waters are warmer and saltier than at higher latitudes. As it flows northward, the AMOC transfers heat into the atmosphere. The SST gradually decreases, and the surface water density increases (Rahmstorf 2024 [2]). Although salinity slightly decreases due to precipitation, as shown in Figure 2.2 (Trenberth et al. 2007 [14]), the surface water remains dense enough to sink once it reaches the Nordic Seas and the Labrador Sea. This process drives the formation of North Atlantic Deep Water (NADW), thereby sustaining the *overturning* circulation.

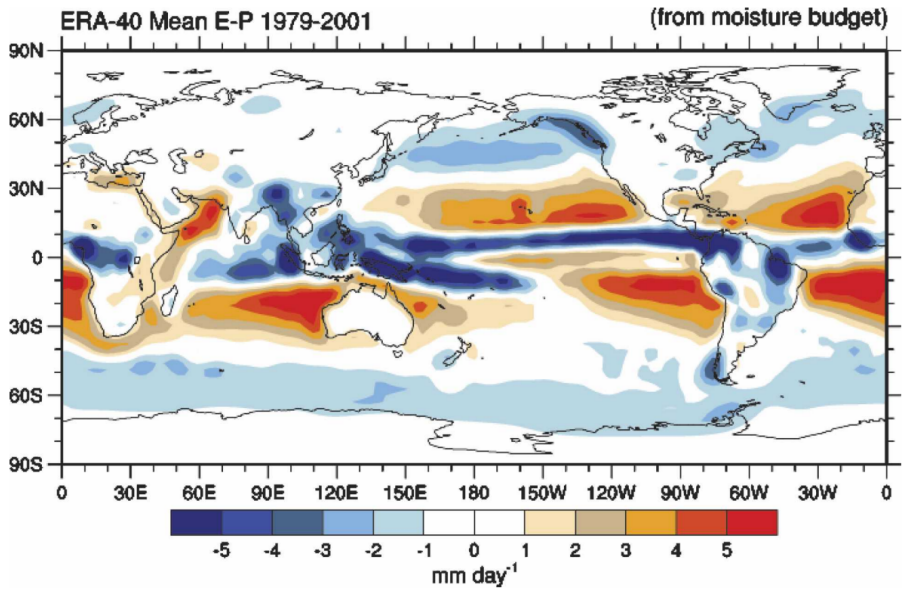


Figure 2.2: The long-term 1979–2001 annual mean of $E - P$ (Evaporation minus Precipitation) budget based on ERA-40 reanalyses. The major features of the E-P budget are represented on this figure, but because of large uncertainties, the values displayed should not be considered as quantitatively exact [14].

2.1.2 AMOC variability

The RAPID array provides a long-term observational record of the AMOC strength at 26.5°N. During the 2004–2022 period, its mean transport was 16.9Sv (1Sv=$10^6 m^3/s$) (Petit et al. 2025 [15]). From 2004 to 2016, the RAPID dataset exhibited a standard deviation of $\pm 0.9 Sv$ (Roach et al. 2022 [16]). This value is usually taken as the reference to study the AMOC variability which refers to its fluctuations over time. Different timescales and their main associated dynamic processes are briefly discussed, based on several papers, Zhang et al. 2019 [17], Jackson et al. 2022 [4], Roach et al. 2022 [16].

At annual timescales (high frequency), the North Atlantic Ocean is passively forced by the atmosphere (Zhang et al. 2019 [17]). The AMOC exhibits substantial variability on intra-annual and seasonal timescales (on the order of 100% of its mean value), and it is primarily driven by momentum variations (Ekman transport). Surface wind stress generates variations in Ekman transport that induce an instantaneous response in AMOC intensity (Roach et al. 2022 [16]). Specifically, spatial variations in these wind-driven transports cause downwelling and upwelling that displace the thermocline, generating local density anomalies and subsequent geostrophic current adjustments. Concurrently, heat and freshwater fluxes at the air-sea interface create buoyancy anomalies that directly modulate NADW formation (Jackson et al. 2022

[4]).

At decadal timescales (low frequency), the North Atlantic Ocean no longer behaves as a purely passive system. The AMOC exhibits reduced variability on inter-annual to decadal timescales (on the order of 10-30% of its mean value), which is mainly driven by water density anomalies resulting from persistent atmospheric forcing that modifies SST and SSS (Zhang et al. 2019 [17]). On these timescales, the AMOC variability exerts a pronounced influence on the climate system, such as the European climate, and can directly modulate the stability of the overturning circulation itself, as detailed in the following sections (Jackson et al. 2022 [4], Zhang et al. 2019 [17]).

2.1.3 AMOC stability

In present-day flow conditions, the AMOC exhibits a self-sustaining feedback mechanism. By transporting high-salinity water from the subtropical to the subpolar North Atlantic, the northward flow sustains the overturning circulation, which in turn reinforces this flow. This salt-advection feedback has maintained AMOC intensity throughout the Holocene. Two feedbacks must be taken into account to understand AMOC stability. If the AMOC weakens, less heat is transported, so the northern region cools down, making the water denser and promoting sinking. Therefore, the temperature feedback acts as a negative feedback on AMOC intensity, tending to stabilize it. However, if salinity decreases due to an influx of freshwater, the water at high latitudes becomes less dense, slowing down the AMOC. Consequently, less salt is transported to the region, weakening the circulation even further. Thus, the salinity feedback is positive and tends to destabilize the AMOC (Rahmstorf 2024 [2]; Weijer et al. 2019 [18]).

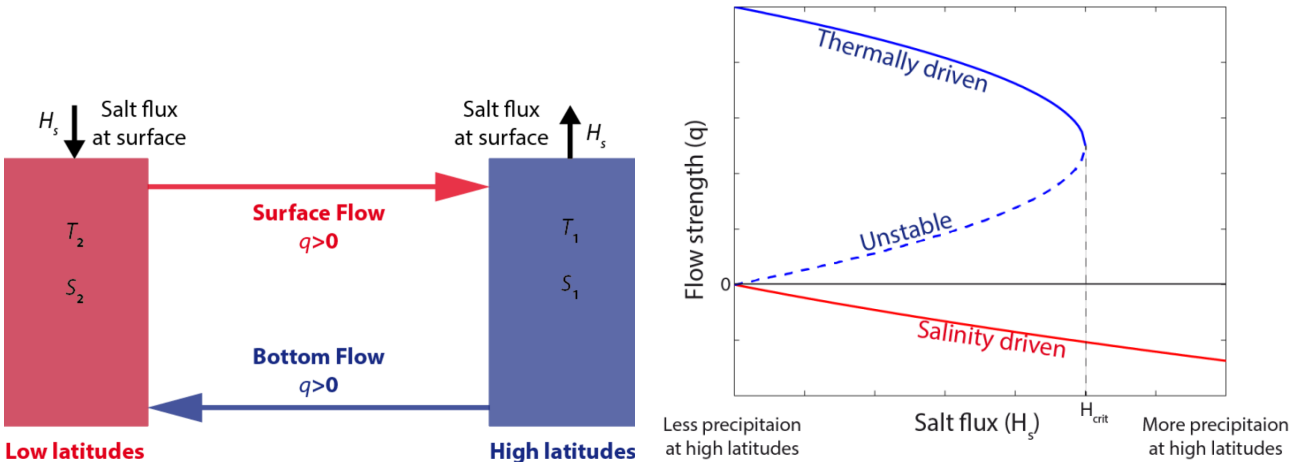
Beyond a critical threshold, a disturbance in salinity may become self-amplifying. This threshold is known as the Stommel bifurcation and corresponds to a disturbance strong enough to cause the AMOC to collapse. Stommel's box model can be used to illustrate the AMOC tipping point resulting from freshwater forcing, as explained later. While the scientific community agrees on this bifurcation behavior, the exact proximity of the AMOC to its tipping point remains unknown. Nevertheless, its impact on the climate system would be dramatic and would persist for centuries.

Analysis of the last deglaciation period has shown that the AMOC collapsed in response to meltwater forcing. During the transition from the Last Glacial Maximum (∼21–19 ka), a massive influx of freshwater perturbed deep ocean convection, leading to a near-complete shutdown of the AMOC during Heinrich Event 1 (∼17 ka). To map these long-term variations, researchers rely on both climate model simulations and geological proxy records, such as marine sediment, to reconstruct sea surface conditions. These proxy records reveal a highly dynamic history, showing that the circulation eventually underwent a rapid, massive recovery during the Bølling-Allerød warming (∼14.5 ka) once the meltwater forcing abruptly ceased (Otto-Bliesner and Brady. 2010 [5], Liu et al. 2015 [6], Rahmstorf 2024 [2]). Although this timescale is beyond the scope of this study, it demonstrates that the AMOC can collapse and recover under sufficiently strong forcing.

Stommel two-box model

To date, the AMOC has remained stable for more than 10 000 years. The response to a perturbation and the future equilibrium state can be explained using the Stommel two-box model

illustrated in Figure 2.3a. This model represents the Atlantic Ocean as two interconnected boxes, the red and blue boxes correspond to low and high latitudes, respectively. They exchange water via a surface flow from low to high latitudes and a return flow at depth in the opposite direction. Both boxes also exchange salt at the surface with the atmosphere.



(a) (b)

Figure 2.3: (a) Stommel two-box model of the meridional overturning circulation. The temperatures are assumed fixed and controlled by the atmosphere, such that $T_2 > T_1$. (b) Qualitative illustration of the flow strength (q) as a function of the salt flux, using the Stommel model. The solid blue line represents the thermally driven stable equilibrium, while the dashed blue line is an unstable equilibrium. The solid red line corresponds to the salinity driven stable equilibrium [19].

The density of seawater is approximated by a linear function of temperature and salinity:

$$\rho = \rho_0 - \alpha_T(T - T_0) + \beta_S(S - S_0) \tag{2.2}$$

With,
α_T the thermal expansion coefficient $[\frac{kg}{m^3 K}]$.
β_S the haline contraction coefficient $[\frac{kg}{m^3}]$.

Assuming that the flow intensity ($q[s^{-1}]$) is proportional to the density difference between the two boxes:

$$q = k_q(\rho_1 - \rho_2) = k_q\left(\alpha_T(T_2 - T_1) - \beta_S(S_2 - S_1)\right) = k_q(\alpha_T \Delta T - \beta_S \Delta S) \tag{2.3}$$

With,
k_q the hydraulic constant $[\frac{m^3}{kg \cdot s}]$.

According to Equation 2.3, the flow intensity q can take two opposite directions. If $\alpha_T \Delta T > \beta_S \Delta S$ ($q > 0$), surface water flows from high to low latitudes, corresponding to a thermally driven flow. Conversely, if $\alpha_T \Delta T < \beta_S \Delta S$ ($q < 0$), the water flows in the opposite direction at the surface, corresponding to a salinity-driven flow.

Additionally, the boxes exchange salt at the surface. An outgoing salt flux can be interpreted

as a freshwater influx that causes dilution, whereas an incoming salt flux represents the effect of evaporation. The salt balance is then expressed as:

$$\begin{cases} \dfrac{dS_1}{dt} = -H_S + |q|(S_2 - S_1) \\ \dfrac{dS_2}{dt} = H_S - |q|(S_2 - S_1) \end{cases} \Rightarrow \frac{d\Delta S}{dt} = 2H_S - 2|q|\Delta S \tag{2.4}$$

The steady-state solutions of Equation 2.4 depend on the sign of the flow strength:

$$\begin{cases} \Delta S_{1,2} = \dfrac{\alpha_T \Delta T}{\beta_S} \left(\dfrac{1}{2} \pm \sqrt{\dfrac{1}{4} - \dfrac{\beta_S H_S}{k_q (\alpha_T \Delta T)^2}} \right) & , \quad q > 0 \\ \Delta S_{3,4} = \dfrac{\alpha_T \Delta T}{\beta_S} \left(\dfrac{1}{2} \pm \sqrt{\dfrac{1}{4} + \dfrac{\beta_S H_S}{k_q (\alpha_T \Delta T)^2}} \right) & , \quad q < 0 \end{cases} \tag{2.5}$$

The stability analysis of Equation 2.4 demonstrates that ΔS_2 and ΔS_3 are stable equilibria, while ΔS_1 is an unstable equilibrium from which a small perturbation drives the circulation toward one of the two stable branches. The solution ΔS_4 can be discarded because the condition of $q < 0$ is not satisfied. The solutions ΔS_1 and ΔS_2 meet at a tipping point that represents the threshold of salinity forcing beyond which the flow q can no longer remain positive ($H_{crit} = (\alpha_T \Delta T)^2 k_q / 4\beta_S$, with $q > 0$ below H_{crit}). If a perturbation shifts the system to another equilibrium, the recovery trajectory back to the initial state differs from the path followed during the perturbation, a phenomenon known as hysteresis. These dynamics are illustrated in Figure 2.3b.

Other elements are crucial to understand AMOC stability, such as the different time response between the temperature and salinity feedbacks. Temperature perturbations have faster response times than salinity perturbations, leading to highly nonlinear behavior and making the system's history non-negligible (Weijer et al. 2019 [18]).

What causes the AMOC weakening ?

The scientific community is still debating the link between the AMOC response and human activity. Although the majority of studies suggest that AMOC weakening is an indirect consequence of the increase in greenhouse gas concentrations produced since the industrial revolution, this has not yet been rigorously demonstrated. The increase in atmospheric CO_2 concentration triggers extensive global warming, causing increased precipitation over the North Atlantic, higher SSTs, and the melting of sea ice. These anomalies decrease the surface water density gradient between low and high latitudes, thereby inducing an AMOC weakening (Madan et al. 2024 [20]). This physical mechanism is reproduced across numerous climate models subjected to an abrupt quadrupling of atmospheric CO_2, despite notable differences in the anomaly amplitudes, as shown in Figure 2.4, under the CMIP6 framework (Bellomo et al. 2021 [21]).

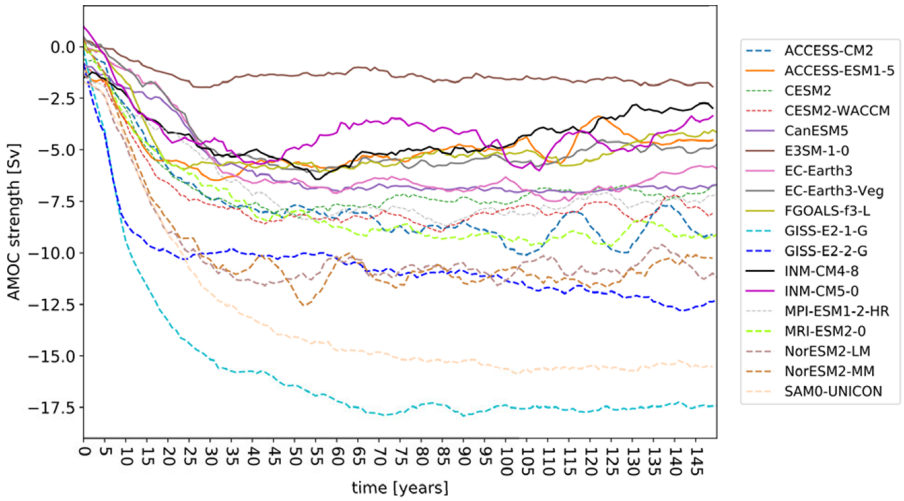


Figure 2.4: Anomalies of the strength of the AMOC in response to an abrupt quadrupling of the atmospheric CO_2 [21].

If the freshwater forcing is strong enough to reach the tipping point, the AMOC could eventually collapse. Such a collapse partially depends on both past and future emissions, making accurate predictions of this event extremely challenging. Several studies suggest that the AMOC could collapse before the 22nd century (Ditlevsen and Ditlevsen 2023 [22], Sgubin et al. 2017 [23], Dijkstra and van Weste 2025 [24], Smolders et al. 2024 [25]).

2.2 North Atlantic Oscillation

The North Atlantic Oscillation (NAO) (as shown in Figure 2.5) is the leading mode of sea-level pressure variability over the North Atlantic, with the pattern being most pronounced in winter. Spatially, it is primarily characterized by a north–south atmospheric dipole between the subtropical and subpolar latitudes of the North Atlantic basin. Consequently, it governs the direction and strength of geostrophic winds in this region according to Equation 2.7.

Quantifying the temporal evolution of the NAO is typically achieved through two main approaches, via meteorological station measurements or numerically via empirical orthogonal function (EOF) analysis of sea-level pressure (psl) fields. The station-based index is computed following Equation 2.6 and represents the normalized pressure difference between a mid-latitude location (such as the Azores or Lisbon) and a high-latitude location (such as Reykjavik).

$$\text{NAO} = psl'_{\text{Azores}} - psl'_{\text{Reykjavik}} \quad \text{with} \quad psl'_i = \frac{psl_i - \mu_{psl,i}}{\sigma_{psl,i}} \tag{2.6}$$

The NAO structures North Atlantic atmosphere circulation and has far-reaching climate impacts. A positive NAO phase corresponds to an enhanced pressure gradient that intensifies westerly winds, transporting warm, moist air into Northern Europe. This raises winter temperatures by 1–2 °C and increases precipitation from Iceland to Scandinavia. Conversely, this phase triggers severe drought across Southern Europe and drives cold northerly winds over Greenland and Northeastern Canada, decreasing local sea surface temperatures. Due to the combined effects of cooling and wind stress, the sea ice margin expands further in these regions. Simultaneously, the warm westerlies inhibit sea ice expansion in the Nordic Seas.

A negative NAO phase is characterized by a weaker pressure gradient, causing mid-latitude storm tracks to shift southward. This increases snow transport to Northern Europe. Simultaneously, Southern Europe undergoes warmer and wetter conditions. Sea ice exhibits the opposite response to that of a positive NAO phase, with enhanced expansion around Iceland driven by the combined effects of cooling and wind stress (Hurrell et al. 2003 [26]).

$$\boldsymbol{u}_h^g = \boldsymbol{k} \times \frac{1}{\rho \cdot f} \boldsymbol{\nabla}_h p \quad \text{with} \quad f = 2\Omega sin(\phi) \tag{2.7}$$

Here, $\boldsymbol{u}_h^g$ is the horizontal geostrophic wind vector, $\boldsymbol{k}$ is the vertical unit vector, ρ is the air density, f is the Coriolis parameter, Ω is the Earth rotation rate ($7.29 \times 10^{-5} rad/s$), ϕ is the latitude, and $\boldsymbol{\nabla}_h p$ is the horizontal pressure gradient vector.

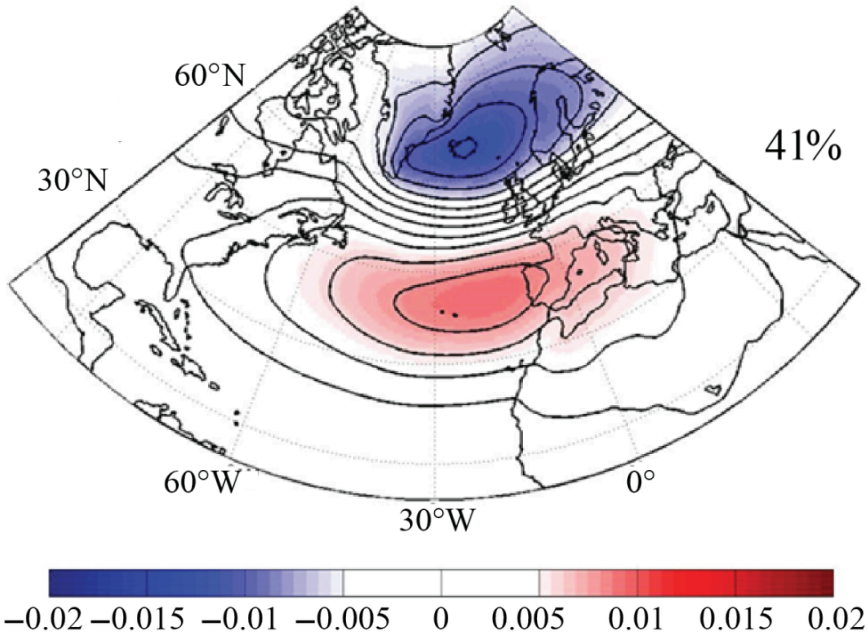


Figure 2.5: First leading EOF of winter (DJF) sea-level pressure (*psl*) from 1979 to 2013. The percentage indicates the amount of variance explained by the first mode [27].

2.3 Baroclinic instabilities

A fluid is said to be baroclinic (such as atmospheric air) if its density depends on both pressure and temperature (or salinity in the case of seawater). The intersection between isobaric and isothermal surfaces results in a vertical geostrophic wind shear, known as the thermal wind, expressed as (in pressure coordinates):

$$\frac{\partial \mathbf{u}_h^g}{\partial(-\ln p)} = \frac{R}{f} \mathbf{k} \times \nabla_{h,p} T, \tag{2.8}$$

where R is the gas constant for dry air and $\nabla_{h,p} T$ is the horizontal temperature gradient evaluated on an isobaric surface.

The existence of a zonal flow in thermal wind balance with the meridional temperature gradient (MTG) is a robust feature of the atmosphere, characterized by a tilted interface that separates

cold, dense subpolar air from warm, lighter subtropical air, maintaining a reservoir of available potential energy (APE). However, this configuration is inherently unstable. Under specific conditions, small atmospheric perturbations can trigger baroclinic instability, converting the APE into kinetic energy of synoptic eddies that transport energy and momentum poleward. The conversion from potential to kinetic energy cannot occur under arbitrary conditions, it must take place in a specific direction bounded by the isentropic surface (a surface of constant potential temperature) and the horizontal, as illustrated in Figure 2.6 (Kalashnik et al. 2022 [28], Molemaker et al. 2022 [29]).

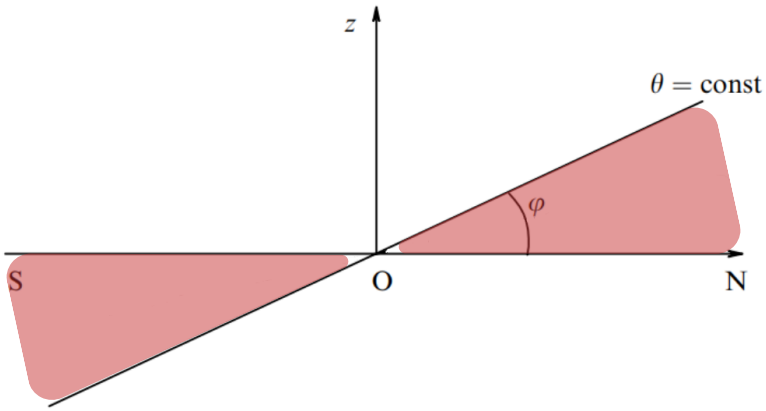


Figure 2.6: Schematic of an instability wedge (shaded in red) in the Northern Hemisphere. φ is the angle between the isentropic surfaces (θ) and the horizontal. N and S represent the northward and southward direction respectively. Adapted from [28].

Baroclinic instability fuels storm tracks, which have a typical length scale of 1000km wide and a characteristic lifetime on the order of 7 days. Consequently, baroclinic instability has profound impacts on Earth's climate system, as these storm tracks act as the primary atmospheric mechanism for the poleward heat and moisture transport.

2.4 Impact of the AMOC weakening

So far, the physical mechanisms governing the AMOC, the NAO, and baroclinic instabilities have been described, while only a few of their impacts have been mentioned. The following section focuses on impacts of AMOC weakening across the North Atlantic and Europe, based on studies using different climate models that employ the same experimental design as that presented in Chapter 3.

A weakened AMOC reduces northward oceanic heat transport, causing widespread ocean surface and atmospheric cooling across the North Atlantic (Jackson et al. 2015 [8], Liu et al. 2020 [30]). This regional reduction in oceanic heat transport significantly delays and mitigates Arctic sea ice loss across all seasons (Liu et al. 2020 [30]). Europe experiences widespread seasonal cooling of several degrees, which peaks sharply in Northern and Eastern regions during winter due to downstream amplified Arctic cooling (Jackson et al. 2015 [8], Van Westen et al. 2025 [31]). Paradoxically, a weakened AMOC results in fewer winter cold spells in Europe. The enhanced meridional temperature gradient provides available baroclinic energy to strengthen the mid-latitude westerly jet stream, which prevents the formation of persistent North Atlantic atmospheric blocking systems that typically drive prolonged European cold spells (Jackson et

al. 2015 [8]).

Large-scale surface cooling reduces the atmospheric capacity to hold moisture via the Clausius-Clapeyron relation (see Equation 2.9). This generates widespread precipitation declines across the Northern Hemisphere mid-latitudes and the majority of continental Europe (Bellomo et al. 2023 [32], Van Westen et al. 2025 [31]). Despite lower total precipitation, colder conditions lead to an increase in overall snowfall rates, snow depth, and the proportion of precipitation falling as snow across Europe. This initiates an extended winter snow-cover season that begins earlier and finishes later in the year (Van Westen et al. 2025 [31]). The combined effects of reduced rainfall and modified snowmelt timing result in substantial, uniform reductions in surface water runoff and river flows (-30% to -80%) across major European river basins. These hydrological changes induce water stress, amplifying hydrological drought risks (Van Westen et al. 2025 [31]).

$$\frac{de_s}{dT} = \frac{L_v}{T\Delta\alpha} \tag{2.9}$$

Where e_s is the saturation vapor pressure with respect to liquid water, T is the air temperature, $L_v = 2257kJ/kg$ the latent heat of vaporization of water at typical atmospheric temperatures, and $\Delta\alpha$ is the specific volume difference between the gas and liquid phase.

A deceleration of the AMOC induces strong surface cooling south of Greenland, which significantly sharpens the near-surface meridional temperature gradient across the North Atlantic mid-latitudes. This enhanced gradient drives an intensification and poleward shift of the Northern Hemisphere mid-latitude westerly jet stream during winter (Liu et al. 2020 [30], Bellomo et al. 2023 [32]). The enhanced baroclinic instability generated by stronger thermal gradients fuels the North Atlantic storm track, while persistent high-pressure systems over Scandinavia, Greenland, and the Nordic Seas become less frequent as the stronger westerly jet stream inhibits the formation and maintenance of atmospheric blocking systems (Jackson et al. 2015 [8]). These atmospheric pressure anomalies project strongly onto the positive phase of the North Atlantic Oscillation during winter, increasing the frequency and overall duration of persistent NAO+ circulation regimes (Jackson et al. 2015 [8], Bellomo et al. 2023 [32]). In contrast, the summer response features a negative summer NAO phase that reduces the intensity of summer westerly winds across central Europe (Van Westen et al. 2025 [31]).

Beyond physical climate changes, the North Atlantic acts as a major sink for atmospheric carbon, responsible for absorbing $\sim 40\%$ of the net oceanic uptake of CO_2. Historical records and modeling data confirm that a slowdown of the overturning circulation significantly diminishes the net oceanic CO_2 uptake (Frajka-Williams et al. 2019 [18], Schaumann and Asenjo 2025 [9]). Given the rise in atmospheric CO_2 driven by anthropogenic activities, an AMOC weakening acts as a positive feedback on atmospheric CO_2 concentrations.

These results outline the impacts of an AMOC weakening, yet substantial uncertainties persist in future projections, with the most significant being the future radiative forcing from greenhouse gases emissions, which depends primarily on political and socioeconomic decisions and is thus extremely difficult to predict.

Chapter 3

Materials and methods

This section describes and justifies the choice of the climate model, the corresponding experimental design and its context, as well as the statistical approach employed to analyze the variables that produce the results presented in Chapter 4. The dataset is accessible via `https://zenodo.org/records/14884357`.

3.1 Experimental Design: NAHosMIP

The data were generated through a set of experiments conducted within the North Atlantic Hosing Model Intercomparison Project (NAHosMIP), a standardized experimental framework. These experiments artificially introduce freshwater into the North Atlantic (referred to as uniform hosing) for a fixed period to investigate the rate and mechanisms of AMOC weakening and whether the AMOC recovers once the uniform hosing stops (Jackson et al. 2023 [33]). Figure 3.1 shows how the freshwater is uniformly added at high latitudes. The circular yellow region (R_1) encompasses the domain from 50°N in the North Atlantic to the Bering Strait at 66°N (including the Arctic). For a given hosing of H (in this case $H = 0.3m^3/s$), the hosing field h is defined as,

$$\begin{aligned} h(i,j) &= \frac{H}{\int_{R_1} dxdy} \quad \text{for} \quad i,j \in R_1 \\ &= 0 \quad \text{otherwise} \end{aligned} \tag{3.1}$$

where dx and dy are the zonal and meridional grid spacings, and i and j are the zonal and meridional grid coordinates.

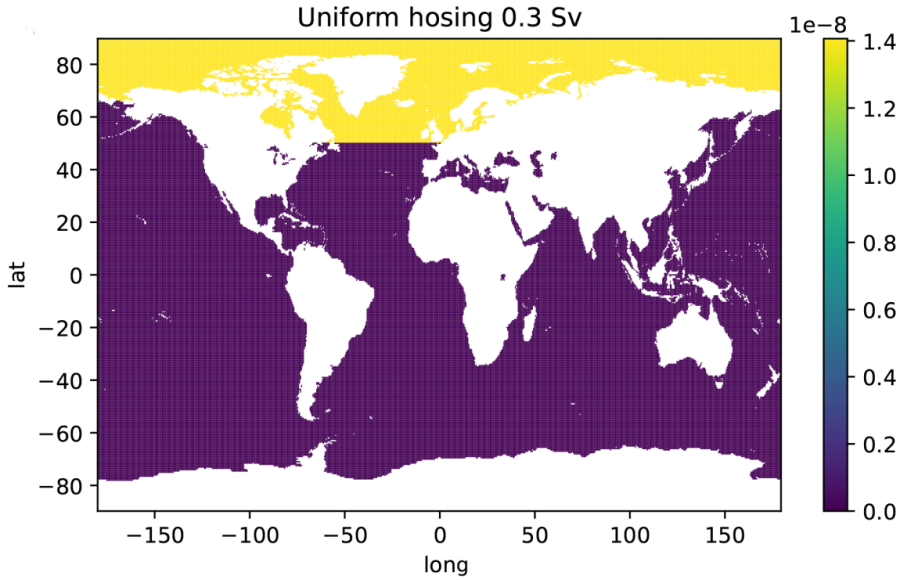


Figure 3.1: The uniform hosing field. The units of the colorbar are m/s and it represents the velocity of the added freshwater in the region R_1 [33].

According to the current state of the art, the scientific community suggests that the decline in AMOC intensity is a response to increasing atmospheric CO_2 concentrations. However, this thesis specifically seeks to understand the direct impacts of an AMOC weakening which motivates the use of this framework. Because no additional CO_2 is artificially added to the atmosphere, this approach isolates AMOC impacts from greenhouse gas warming, providing a suitable setup to answer the research questions.

3.2 Model Description: CanESM5

The results presented in the subsequent Chapter 4 were generated using the Canadian Earth System Model version 5 (CanESM5). The specifications of this model are listed in Table 3.1. A primary objective of CanESM5 is to simulate future climate projections on centennial timescales. The model features relatively coarse resolution and high computational throughput, which facilitates the production of large ensembles. CanESM5 has a notably higher equilibrium climate sensitivity (ECS) of 5.6 K compared to the 3.7 K observed in its previous version. CanESM5 simulations contribute to the Coupled Model Intercomparison Project Phase 6 (CMIP6) (Eyring et al. 2016 [34]).

Within the dataset, eight climate models are available, four of them demonstrate a quasi-stable low AMOC state and are listed in Table 3.1. A quasi-stable state is assumed when the AMOC intensity remains low for centuries after the hosing has ceased. These experiments provide the North Atlantic and European climate conditions associated with a sustained low-AMOC state, which is essential for the purpose of this study.

Model	Model Atm, Ocean, Ice	Resolution Atm, Ocean	Levels Atm, Ocean	Ref.
CanESM5	CanAM5, NEMO3.4.1, LIM2	2.8°, 1°	49, 45	[35]
IPSL-CM6A-LR	LMDZ6, NEMO3.6, LIM3	2°, 1°	79, 75	[36]
CESM2	CAM6, POP2, CICE5	1°, 1°	32, 60	[37]
HadGEM3-GC3-1MM	UM GA7, NEMO3.6, CICE GSI8.1	0.7°, 0.25°	85, 75	[38]

Table 3.1: The first column lists the models exhibiting a quasi-stable AMOC state. Their associated Atmosphere, Ocean, and Ice model are displayed in the second column. The resolution and levels of each model are presented in the third and fourth columns.

To select CanESM5 from the pool of candidates, the duration and drift (linear slope) of the low-AMOC state across experiments are evaluated in Table 3.2. CanESM5 offers an optimal trade-off between experimental simulation length and stability. It exhibits the second-longest low-AMOC period alongside a more stable trend with a weaker absolute slope (-0.95 Sv/100 years, compared to 1.13 Sv/100 years for CESM2). Additionally, CanESM5 provides an additional recovery experiment compared to CESM2 and HadGEM3-GC3-1MM, thereby offering a broader range of simulation configurations to study AMOC recovery pathways. From a practical standpoint, the dataset structure of CanESM5 is particularly convenient, as each experiment is stored in a single file per variable, unlike other models where the outputs are split across multiple files per experiment, which substantially facilitates data processing and analysis.

Model	control AMOC experiment [Sv]	Number of experiment	Low AMOC experiment	Range [year]	Slope [Sv/100year]
CanESM5	11.35 ± 0.85	4	r70	180	-0.95
IPSL-CM6A-LR	12.48 ± 1.24	4	r100	150	1.03
CESM2	17.94 ± 0.84	3	r50	190	1.13
HadGEM3-GC3-1MM	16.33 ± 0.84	3	r50	100	0.39

Table 3.2: The first column lists the models exhibiting a quasi-stable AMOC state. Second column shows the mean and the standard deviation of the control experiment over their full range. The third column indicates the number of experiments (including control, hosing, and recovery experiments). Subsequent columns provide quasi-stable AMOC experiment, its time range, and its slope of the linear fit.

Studied experiments of the CanESM5 model:

- piControl: preindustrial control.
- u03-hos: constant uniform hosing of 0.3 Sv in the North Atlantic.
- u03-r50: experiment with no hosing initialised 50 years into u03-hos.
- u03-r70: experiment with no hosing initialised 70 years into u03-hos.

3.3 Statistical Approach and Variables

Europe is divided into four distinct regions following the United Nations geoscheme, excluding Russia, Iceland and Svalbard as shown in Figure 3.2. Table 3.3 summarizes the variables used

in this study.

To isolate the low-frequency response from high-frequency internal climate variability, the time series are generally low-pass filtered using a decadal running mean. However, in a few cases, multi-decadal running means are applied to increase sample sizes for statistical robustness. When high-frequency filtering is not required, the annual mean is retained.

For seasonal mean anomaly maps, statistical significance at the 90% confidence level is determined using Welch's t-test for surface air temperature and sea-level pressure assuming a normal distribution and unequal variances. However, the non-parametric Mann-Whitney U test is applied to precipitation data to account for its non-normal distribution, which is frequently modeled as a Weibull distribution.

For seasonal standard deviation maps, the variable is first linearly detrended at each grid point, which is assumed valid if the background trend is approximately linear over the timescale of interest. Then, for each season, the corresponding months are averaged to produce a reference season map, from which the standard deviation is computed. The statistical significance of the standard deviation anomalies is assessed using an F-test at the 90% confidence level. Conversely, time series analyses require a more sophisticated detrending method based on centered running mean subtraction to eliminate nonlinear climate drift. For seasonal or regional time series, the seasonal months or the regional grid points are averaged before being detrended.

Variable	Unit	Temporal resolution
maximum AMOC streamfunction at 26.5°N	Sv	yearly
Surface Air Temperature (tas)	$°C$	monthly
Precipitation flux (pr)	mm/day	monthly
Air pressure at sea level (psl)	hPa	monthly

Table 3.3: Variables used in this study with their converted units and their temporal resolution.

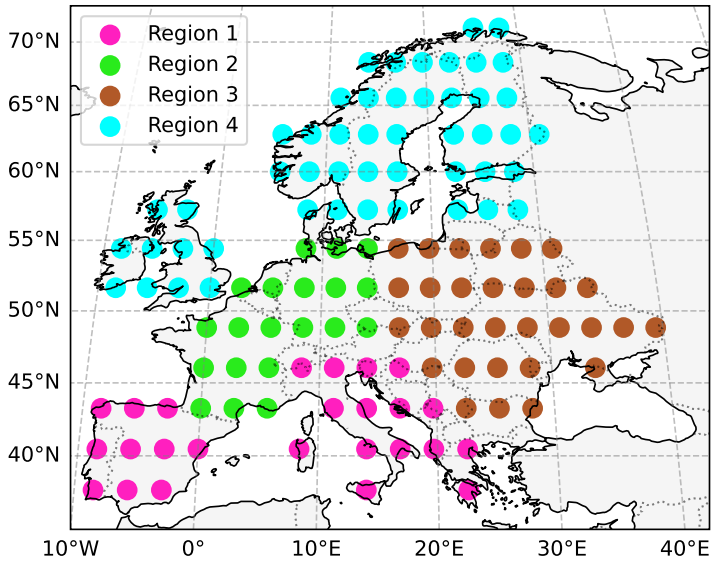


Figure 3.2: European regions: Southern Europe (pink), Western Europe (green), Eastern Europe (brown), Northern Europe (cyan).

	Southern Europe	Western Europe	Eastern Europe	Northern Europe	Total
Grid points	25	20	30	49	124
Weight, w_i [%]	20.16	16.13	24.19	39.52	100

Table 3.4: Grid point distribution and their associated weights among the four Europe regions.

3.4 Model validation

Validation of the CanESM5 model is based on observational and reanalysis data. In this study, the AMOC time series, the NAO spatial pattern, the NAO index time series and its power spectral density are evaluated against observations and reanalysis datasets.

The RAPID project has pioneered the use of arrays of moorings to measure the variability of the meridional overturning circulation (MOC) at 26.5°N, sustaining continuous observations for more than 20 years. These data (available at `https://rapid.ac.uk/`) are compared with two decades of measurements against the CanESM5 model control experiment in Figure 3.3. As shown in Table 3.5, which presents the annual means of both the RAPID observations and the control experiment, there is a substantial difference in their mean values. Specifically, the CanESM5 model underestimates the mean strength of the AMOC by 5.67 Sv on average. This systematic negative bias may contribute to a cooler European climate than observed due to reduced OHT.

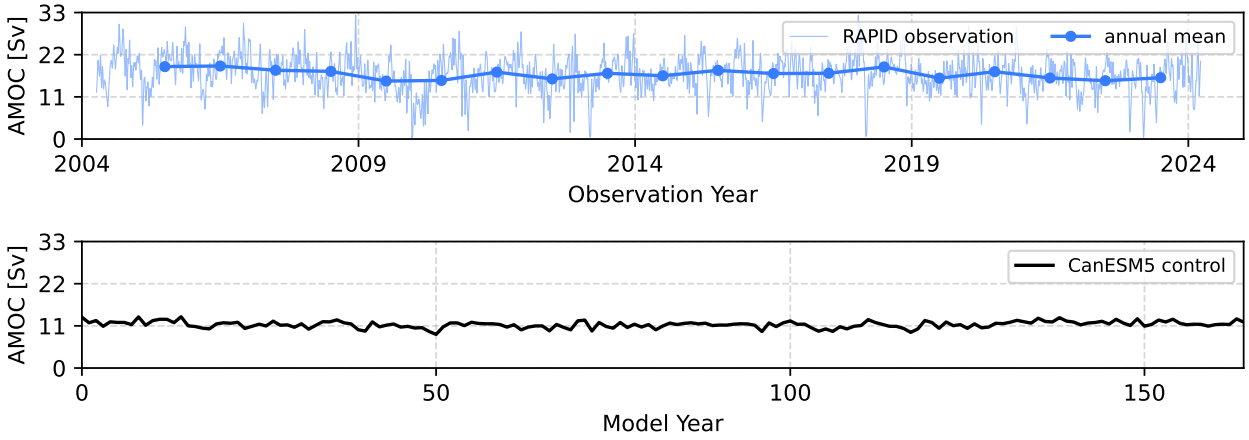


Figure 3.3: The upper graph displays the RAPID data corresponding to the observed 12-hourly MOC transport (thin blue line) and the annual mean (thick blue line) at 26.5°N from April 2004 to March 2024. The lower graph represents the CanESM5 maximum AMOC streamfunction at 26.5°N of the control experiment from year 0 to 164.

	Mean [Sv]	Standard deviation [Sv]
MOC observations (RAPID)	17.02	1.23
Control experiment (CanESM5)	11.35	0.85

Table 3.5: The results come from Figure 3.3. MOC observations: Mean of the raw observations, and standard deviation of the annual mean. Control experiment: mean and standard deviation of the simulation.

Because the first research question aims to understand the role of the NAO in this changing dynamic of a low-AMOC state, its simulation must be appropriate. For this purpose, the ERA5 dataset (available at `https://cds.climate.copernicus.eu/datasets`) enables a comparison of the NAO spatial pattern, time series, and the power spectral density with the control experiment of the CanESM5 model, as shown in Figures 3.4 3.5, and 3.6, respectively. ERA5 is the global climate reanalysis dataset produced by the European Centre for Medium-Range Weather Forecasts (ECMWF). It combines historical observational data with numerical models to provide spatially and temporally continuous land and ocean parameters from 1940 to the present, making it more suitable for comparison with the CanESM5 model than sparse observational station records alone.

The CanESM5 correctly reproduces the characteristic dipole structure of the NAO. However, the total variance explained by the first mode is slightly lower than in ERA5, indicating that the NAO mode is slightly less dominant in the model over the North Atlantic domain (36.74% in ERA5 and 34.42% in CanESM5). Additionally, the model exhibits a northeastward shift in both centers of action and a larger pressure gradient per standard deviation. These biases modify the simulated atmospheric circulation, leading to northeastward-shifted and stronger westerlies across the North Atlantic compared to observations. Regarding the time series and power spectral density, CanESM5 accurately captures the overall temporal variability. The standard deviations of the monthly time series are very similar between the control run and the reanalysis (1.71 in ERA5 and 1.66 in CanESM5), but nevertheless reflect only a minor underestimation of temporal variability in the simulations. Furthermore, Halifa-Marín et al. [39] similarly demonstrated that the CanESM5 model accurately reproduces the observed NAO by capturing large-scale circulation variability and synoptic patterns.

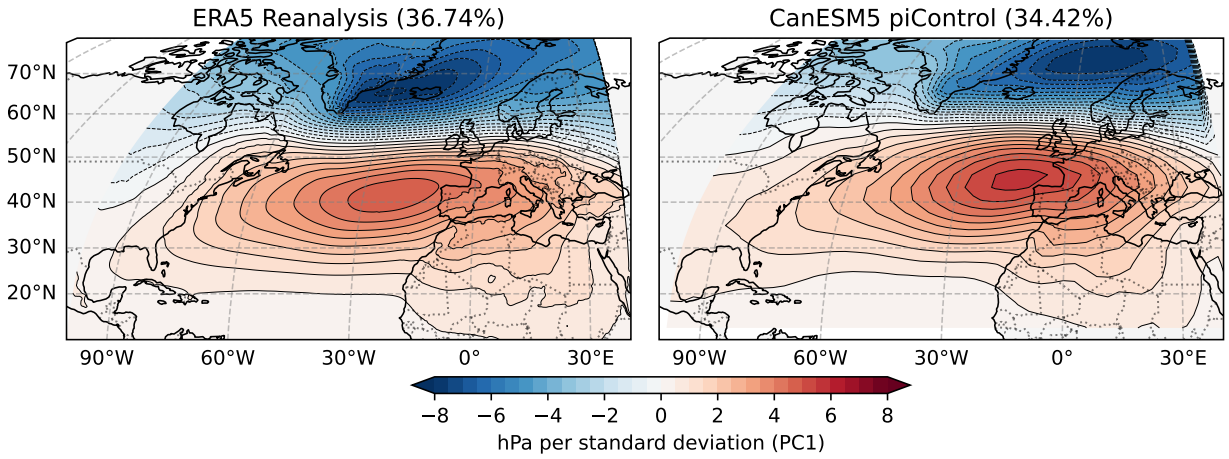


Figure 3.4: The first Empirical Orthogonal Function (EOF1) of winter (DJF) *psl* for ERA5 Reanalysis (left) from 1940 to 2026, and the CanESM5 control experiment (right) from year 0 to 164 in the Atlantic region (10°N–80°N, 100°W–40°E). The percentage represents total winter *psl* variance explained by the first mode.

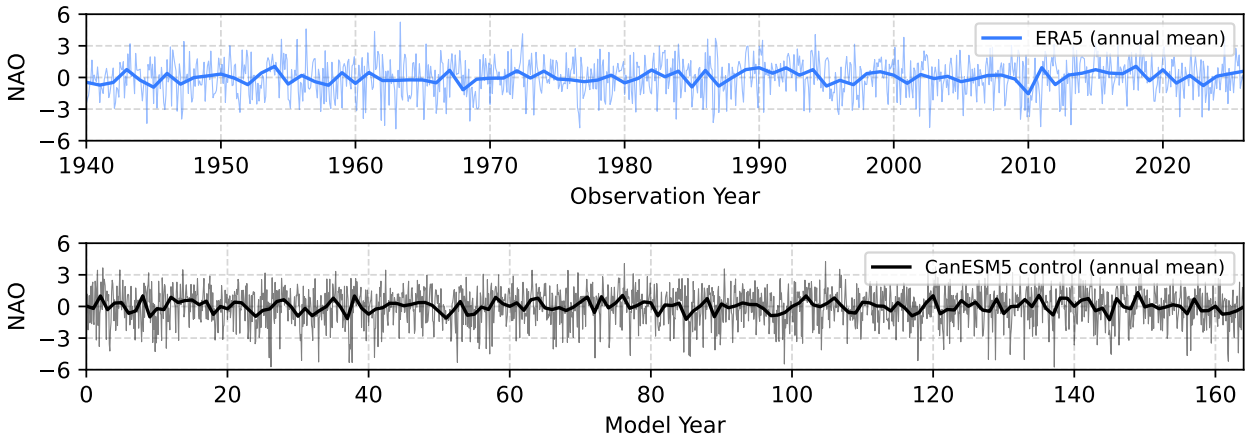


Figure 3.5: The upper graph displays the ERA5 data corresponding to the monthly observed NAO index (thin blue line) and its annual mean (thick black line) from 1940 to present. The lower graph represents the monthly NAO index (thin blue line) and its annual mean (thick black line) of the control experiment from year 0 to 164.

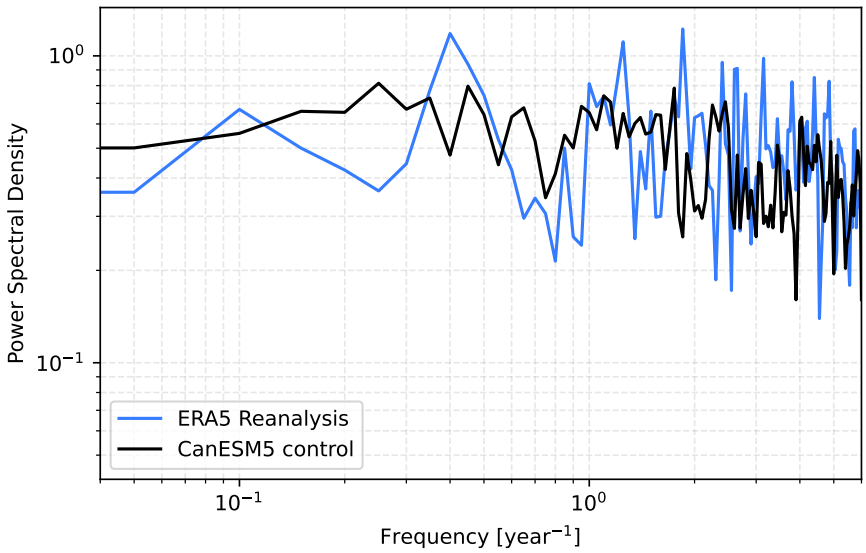


Figure 3.6: Power spectral density of the NAO timeseries from 25 year cycle (lower bound) to 2 months cycle (upper bound). The blue and black lines correspond to ERA5 reanalysis and CanESM5 control experiment respectively.

Chapter 4

Results

4.1 Experiments and Global View

This first section presents the evolution of the maximum AMOC streamfunction at 26.5°N across different scenarios (see Figure 4.1) and the associated European annual mean temperatures (see Figure 4.2). These comparisons provide a comprehensive view of the European climate response, while highlighting several notable behaviors.

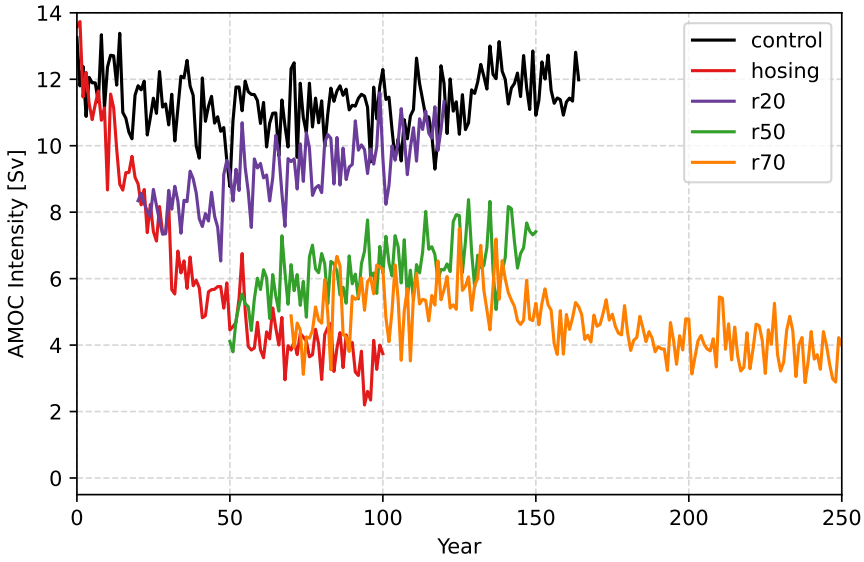


Figure 4.1: AMOC streamfunction at 26.5°N for different experiments.

The CanESM5 model includes five distinct experiments shown in Figure 4.1, the control run (black), the hosing phase (red) and three recovery phases after 20, 50 and 70 years of hosing (purple, green and orange respectively).

The control run remains relatively stable around its mean value of 11.35Sv. In contrast, the hosing experiment exhibits an immediate decline in response to the freshwater forcing, losing more than 60% of its intensity after 100 years, compared to the control baseline. The recovery experiments demonstrate different degrees of AMOC stability and hysteresis behavior depending on the duration of the forcing. When the hosing ceases after 20 years, the AMOC recovers rapidly. The r50 experiment appears to follow a recovery trajectory at a slower rate, although

a longer simulation period would be required to confirm this behavior. Crucially, 70 years of hosing is sufficient to maintain a low-AMOC state on centennial timescales.

Although the r20 AMOC streamfunction data are available in the database, this experiment is omitted from the subsequent analysis because no other variable fields (*tas*, *pr*, *psl*) are provided in the CanESM5 model or any other models exhibiting a quasi-stable AMOC state.

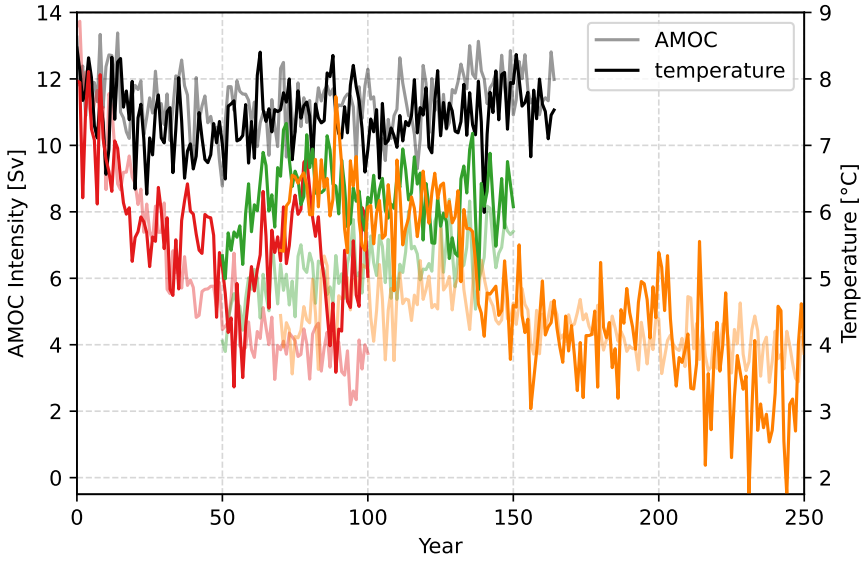


Figure 4.2: European annual mean temperature (opaque lines) associated with their AMOC streamfunction (semi-transparent lines) for different experiments: control (black), hosing (red), r50 (green) and r70 (orange).

Given that the primary objective is to understand the impact of an AMOC weakening on the European climate, the most critical variable in this analysis is the surface air temperature (*tas*). The Figure 4.2 illustrates the coupling between the AMOC and European temperature. A first general observation links reduced AMOC intensity to colder temperatures. Specifically, all perturbed scenarios exhibit a colder annual mean temperature compared to the control run (with the exception of a few extreme years). However, certain periods remain either completely or partially unexplained by the AMOC alone. This is the case for the last 50 years of the hosing experiment, where a large oscillation increases the temperature by approximately 2°C, while the AMOC remains weak. Similarly, the r50 experiment shows a warming phase followed by a plateau, even though the AMOC increases linearly. To support these observations, Figure 4.3 shows the linear fit of the mean European temperature as a function of the normalized AMOC signal (based on a decadal running mean), following the relation,

$$T(t) = \alpha \cdot \mathrm{AMOC}'(t) + \varepsilon \quad \text{with} \quad \mathrm{AMOC}'(t) = \frac{\mathrm{AMOC}(t) - \mu_{\mathrm{AMOC}}}{\sigma_{\mathrm{AMOC}}} \tag{4.1}$$

Although this simple linear expression fits the hosing and r70 experiments surprisingly well (according to the coefficient of determination r^2), it fails to capture higher-frequency contributions, while the temperature trajectory in r50 remains completely unexplained.

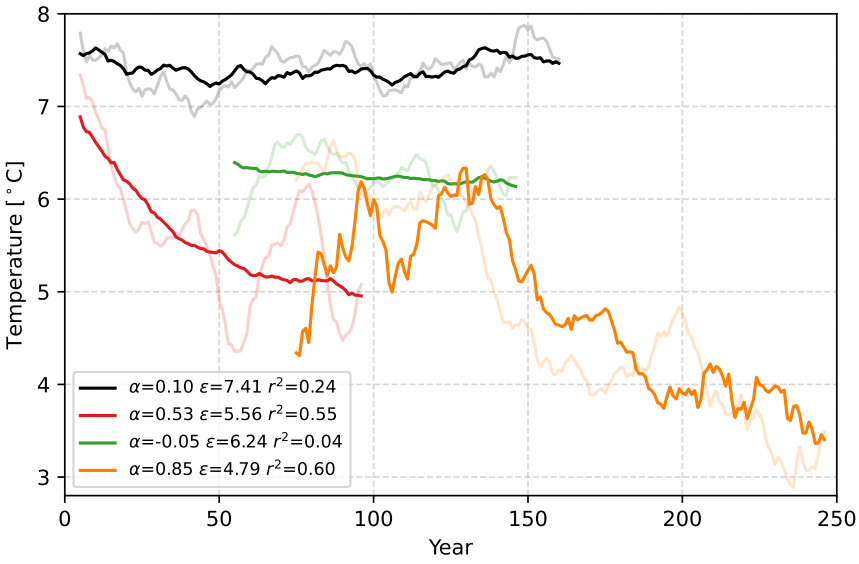


Figure 4.3: Linear fit (opaque lines) of European decadal running mean temperature (semi-transparent lines) for different experiments: control (black), hosing (red), r50 (green) and r70 (orange). The units of α and ε are °C.

This simple linear expression, reflected by its low coefficient of determination (r^2), highlights significant anomalies in the decadal running mean temperature that motivate the search for an additional climate driver. However, first it is necessary to evaluate the baseline impacts of a low-AMOC state on Europe.

4.1.1 European Climate under low-AMOC state

As mentioned previously, an AMOC weakening induces a cooling trend across Europe, as demonstrated in Figure 4.4. Within the hosing and r70 experiments, the temperature decreases progressively, with enhanced cooling across high-latitude regions. However, the temperature remains stable during r50, though its value is lower compared to the control experiment. The Western and Eastern European temperatures (green and brown trajectories in Figure 4.4) exhibit highly similar trajectories, suggesting that European temperature varies less in the zonal direction than in the meridional direction. Furthermore, Northern Europe's temperature profile and the overall European temperature profile (see Figure 4.2) show similar behavior, as demonstrated in Table 4.1, which computes the percentage of European temperature variance (C_i) originating from region i,

$$C_i = \frac{w_i \mathrm{Cov}(T_i, T_{\mathrm{EU}})}{\mathrm{Var}(T_{\mathrm{EU}})} \quad \text{with} \quad T_{\mathrm{EU}}(t) = \sum_{i=1}^{4} w_i T_i(t) \tag{4.2}$$

The European temperature (T_{EU}) is the weighted sum of each regional temperature (T_i), the weights (w_i) can be found in Table 3.4.

While Northern Europe is the largest region (39.52% of European grid points), its dominance in driving European temperature variability is not an artifact of spatial weighting. In the control run, its variance contribution (44.64%) is only slightly higher than its spatial weight. However, under a low-AMOC state, its influence rises up to 69.16% of the total variance in

the r70 scenario. Among all regions, Southern Europe represents the least dominant region in terms of explaining the total variance. It never reaches 11% in any scenario, while it accounts for 20.16% of the grid points. Table 4.1 also provides results computed with 10-year running mean temperature signals. They show an even more dominant Northern Europe contribution across all scenarios, reaching a contribution from 58.52% during hosing to 72.03% in the r70 experiment.

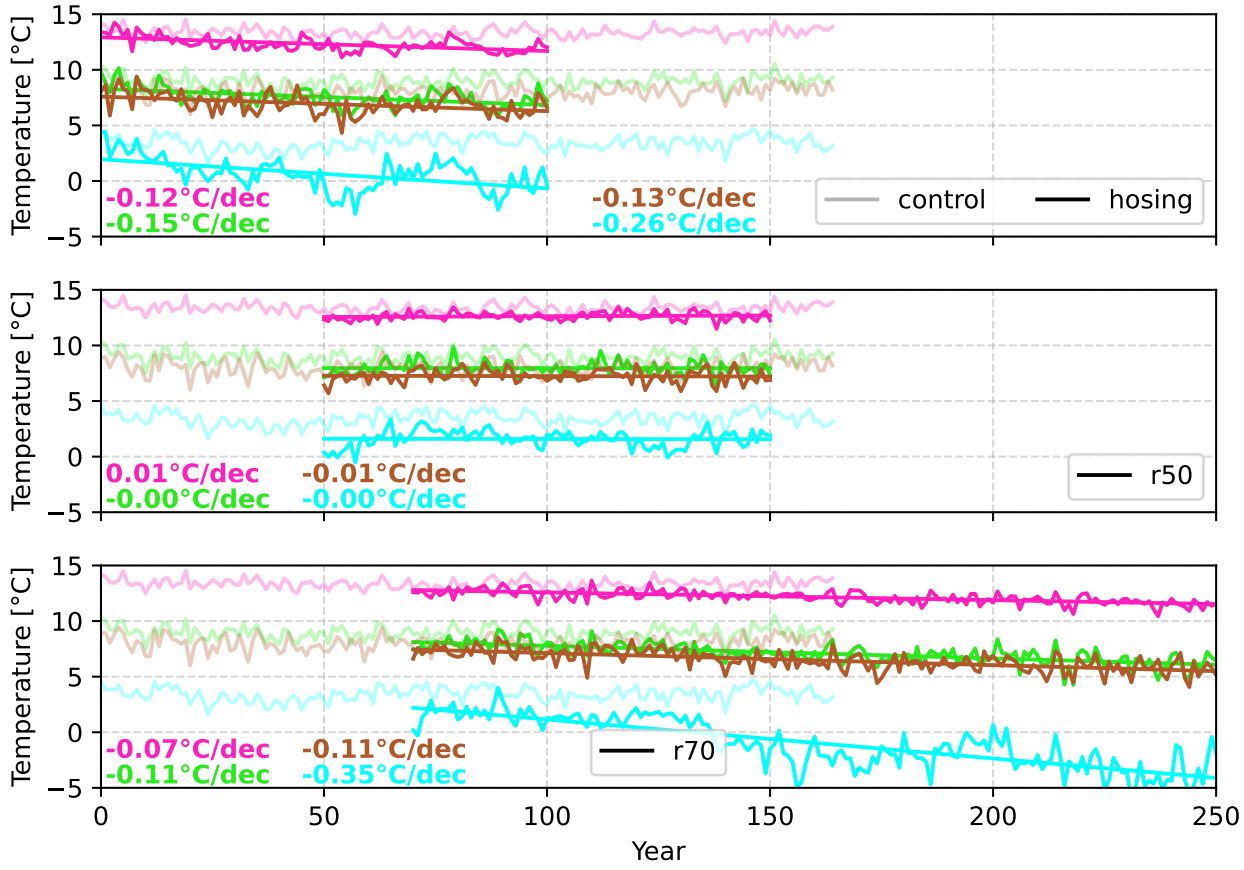


Figure 4.4: European annual mean temperature for each region (defined in Figure 3.2): Southern Europe (pink), Western Europe (green), Eastern Europe (brown), Northern Europe (blue). Top, middle and bottom plot corresponding to the hosing, r50 and r70 experiments respectively (opaque lines). Linear regression fits and their slopes (in °C/dec) have been computed for each region.

	Weighted covariance decomposition [%]			
Annual mean	Southern Europe	Western Europe	Eastern Europe	Northern Europe
control	10.91	16.02	28.43	44.64
hosing	10.78	12.80	19.50	56.92
r50	9.21	15.39	21.98	53.42
r70	6.50	9.70	14.64	69.16
10-year mean	Southern Europe	Western Europe	Eastern Europe	Northern Europe
control	4.98	12.14	20.03	62.85
hosing	10.97	11.80	18.70	58.52
r50	5.92	10.60	15.58	67.90
r70	6.33	8.90	12.73	72.03

Table 4.1: Percentage of European temperature fluctuations originating from each region across control, hosing, and recovery scenarios. The upper and lower tables are performed with annual mean and 10-year running mean temperature signals respectively.

The seasonal spatial anomalies (see Figure 4.6) provide additional insight into the spatial distribution of the cooling response across Europe. These anomalies are computed by subtracting the control from the r50 experiment over the period from year 50 to 150. A general cooling occurs in every season with enhanced amplitudes at higher latitudes, confirming the strong meridional dependence of European temperature. These findings align with previous literature, similar temperature trends have been identified by Jackson et al. 2015 [8] using HadGEM3, Bellomo et al. 2023 [32] using EC-Earth3, and Liu et al. 2020 [30] using the Community Climate System Model version 4 (CCSM4). Winter exhibits the most pronounced anomalies, which are localized over the Nordic Seas and the Labrador Sea. This dynamic can be attributed to sea ice expansion driven by the reduced oceanic heat transport (OHT) associated with a weaker AMOC. Sea ice expansion further amplifies the cooling effect and acts as a positive feedback. Although sea ice concentration or sea surface temperature (SST) would be more suitable to study the sea ice expansion, surface air temperature (*tas*) is assumed to be sufficiently correlated with sea ice extent to justify this physical explanation. A similar mechanism regarding the sea ice expansion and its amplification of European temperature anomalies has been detailed by van Westen and Baatsen 2025 [40] and Liu and Fedorov 2022 [41]. The anomalies in precipitation (*pr*) and sea-level pressure (*psl*), reveal a widespread reduction in precipitation (drier conditions) and an increased sea-level pressure. As temperature decreases, the saturation vapor pressure decreases according to the Clausius-Clapeyron relation, reducing the air capacity of holding water vapor and leading to less precipitation. Simultaneously, via the hydrostatic equilibrium, the colder air mass becomes denser resulting in an increase in sea level-pressure (Van Westen et al. 2025 [31], Jackson et al. 2015 [8]). For clarity, the corresponding seasonal anomaly maps for *pr* and *psl* are displayed in the Appendix B.1 and B.2.

Similar to the regional dominance analysis, Table 4.2 evaluates the percentage of European temperature variance (C_j) originating from season j,

$$C_j = \frac{\frac{1}{4}\mathrm{Cov}(T_j, T_{\mathrm{EU}})}{\mathrm{Var}(T_{\mathrm{EU}})} \quad \text{with} \quad T_{\mathrm{EU}}(t) = \sum_{j=1}^{4} \frac{1}{4} T_j(t) \tag{4.3}$$

While each season has an equal temporal weight ($\frac{1}{4}$), the seasonal analysis reveals that European temperature variability is heavily dominated by winter and spring. In the control experiment,

winter accounts for 38.32% of the interannual variance and spring represents the second largest contributor at 31.15%. Conversely, summer contributes the least to European temperature variance, representing only 12.18% in the control run. Under low-AMOC states, winter remains the most dominant season. The 10-year running mean acts as a low-pass filter smoothing the high-frequency variability of the winter season. Consequently, the gap between the winter and spring season narrows, and spring eventually becomes the dominant season, as shown for the r50 experiment.

These covariance analyses provide key insights concerning the interpretation of the European temperature profile, introduced in Figure 4.2. It shows that the European temperature is mostly driven by the Northern Europe region and the winter season, pointing to a strong coupling between sea ice dynamics and European temperature.

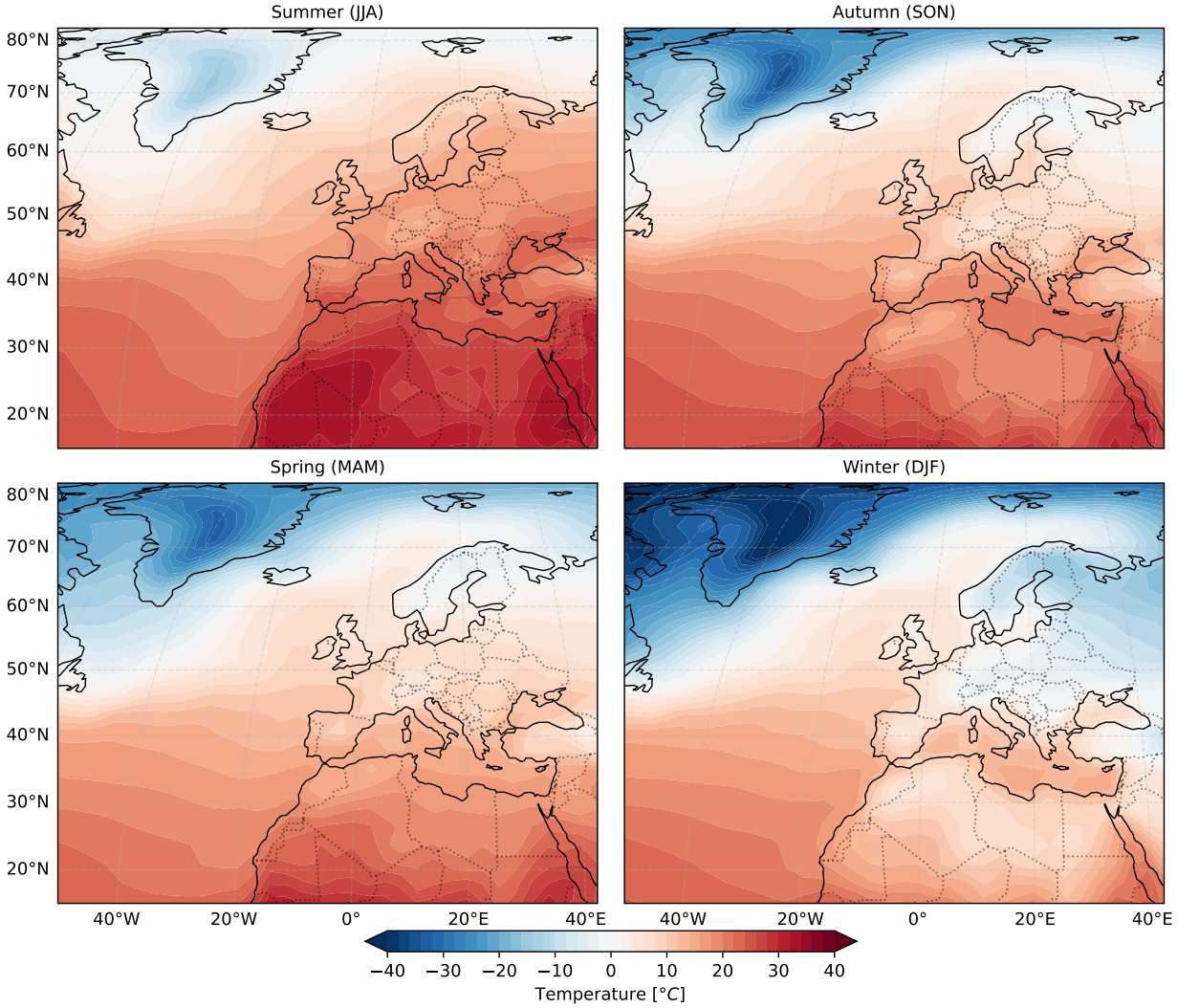


Figure 4.5: Seasonal absolute temperature mean of the control experiment from year 0 to 164.

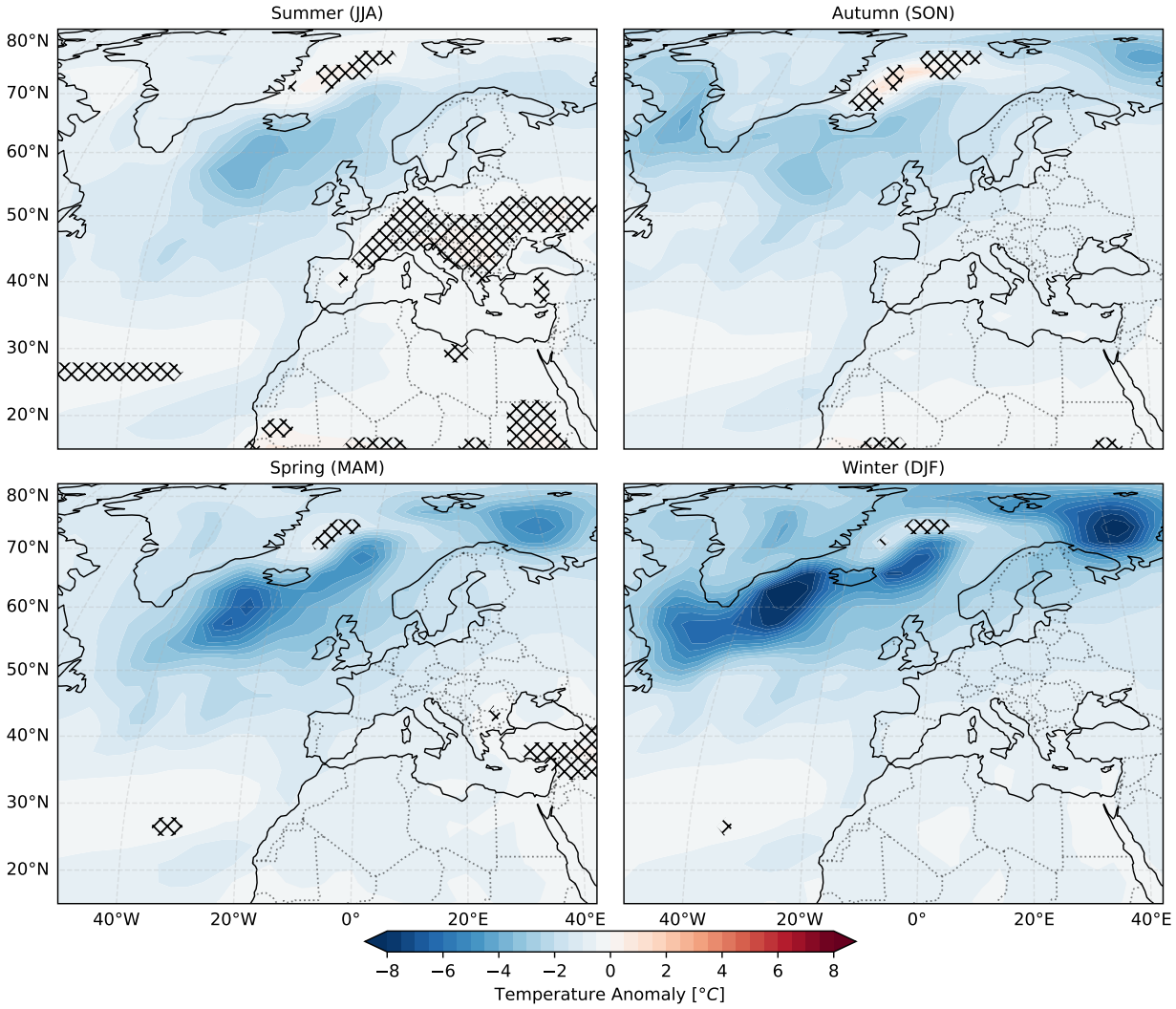


Figure 4.6: Seasonal temperature anomaly between r50 and the control experiment from year 50 to 150 (r50 minus control). Hatched area corresponds to nonsignificant area.

	Weighted covariance decomposition [%]			
Annual mean	Summer (JJA)	Autumn (SON)	Winter (DJF)	Spring (MAM)
control	12.18	18.35	38.32	31.15
hosing	15.23	18.32	33.98	32.47
r50	15.93	16.70	35.65	31.71
r70	10.20	17.22	41.40	31.18
10-year mean	Summer (JJA)	Autumn (SON)	Winter (DJF)	Spring (MAM)
control	15.18	23.44	36.82	24.56
hosing	15.08	19.16	33.19	32.57
r50	19.03	21.44	28.36	31.17
r70	10.47	17.15	41.11	31.28

Table 4.2: Percentage of European temperature fluctuations originating from each season across control, hosing, and recovery scenarios. The upper and lower tables are performed with annual mean and 10-year running mean temperature signals respectively.

4.2 NAO contribution

Thus far, the analysis demonstrates that the AMOC accounts for low-frequency temperature trend over Europe. Conversely, the NAO structures the atmospheric circulation of the North Atlantic and contributes to European climate at higher frequencies. Understanding the dynamical coupling between the AMOC, the NAO, and the European climate is the focus of the following section.

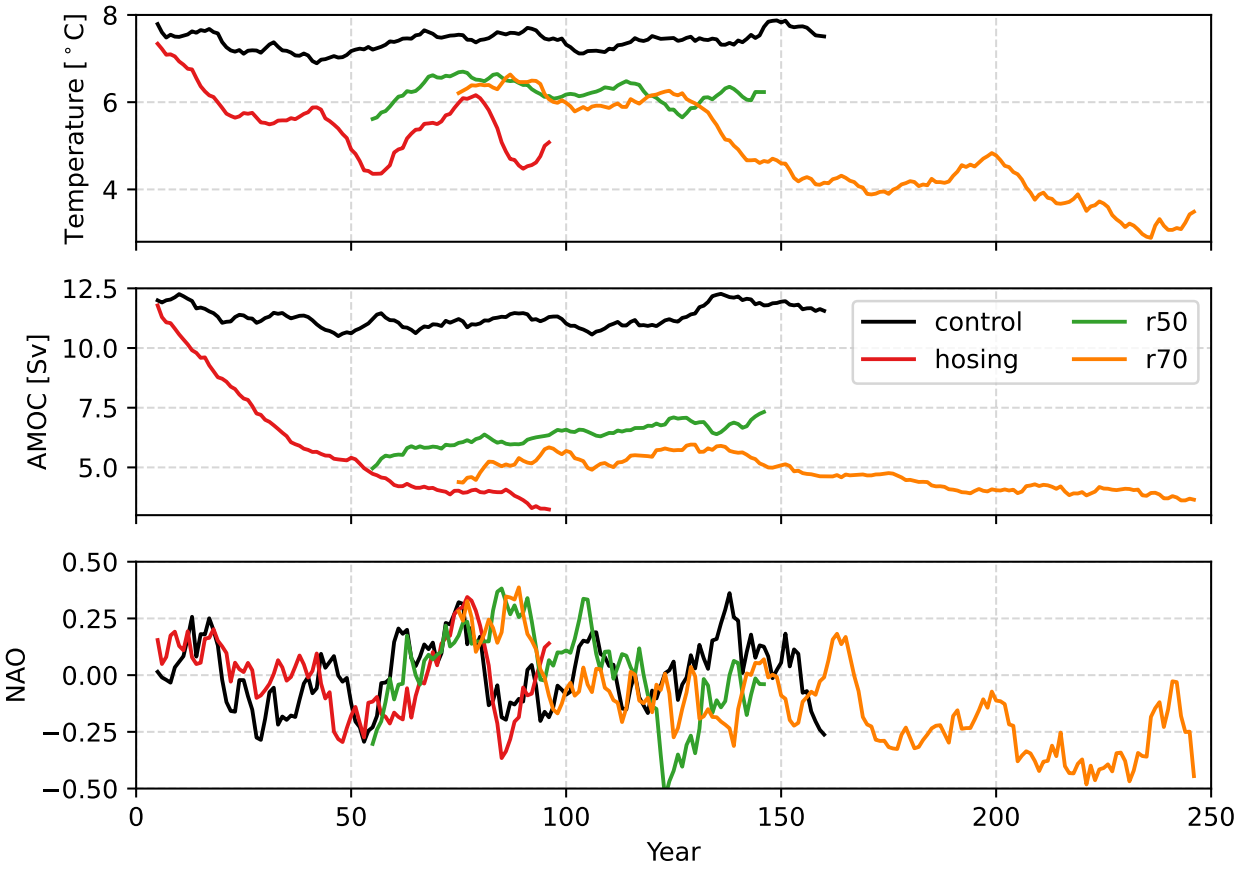


Figure 4.7: Decadal running mean of European temperature, AMOC and NAO signals for each experiment.

The individual decadal running means of European temperature, the AMOC, and the NAO shown in Figure 4.7 provide insight into how the impact of the NAO on European temperatures varies under different AMOC strengths. One specific period makes this comparison possible. From year 55 to 80, the control, hosing and r50 experiments all exhibit a pronounced increase in the NAO index, rising from approximately -0.25 to 0.25. However, the corresponding temperature trajectories during this period increase less when the AMOC is stronger. Table 4.3 provides the quantitative values for this period.

	year 55 → year 80		
	Temperature [°C]	NAO index	Mean AMOC [Sv]
control	7.20 → 7.43 (+0.23)	−0.23 → 0.17 (+0.40)	11.13
hosing	4.36 → 6.09 (+1.73)	−0.12 → 0.22 (+0.34)	4.35
r50	5.62 → 6.51 (+0.89)	−0.30 → 0.15 (+0.45)	5.60

Table 4.3: Quantitative values for years 55 and 80. The values on the left and right of the arrow correspond to the year 55 and 80 respectively. The values in parentheses are the difference of year 80 and year 55. The AMOC values are the mean during the time period between year 55 and 80.

This discrepancy suggests that an AMOC weakening amplifies the NAO impact on European temperature. Figures 4.8, 4.9 and 4.10 show the anomalies between the negative and positive NAO phases in the control, hosing and r50 experiments. In every scenario, the winter season exhibits the most intense anomalies in the Nordic Seas. The hosing experiment does not necessarily exhibit the greatest anomalies in terms of amplitude but the signal is wider and shifted southward compared to the control experiment. As the anomalies reach lower latitudes, they eventually reach Northern Europe and influence the European temperatures, as observed in the time series in Figure 4.7. When the AMOC intensity is higher, such as in the control run, the winter temperature anomalies are confined to higher latitudes, and almost no European grid points show statistically significant changes, suggesting that the slight temperature difference may not be linked to the NAO.

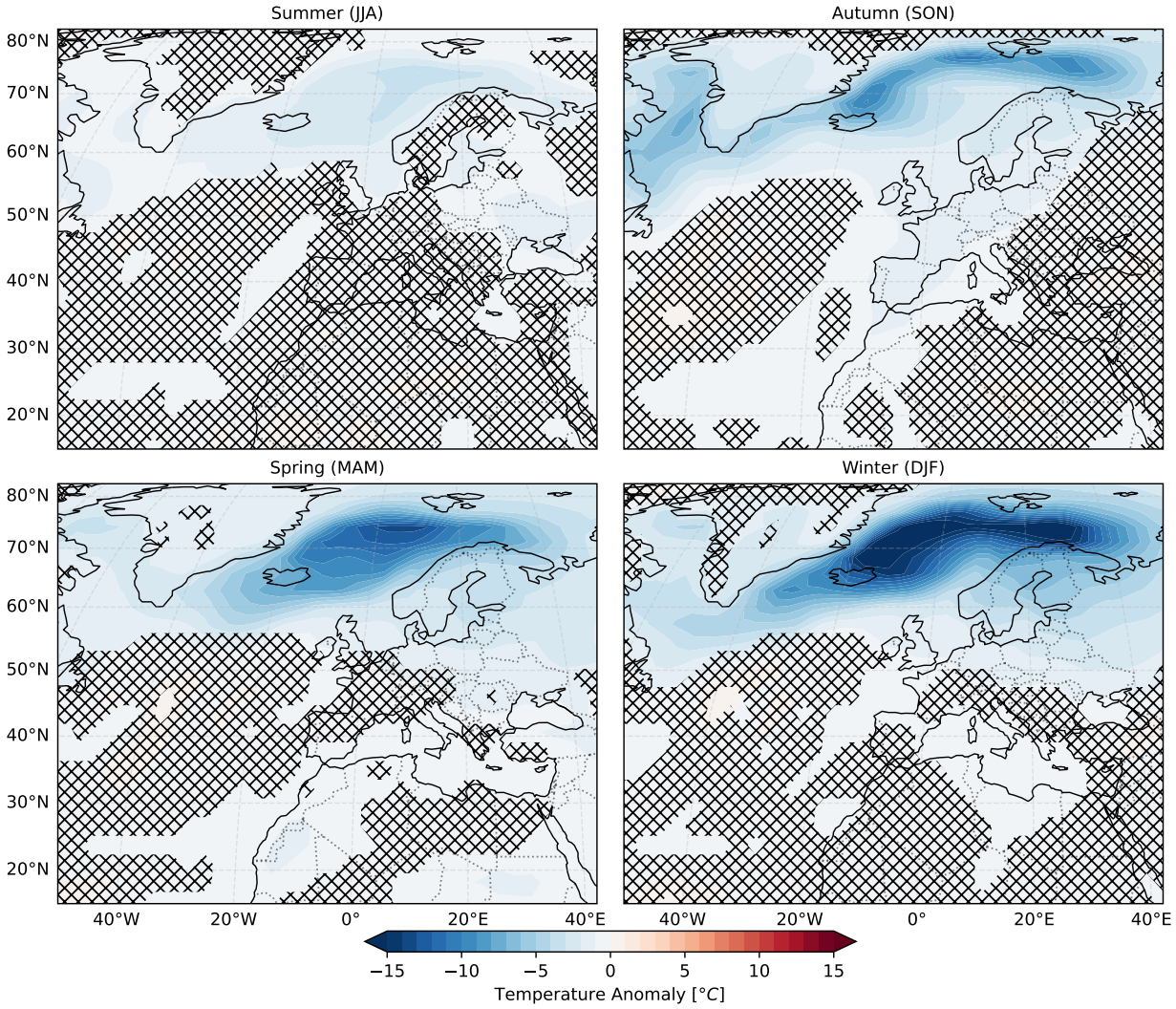


Figure 4.8: Seasonal temperature anomaly, of the hosing experiment, between two 10-year periods representing distinct NAO phases: years 50–60 (negative NAO) and years 73–83 (positive NAO). Anomalies are computed as negative NAO period minus positive NAO period. Hatched area corresponds to nonsignificant area.

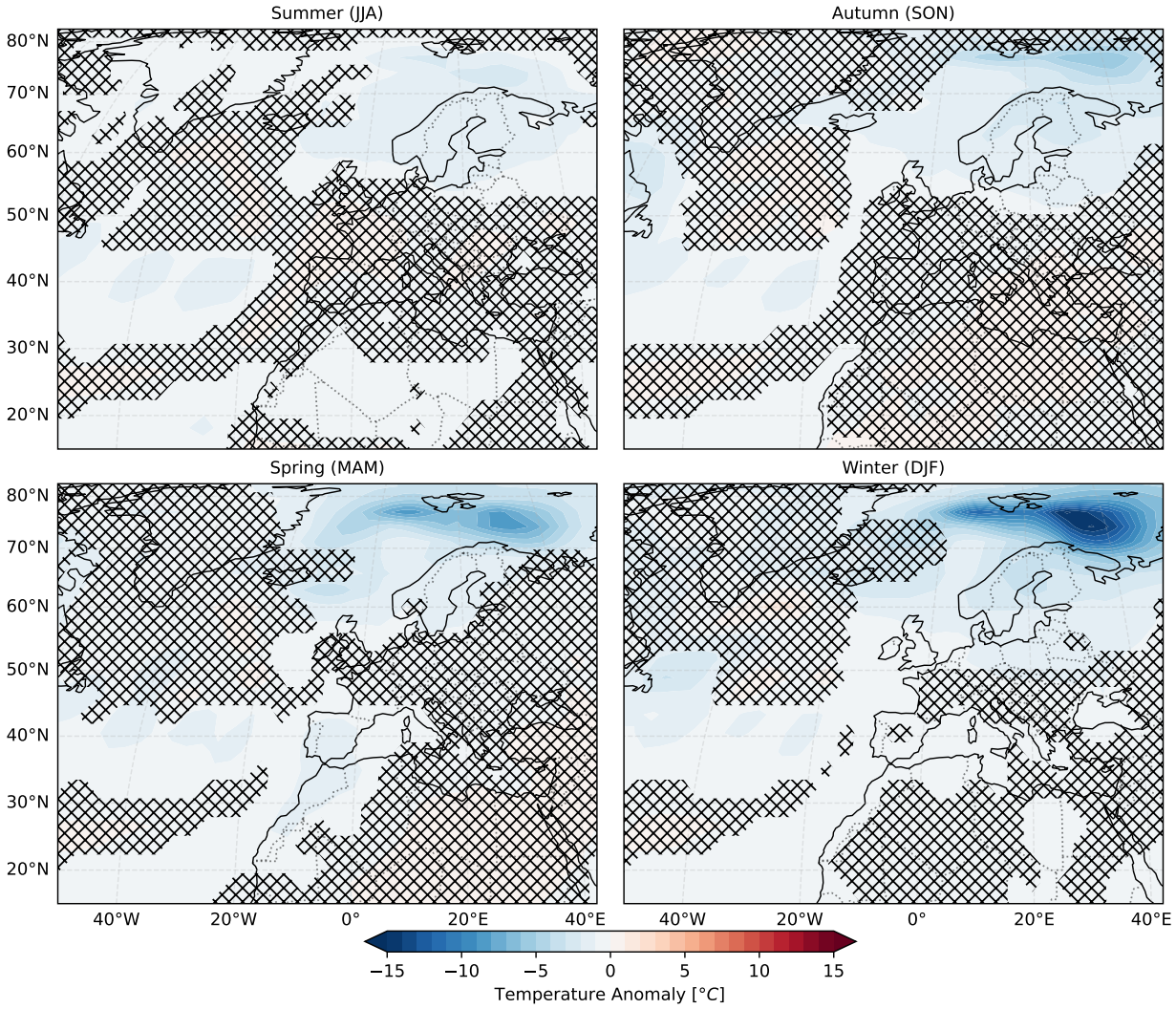


Figure 4.9: Seasonal temperature anomaly, of the r50 experiment, between two 10-year periods representing distinct NAO phases: years 50–60 (negative NAO) and years 73–83 (positive NAO). Anomalies are computed as negative NAO period minus positive NAO period. Hatched area corresponds to nonsignificant area.

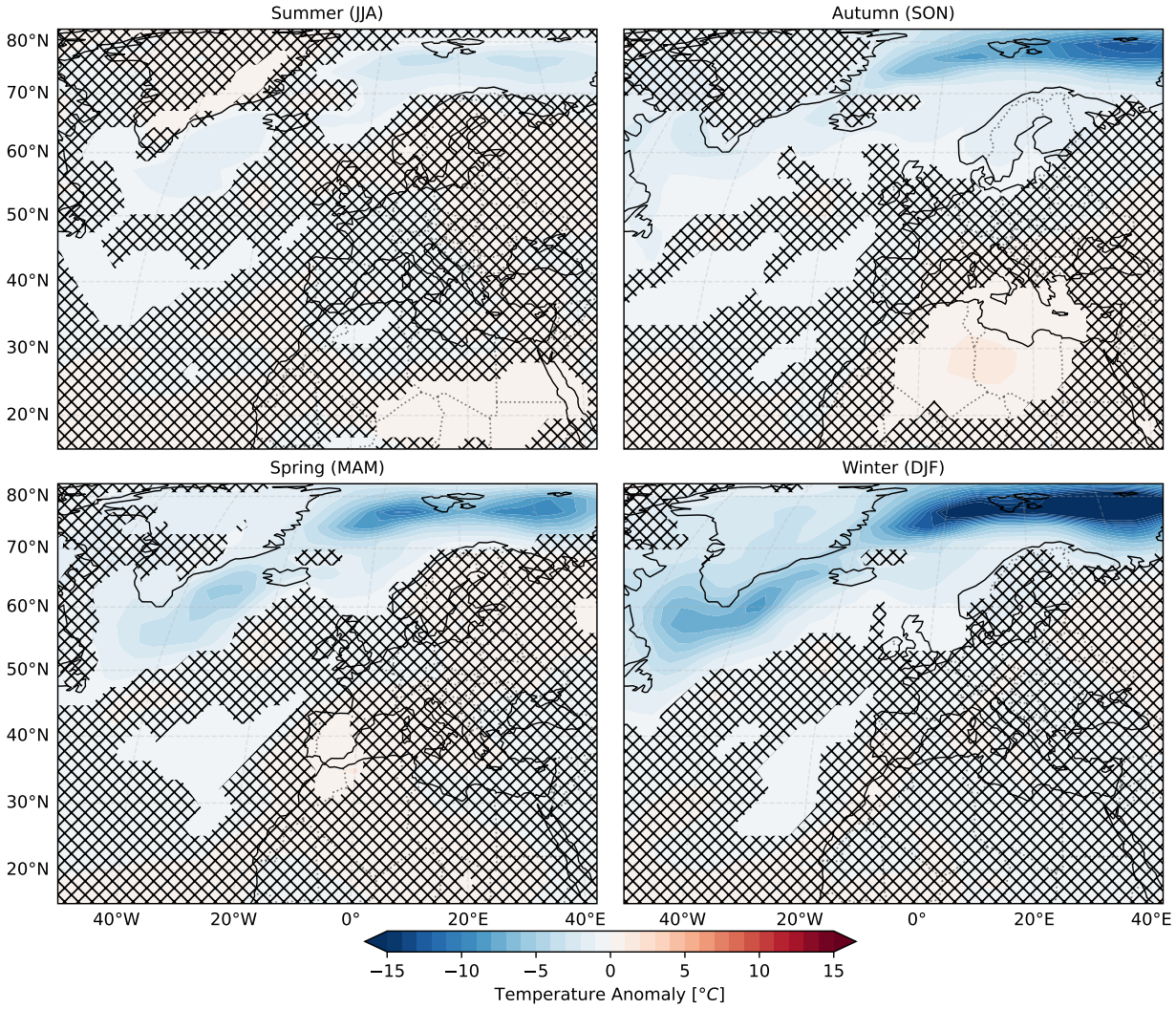


Figure 4.10: Seasonal temperature anomaly, of the control experiment, between two 10-year periods representing distinct NAO phases: years 50–60 (negative NAO) and years 73–83 (positive NAO). Anomalies are computed as negative NAO period minus positive NAO period. Hatched area corresponds to nonsignificant area.

To clarify the mechanism, positive and negative NAO phases are mapped in Figures 4.11 and 4.12 respectively. The wind vectors (black arrows) and the temperature gradients determine the horizontal temperature advection across the North Atlantic. The maximum temperature gradients are located close to the sea ice edge. The NAO influence is the weakest in summer compared to other seasons, as it is mainly a winter phenomenon. A negative NAO phase amplifies, mostly in winter, the sea ice expansion, thereby shifting the maximum temperature gradient southward. The Figure 4.13 illustrates the seasonal horizontal temperature gradient anomaly between the negative and positive NAO regimes during the hosing experiment. Summer shows almost no significant gradient anomalies demonstrating that the interaction between the NAO phase and temperature gradients is almost exclusively an autumn-to-spring phenomenon. During a negative NAO phase, weaker westerlies allow cold Arctic air to advect further south, shifting the sea ice boundary and the associated temperature gradient southward towards Northern Europe. This is highlighted by the presence of a dipole anomaly during autumn, winter and spring. This link between the NAO and sea ice is consistent with find-

ings from previous studies (Schurer et al 2023 [42], Pedersen et al 2016 [43]). Consequently, Northern Europe experiences enhanced cold-air advection in winter, even though the overall intensity of the geostrophic winds is weaker. These wind and temperature gradient patterns are systematic across all scenarios, supporting the aforementioned interpretations.

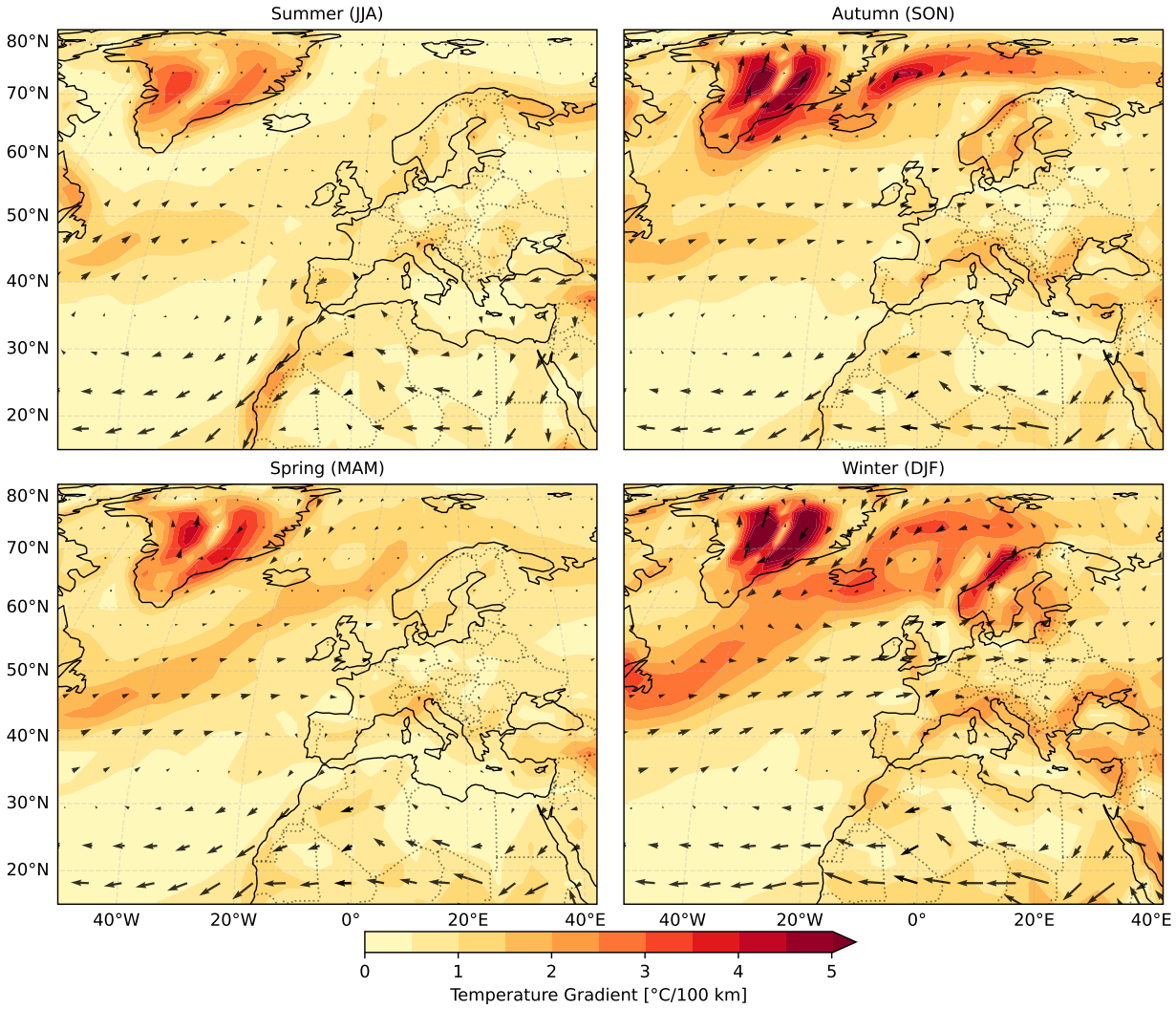


Figure 4.11: Mean geostrophic wind (black arrows) and mean temperature gradient from year 50 to 60. Low AMOC strength and negative NAO index situation.

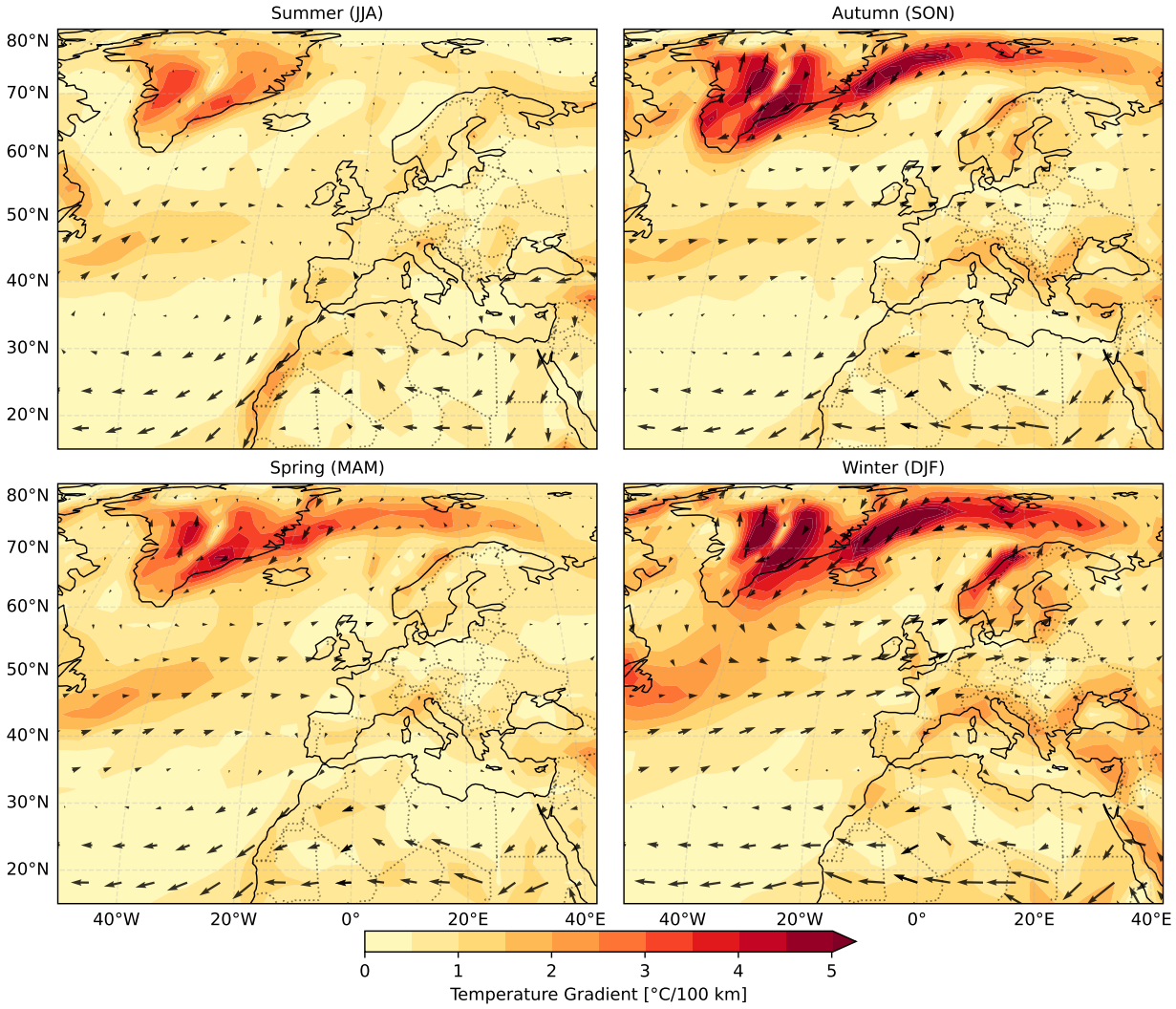


Figure 4.12: Mean geostrophic wind (black arrows) and mean temperature gradient from year 73 to 83. Low AMOC strength and positive NAO index situation.

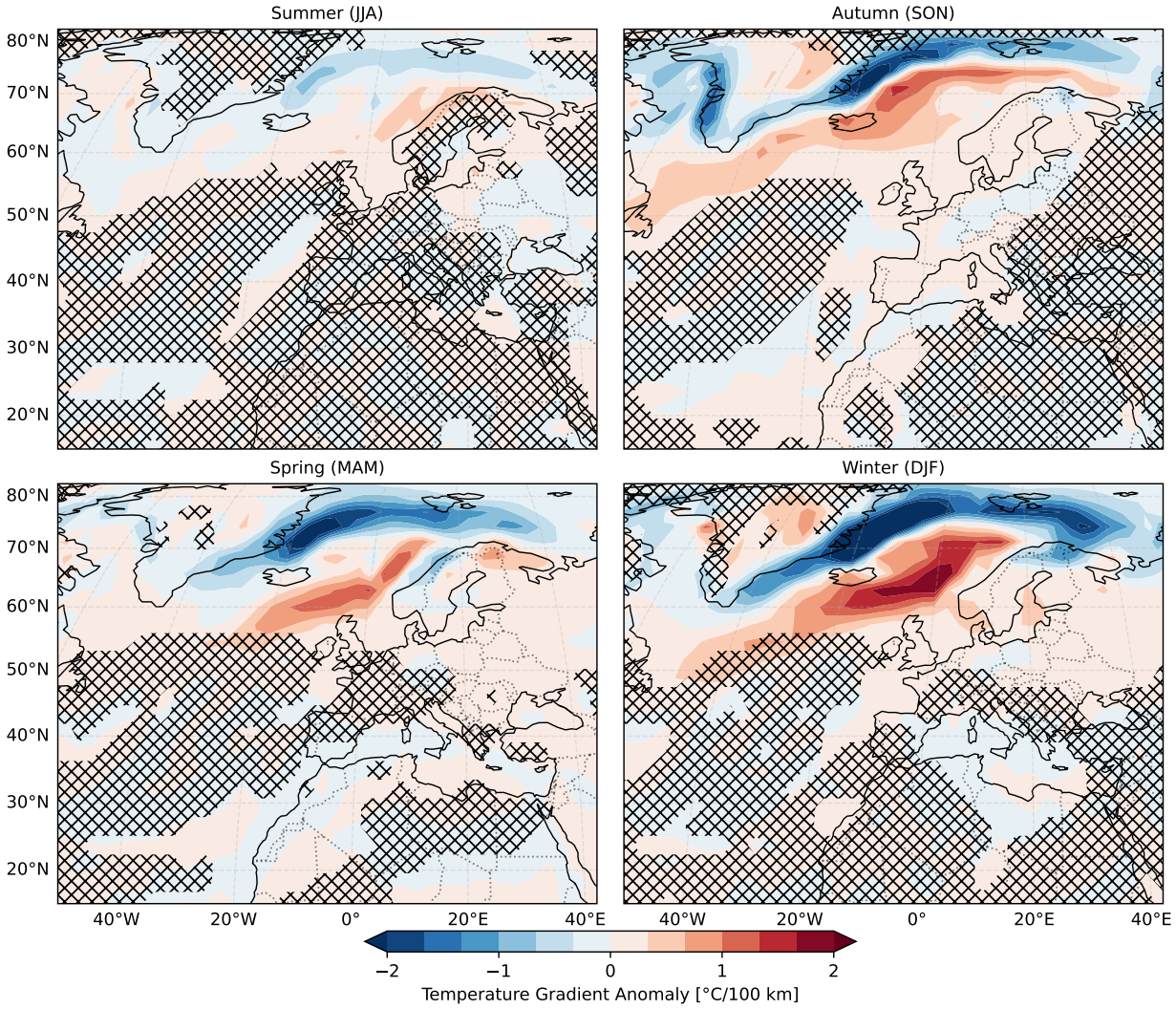


Figure 4.13: Seasonal temperature gradient anomaly, of hosing experiment, between two 10-year periods representing distinct NAO phases: years 50-60 (negative NAO) and years 73-83 (positive NAO). Anomalies are computed as negative NAO period minus positive NAO period. Hatched area corresponds to nonsignificant area.

Analyzing the effect of AMOC weakening during positive and negative NAO phases (Figures 4.14 and 4.15 respectively) reveals a similar pattern of spatial anomalies. In both cases, the temperature gradients are shifted southward. Although the shift does not occur in the exact same region, it demonstrates that an AMOC weakening substantially contributes to a southward displacement of the temperature gradients. During the positive NAO phase (Figure 4.15), the shift in temperature gradient is much more confined to higher latitudes than in the negative NAO phase, supporting the earlier interpretation that the NAO can either amplify or dampen the sea ice expansion initiated by the AMOC weakening. In both NAO phases, an AMOC weakening exerts a broader area of influence across the North Atlantic Ocean, with the temperature gradient shift extending below 50°N along the East Coast of the US, indicating that the NAO impact is more confined to its dipole structure than the AMOC impact. Overall, this anomaly analysis provides insights into the spatial domains of influence of an AMOC weakening and distinct NAO phases.

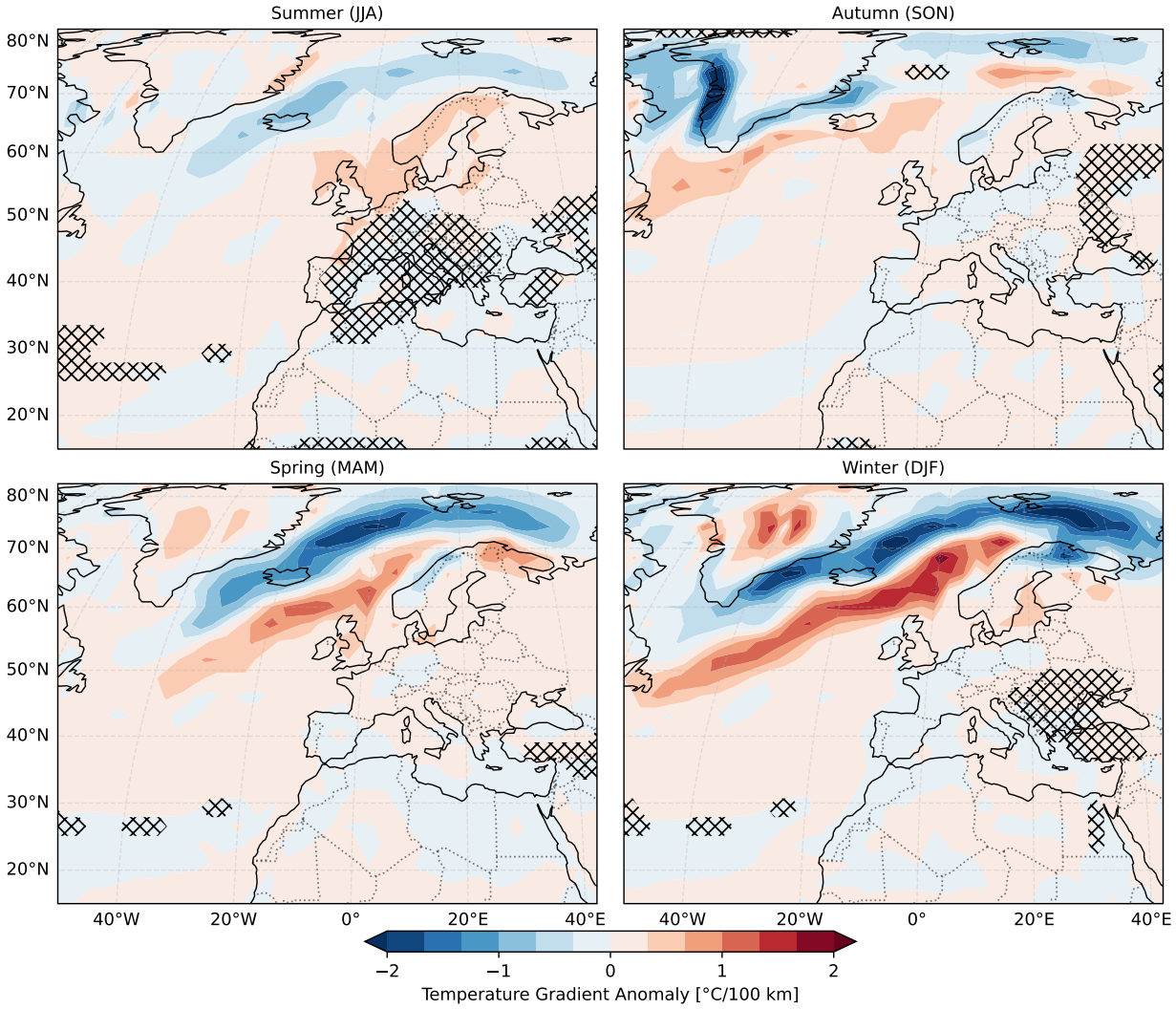


Figure 4.14: Seasonal temperature gradient anomaly of the negative NAO phase (year 50-60), between two experiments representing distinct AMOC strength: hosing (low AMOC strength) and control (high AMOC strength). Anomalies are computed as hosing minus control. Hatched area corresponds to nonsignificant area.

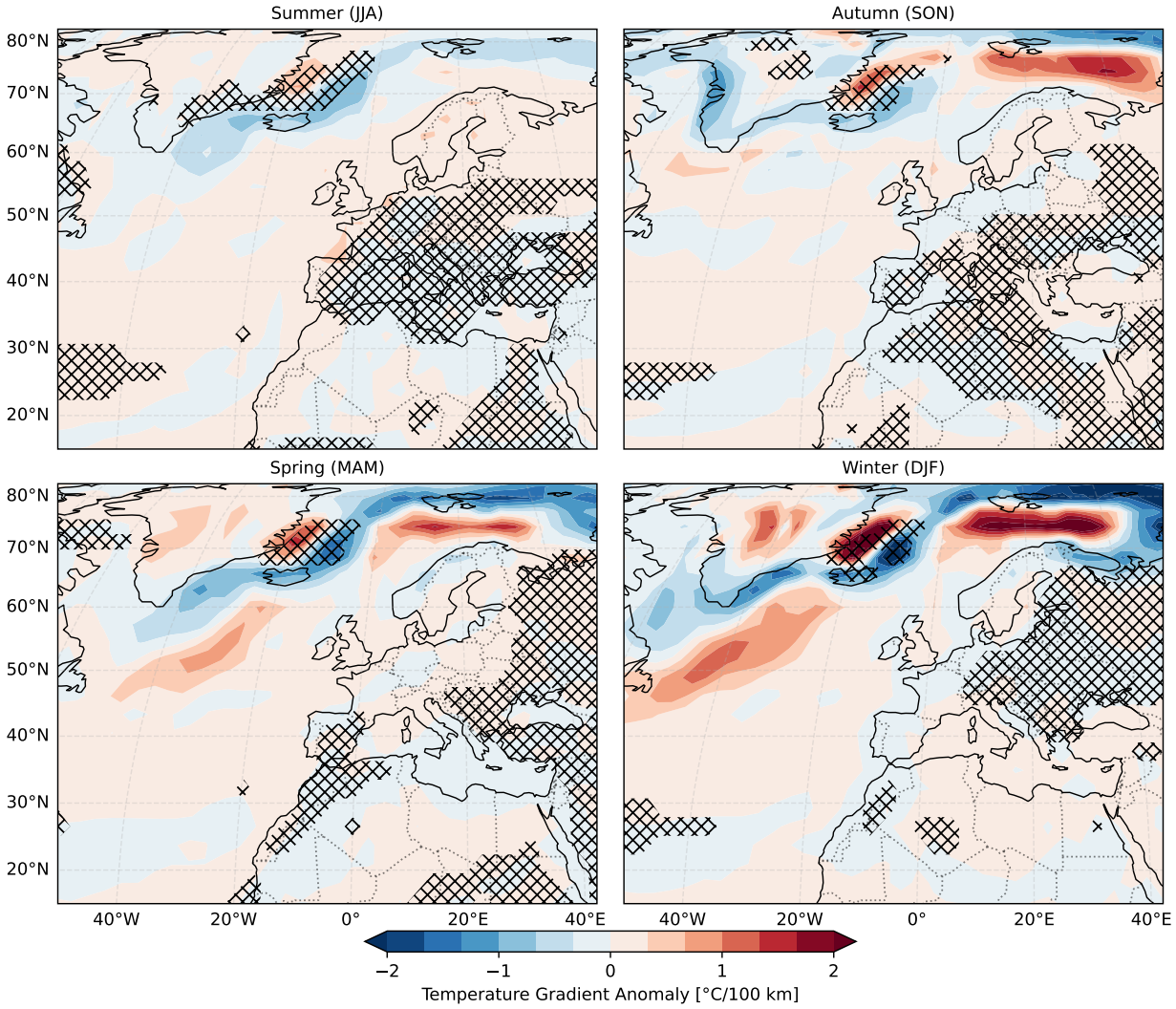


Figure 4.15: Seasonal temperature gradient anomaly of the positive NAO phase (year 73-83), between two experiments representing distinct AMOC strength: hosing (low AMOC strength) and control (high AMOC strength). Anomalies are computed as hosing minus control. Hatched area corresponds to nonsignificant area.

4.2.1 Linear temperature model

The combination of the AMOC and NAO signals yields a substantially improved fit quality for the decadal running mean European temperature, following Equation 4.4, and explains the decadal variability across most experiments (except for the control run, which remains poorly explained). The quality of the multilinear fit is evaluated by the coefficient of determination (r^2), while the regression coefficients (α and β) indicate how the temperature is modulated by the normalized AMOC and NAO respectively, while minimizing the residual error. The coefficient ε corresponds to the baseline mean temperature of each scenario (not the mean

temperature of the fit).

$$T(t) = \alpha \cdot \mathrm{AMOC}'(t) + \beta \cdot \mathrm{NAO}'(t) + \varepsilon \quad \text{with} \quad \mathrm{AMOC}'(t) = \frac{\mathrm{AMOC}(t) - \mu_{\mathrm{AMOC}}}{\sigma_{\mathrm{AMOC}}} \qquad \mathrm{NAO}'(t) = \frac{\mathrm{NAO}(t) - \mu_{\mathrm{NAO}}}{\sigma_{\mathrm{NAO}}} \tag{4.4}$$

In lower-AMOC scenarios, the value of the β coefficient increases markedly, from 0.03 in the control to 0.44 in the r70 experiment, as shown in Table 4.4. This indicates a greater influence of the NAO when the AMOC intensity is reduced, confirming the observations made in Figure 4.7. The AMOC remains the dominant driver in the hosing and r70 experiments, where $\alpha > \beta$. However, the temperature trajectory in r50 is almost entirely explained by the NAO. Comparing the control run with the perturbed experiments, the combination of the AMOC and NAO signals improves the fit quality by a factor of two to three based on r^2.

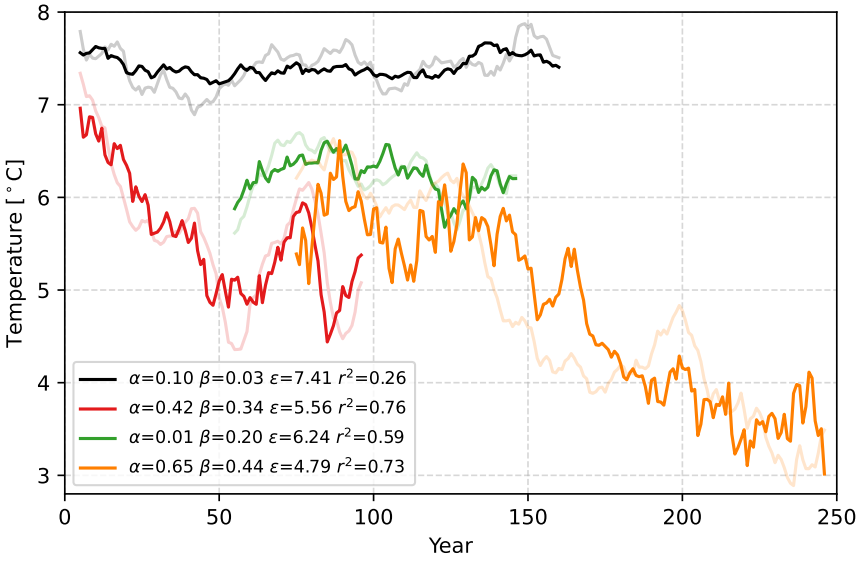


Figure 4.16: Multi-linear fit of European decadal running mean temperature for different experiments (semi-transparent line) for different experiments: control (black), hosing (red), r50 (green) and r70 (orange). The units of α and β are °C.

	Mean AMOC [Sv]	α [°C]	β [°C]	ε [°C]
control	11.35	0.10	0.03	7.41
hosing	6.10	0.42	0.34	5.56
r50	6.31	0.01	0.20	6.24
r70	4.62	0.65	0.44	4.79

Table 4.4: Quantitative comparison of the mean AMOC intensity and the fit coefficients (α, β, ε).

The following Figures 4.17 and 4.18 illustrate the temperature fit decomposed by season and region, respectively, while Table 4.5 provides the metrics of the fit (α, β, ε, r^2). Similar to the covariance analysis in the previous section, this decomposition reveals how the AMOC and NAO modulate the temperature across individual seasons and regions. Physically, oceanic heat

transport (α) and atmospheric heat advection (β) are physically constrained to be positive drivers of European temperature. Negative coefficients reflect optimization artifacts of the linear regression rather than physical cooling mechanisms.

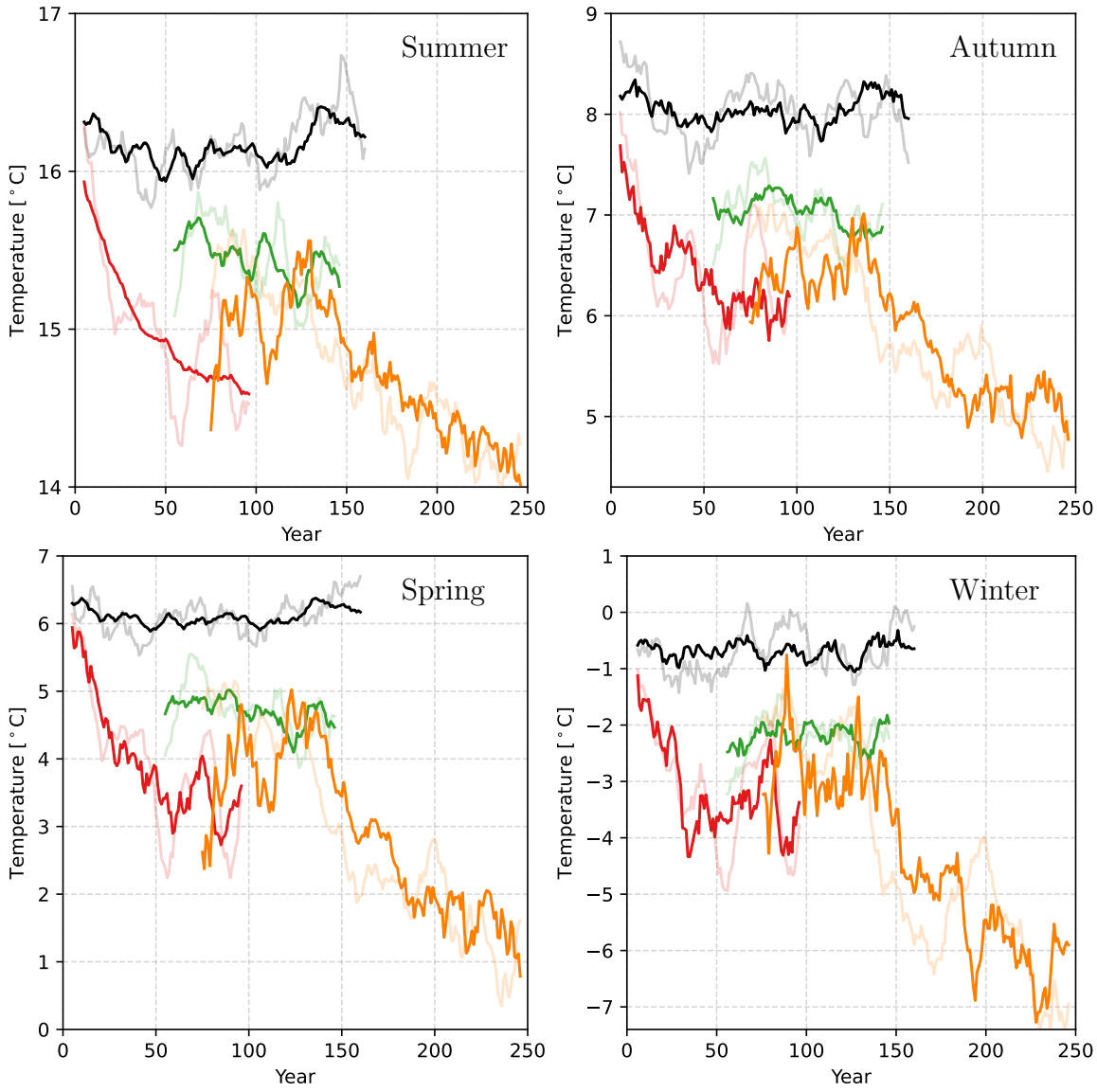


Figure 4.17: Seasonal decomposition of the European temperature decadal running mean (semi-transparent lines). Seasonal decomposition of the decadal running mean temperature fit (opaque lines). Scenarios: control (black), hosing (red), r50 (green), r70 (orange).

Because the AMOC time series has an annual resolution, the normalized signal ($\mathrm{AMOC}'(t)$) remains unchanged across seasons, which isolates the capacity of the NAO signal to explain seasonal temperature variations. The seasonal decomposition confirms that the NAO modulation is strongly season-dependent. During winter, the atmospheric coupling coefficient reaches its maximum across all perturbed scenarios, starting at $\beta = 0.18$ in the r50 experiment and peaking at $\beta = 0.72$ in the r70 experiment. In contrast, summer shows negligible sensitivity to the NAO index across all experiments ($\beta = -0.01$ to 0.11). These findings demonstrate that the NAO impact on European temperatures peaks in winter, with its contribution becoming even more pronounced under an AMOC weakening.

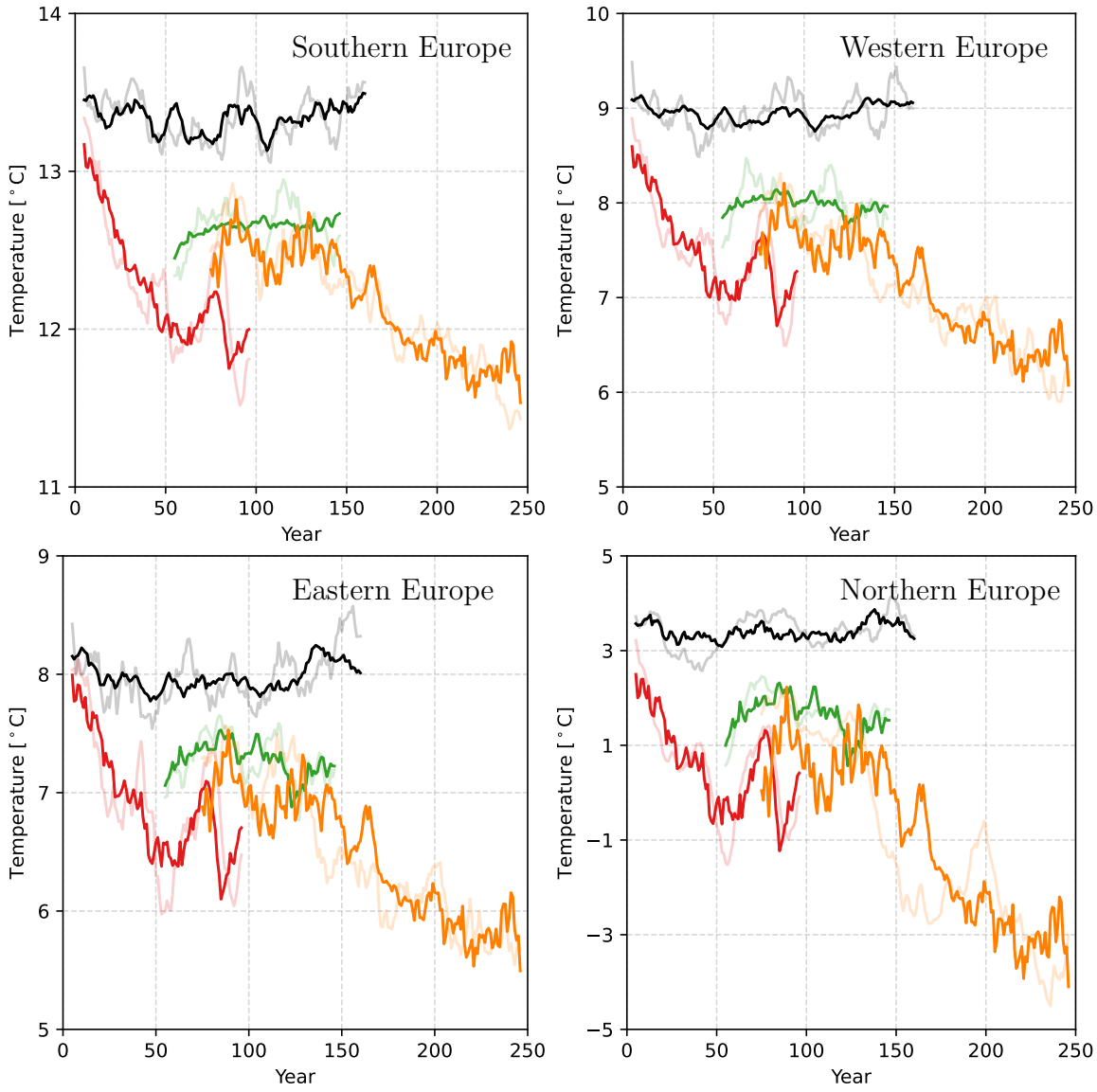


Figure 4.18: Spatial decomposition of the European temperature decadal running mean (semi-transparent lines). Spatial decomposition of the decadal running mean temperature fit (opaque lines). Scenarios: control (black), hosing (red), r50 (green), r70 (orange).

For spatial decomposition, AMOC$'(t)$ and NAO$'(t)$ both remain unchanged across all regional temperatures. The spatial decomposition highlights a pronounced North-South gradient in sensitivity to both oceanic and atmospheric drivers. Northern Europe exhibits the highest sensitivity to both AMOC weakening ($\alpha = 0.55$ in hosing and $\alpha = 1.18$ in r70) and NAO phase shifts ($\beta = 0.58$ in hosing and $\beta = 0.76$ in r70). Conversely, Southern Europe displays the lowest sensitivity ($\alpha = 0.24 - 0.32$, $\beta = 0.11 - 0.16$ under low-AMOC conditions). Situated farther south from the sea ice feedback area, it remains buffered against cold-air advection, contributing less than 11% to the overall European temperature variance (as observed in Table 4.1). Finally, the fit metrics provide the physical mechanism behind the r50 experiment. Although the AMOC intensity increases linearly in r50, regional temperatures remain on a persistent cold plateau. In Table 4.5, $\alpha \approx 0.00$ across all seasons and all regions in r50, whereas the NAO sensitivity coefficient remains substantial ($\beta = 0.38$ °C in Northern Europe, $r^2 = 0.65$). This confirms that temperature variations during the r50 plateau are governed primarily by NAO forcing. However, during the hosing and r70 experiments, the AMOC remains the most predominant

driver of the temperature ($\alpha > \beta$) across all seasons and regions.

A	control	hosing	r50	r70
Summer	0.10, 0.03, 16.16	0.37, -0.01, 15.00	-0.04, 0.10, 15.45	0.35, 0.11, 14.74
	0.36	0.67	0.32	0.66
Autumn	0.09, 0.09, 8.05	0.46, 0.19, 6.45	-0.07, 0.13, 7.03	0.55, 0.18, 5.84
	0.23	0.51	0.33	0.64
Winter	0.10, 0.14, -0.69	0.42, 0.56, -3.14	0.08, 0.18, -2.20	1.09, 0.72, -4.36
	0.16	0.66	0.26	0.68
Spring	0.12, 0.00, 6.11	0.72, 0.29, 3.93	-0.11, 0.15, 4.70	1.02, 0.19, 2.91
	0.23	0.73	0.28	0.65
B	control	hosing	r50	r70
Southern EU	0.08, -0.06, 13.34	0.32, 0.11, 12.27	0.05, 0.03, 12.64	0.24, 0.16, 12.17
	0.36	0.77	0.12	0.81
Western EU	0.09, -0.03, 8.95	0.35, 0.22, 7.49	0.00, 0.08, 7.99	0.35, 0.28, 7.10
	0.21	0.76	0.16	0.75
Eastern EU	0.11, 0.02, 7.98	0.35, 0.23, 6.90	-0.00, 0.14, 7.28	0.33, 0.27, 6.47
	0.27	0.69	0.50	0.75
Northern EU	0.10, 0.11, 3.40	0.55, 0.58, 0.54	0.01, 0.38, 1.63	1.18, 0.76, -0.96
	0.21	0.74	0.65	0.69

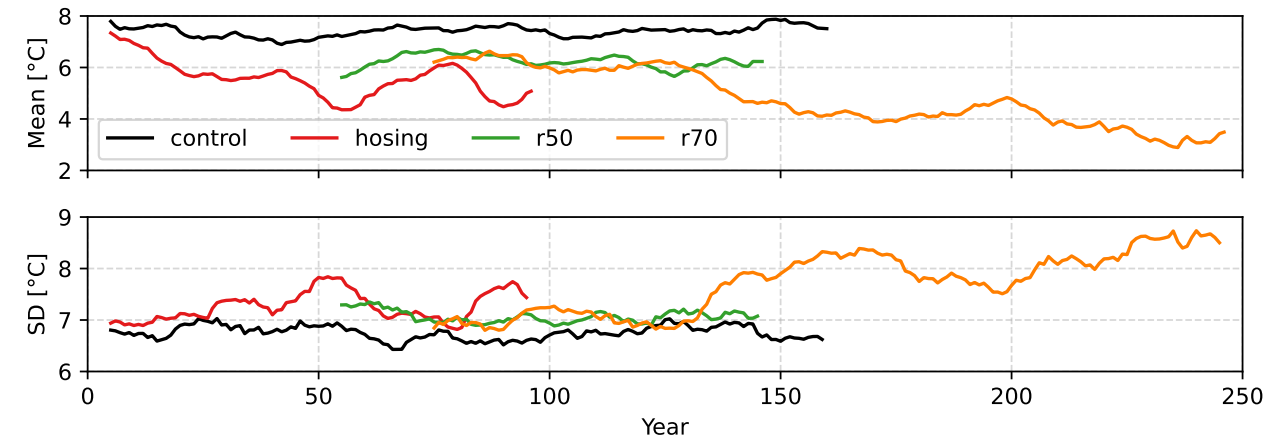
Table 4.5: The upper table **A** corresponds to the temperature fit metric decomposed into four seasons when all regions are taken into account. The lower table **B** corresponds to the temperature fit metric decomposed into four regions when all seasons are taken into account. For each case, 2 lines are provided. First line provides the coefficients α, β, ε. Second line provides the coefficient of determination r^2.

Together, these results establish the full coupling mechanism between the AMOC and the NAO, providing a better understanding of European temperatures under a low-AMOC state. The AMOC drives the temperature at lower frequencies than the NAO, a reduction in its intensity decreases the poleward heat flux transported by the oceanic circulation. This causes a widespread cooling across the North Atlantic and triggers sea ice expansion. The covariance analysis demonstrates that the European temperature signal is dominated by Northern Europe and the winter season signals across all scenarios, a dominance that becomes even more pronounced as the AMOC intensity is reduced. Additionally, the atmospheric circulation driven by the NAO governs the advection of the air masses flowing toward Europe. Because the NAO is primarily a winter phenomenon and interacts with the sea ice expansion, its influence is concentrated over Northern Europe and during the winter season as well. A negative NAO phase amplifies the cooling effect by displacing the high-latitude temperature gradient closer to Northern Europe. In contrast, a positive NAO phase exerts the opposite effect, confining the temperature gradient to higher latitudes and thereby dampening the cooling effect on Northern Europe. A key element of this coupling mechanism is the positive sea ice expansion feedback, which can be triggered by either an AMOC weakening or a negative NAO phase. Finally, the influence of the NAO increases significantly as the AMOC weakens, which primarily affects Northern Europe and the winter season.

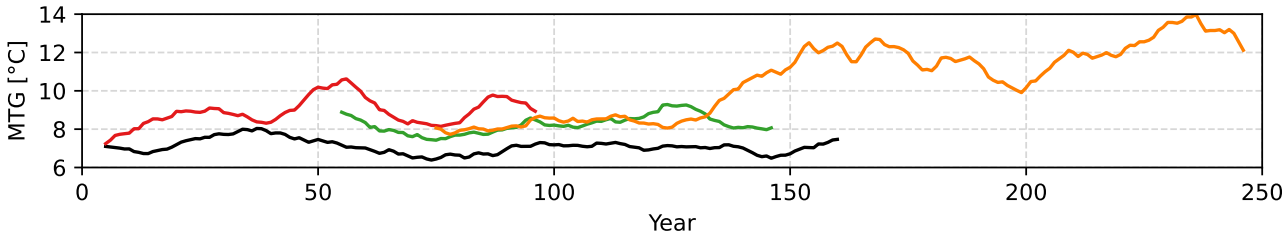
4.3 Temperature volatility in Europe

While the previous sections focused on decadal European temperature variability driven by the coupling between the AMOC and NAO, analyzing mean temperature variations alone does not capture the full climate response. Consequently, this section investigates changes in temperature volatility (quantified using the standard deviation) to evaluate higher-order fluctuations in response to a weakened AMOC.

The standard deviation of the European temperature is presented in Figure 4.19a. The temporal evolution of the standard deviation shows a pronounced mirror symmetry with the corresponding mean temperature. Except for a few anomaly years around year 135, the perturbed experiments (hosing, r50, r70) exhibit a larger standard deviation than the control run (mean of 6.75°C mean), with the mean value rising to 7.06°C in r50 and to 7.72°C in r70. This indicates that perturbed climates have greater dispersion around their mean, particularly when the mean temperature drops. The meridional temperature gradient (MTG), shown in Figure B.4, is a key diagnostic metric for understanding temperature volatility. It is defined as the temperature difference between a subtropical warm box (low latitudes) and a subpolar cold box (high latitudes) within the North Atlantic Ocean (see Figure B.3). The MTG is the primary source of the atmospheric baroclinicity that fuels storm formation, and is directly related to the speed of the mid-latitude westerly jet through the thermal wind balance, as described by Vacca et al. 2025 [44] and Van Westen, Kliphuis, and Dijkstra 2024 [45]. Additionally, the sea ice edge amplifies the atmospheric MTG over the Atlantic Ocean during the winter months, which strengthens the jet stream and enhances storm track activity over Northwestern Europe (Westen and Baatsen. 2025 [40]). Because this research question focuses on Europe, the Figure 4.19b provides the MTG across Europe (boxes are defined in Figure B.5), which reflects the reservoir of available potential energy, over Europe, that feeds baroclinic instability. The trajectories of the European MTG and the associated temperature standard deviations are very similar, suggesting that baroclinic instability contributes to temperature volatility in Europe.



(a)



(b)

Figure 4.19: (a) Decadal running mean and standard deviation of European temperature (b) Decadal running mean meridional temperature gradient (MTG) across Europe.

4.3.1 Temporal volatility analysis

The following temporal volatility analysis focuses on the seasonal and regional decompositions of the time series introduced in Figure 4.19b. The framework used for this purpose is similar to the European temperature covariance analysis conducted in Section 4.1.1.

In general, the annual temperature cycle is approximately sinusoidal, with the steepest intra-seasonal temperature slope occurring in autumn and spring. If the standard deviation were computed directly from monthly raw temperature series within each season, it would artificially exhibit larger values in autumn and spring due to the seasonal transition cycle. To mask this geophysical phenomenon and ensure comparable seasons, the following expression is used to compute the interannual seasonal variability (via the standard deviation) originating from season s over a time window of Y years (see Figure 4.20),

$$\begin{aligned}
\bar{T}_{y,s} &= \frac{1}{3}\sum_{m\in M_s} T_{y,m} \\
\bar{T}'_{y,s} &= \bar{T}_{y,s} - \mathrm{Trend}_{y,s} \quad \text{with} \quad \mathrm{Trend}_{y,s} = \frac{1}{W}\sum_{k=y-\lfloor W/2\rfloor}^{y+\lfloor W/2\rfloor} \bar{T}_{k,s} \\
\sigma_s &= \sqrt{\frac{1}{Y-1}\sum_{y=1}^{Y}\left(\bar{T}'_{y,s}-\mu_s\right)^2} \quad \text{with} \quad \mu_s = \frac{1}{Y}\sum_{y=1}^{Y}\bar{T}'_{y,s}
\end{aligned} \tag{4.5}$$

The monthly temperature ($T_{y,m}$) is defined for year $y \in \{1, 2, \ldots, Y\}$ and month $m \in \{1, 2, \ldots, 12\}$. For a specific season $s \in \{\text{Summer (JJA)}, \text{Autumn (SON)}, \text{Winter (DJF)}, \text{Spring (MAM)}\}$, the seasonal mean temperature in year y, denoted as $\bar{T}_{y,s}$ where M_s is the set of months corresponding to season s. To isolate low-frequency climate drift variability, the detrended seasonal anomaly $\bar{T}'_{y,s}$ is obtained by subtracting a W-year centered moving average trend ($\text{Trend}_{y,s}$) from $\bar{T}_{y,s}$. The seasonal standard deviation (σ_s) is then calculated over the centered running window as the sample standard deviation of these detrended anomalies $\bar{T}'_{y,s}$ around their window mean μ_s.

The mean standard deviation values, provided in Table 4.6, reveal a clear pattern. Winter exhibits the largest standard deviation (0.98°C to 1.31°C), followed by spring (0.78°C to 1.05°C), autumn (0.60°C to 0.80°C), and summer (0.42°C to 0.52°C). The winter values are more than double those of summer. Hosing consistently increases the temperature standard deviation across all seasons relative to the control run. The largest increases occur in spring (+0.25°C) and autumn (+0.20°C), suggesting that the hosing scenario amplifies interannual temperature swings. In r50, the temperature standard deviation decreases significantly across all seasons, returning near or slightly below control levels (as observed in Figure 4.20). The r70 exhibits the second largest standard deviation after hosing, where spring and autumn also experience the largest standard deviation increase. While winter remains the most dominant season under weakened AMOC, transition seasons (spring and autumn) show the largest increase relative to the control run.

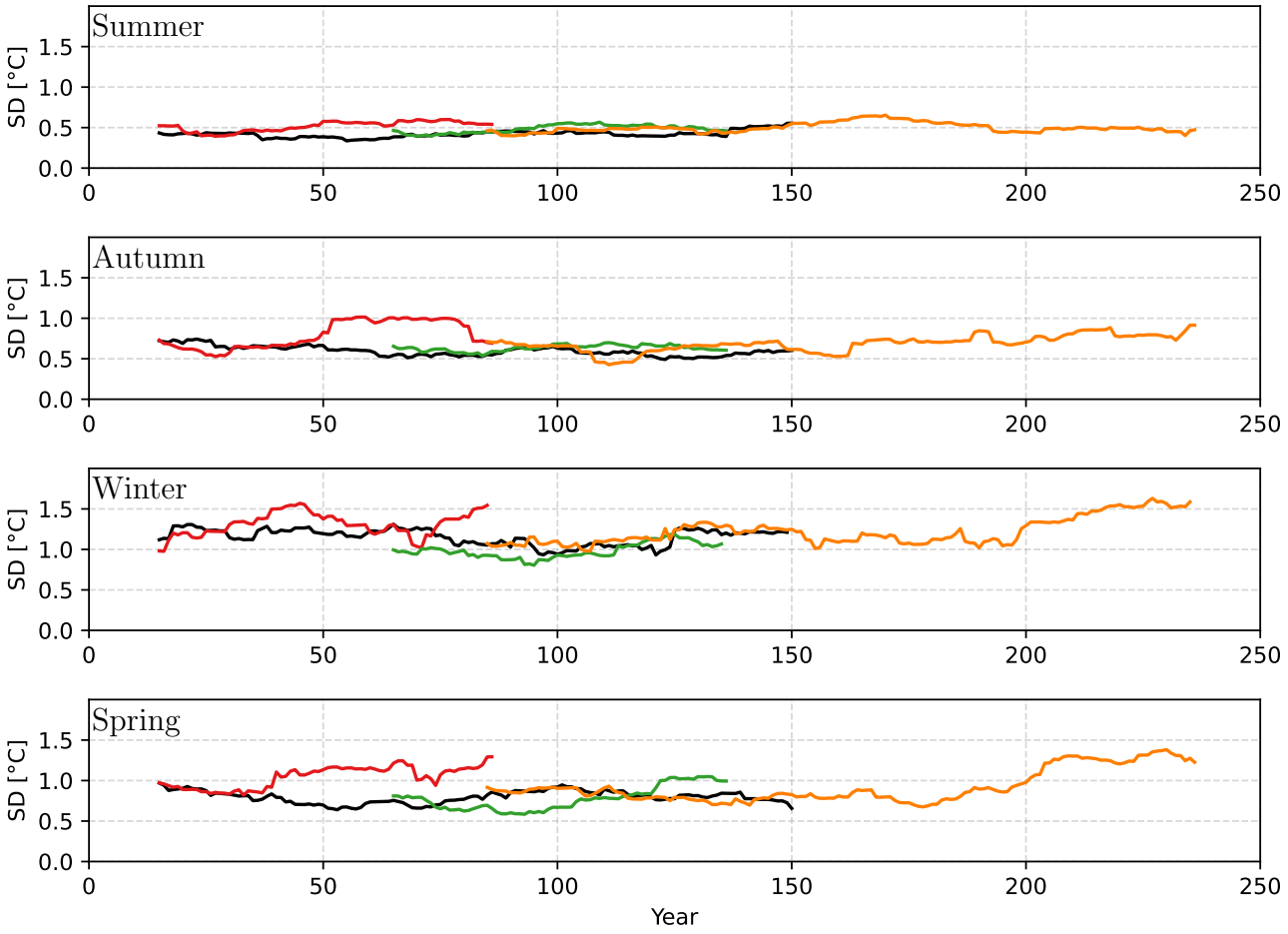


Figure 4.20: Seasonal decomposition of the European temperature 30-year running standard deviation mean. Scenarios: control (black), hosing (red), r50 (green), r70 (orange).

	Mean standard deviation [°C]			
30-year mean	Summer (JJA)	Autumn (SON)	Winter (DJF)	Spring (MAM)
control	0.42	0.60	1.15	0.80
hosing	0.52	0.80	1.31	1.05
r50	0.48	0.63	0.98	0.78
r70	0.50	0.69	1.22	0.92

Table 4.6: 30-years running mean standard deviation of European temperature originating from each season across control, hosing, and recovery scenarios.

Because regions contain an unequal number of grid points, spatially averaging them into a single reference point isolates the large-scale regional response from the spatial noise and enables regional comparisons. Similar to Equation 4.5, the following expression is used to compute the interannual regional variability (via the standard deviation) originating from region r over a time window of Y years (see Figure 4.21),

$$\begin{aligned} \bar{T}_{y,r} &= \frac{1}{N_r} \sum_{i \in C_r} T_{y,i} \\ \bar{T}'_{y,r} &= \bar{T}_{y,r} - \text{Trend}_{y,r} \quad \text{with} \quad \text{Trend}_{y,r} = \frac{1}{W} \sum_{k=y-\lfloor W/2 \rfloor}^{y+\lfloor W/2 \rfloor} \bar{T}_{k,r} \\ \sigma_r &= \sqrt{\frac{1}{Y-1} \sum_{y=1}^{Y} \left(\bar{T}'_{y,r} - \mu_r\right)^2} \quad \text{with} \quad \mu_r = \frac{1}{Y} \sum_{y=1}^{Y} \bar{T}'_{y,r} \end{aligned} \tag{4.6}$$

Here, the temperature $T_{y,i}$ is defined for year $y \in \{1, 2, \ldots, Y\}$ at grid point i. For a specific spatial region r, C_r represents the set of grid points belonging to region r, and N_r is the total number of grid points in that region (see Table 3.4). The spatially averaged regional mean temperature in year y is denoted as $\bar{T}_{y,r}$. To isolate low-frequency climate drift, the detrended regional anomaly $\bar{T}'_{y,r}$ is obtained by subtracting a W-year centered moving average trend ($\text{Trend}_{y,r}$) from $\bar{T}_{y,r}$. The regional standard deviation (σ_r) is calculated as the sample standard deviation of these detrended regional anomalies $\bar{T}'_{y,r}$ around their mean μ_r.

In addition to the seasonal analysis, Table 4.7 provides the mean standard deviation values across regions for all scenarios. In the control experiment, Eastern Europe exhibits the highest standard deviation. While classical continentality attributes this difference primarily to the contrast in heat capacity, where the ocean acts as a thermal buffer damping temperature swings in coastal regions, Dommenget 2009 [46] demonstrates that continental lands experience amplified variability due to the combined effects of low soil heat capacity and atmospheric radiative feedbacks driven by the oceans. Under AMOC weakening, the standard deviation across all regions increases. The most pronounced impact occurs in Northern Europe, where the values nearly double from 0.54°C in the control run to 1.03°C under hosing. In the perturbed climate scenarios (hosing, r50, r70), Northern Europe (high latitudes) always exhibits a larger standard deviation than Southern Europe (low latitudes), demonstrating a clear latitudinal dependence in temperature fluctuations. As demonstrated in previous sections, AMOC weakening predominantly affects Northern Europe temperatures, with an attenuated impact on lower-latitude regions. This indicates that an AMOC weakening not only cools Northern Europe with a larger amplitude than other regions but also induces greater temperature volatility (an average of 49% higher than in other regions). Similar to the seasonal analysis in Table 4.6, the standard

deviation in r50 returns near or slightly below control levels, whereas r70 maintains the second largest standard deviation after hosing.

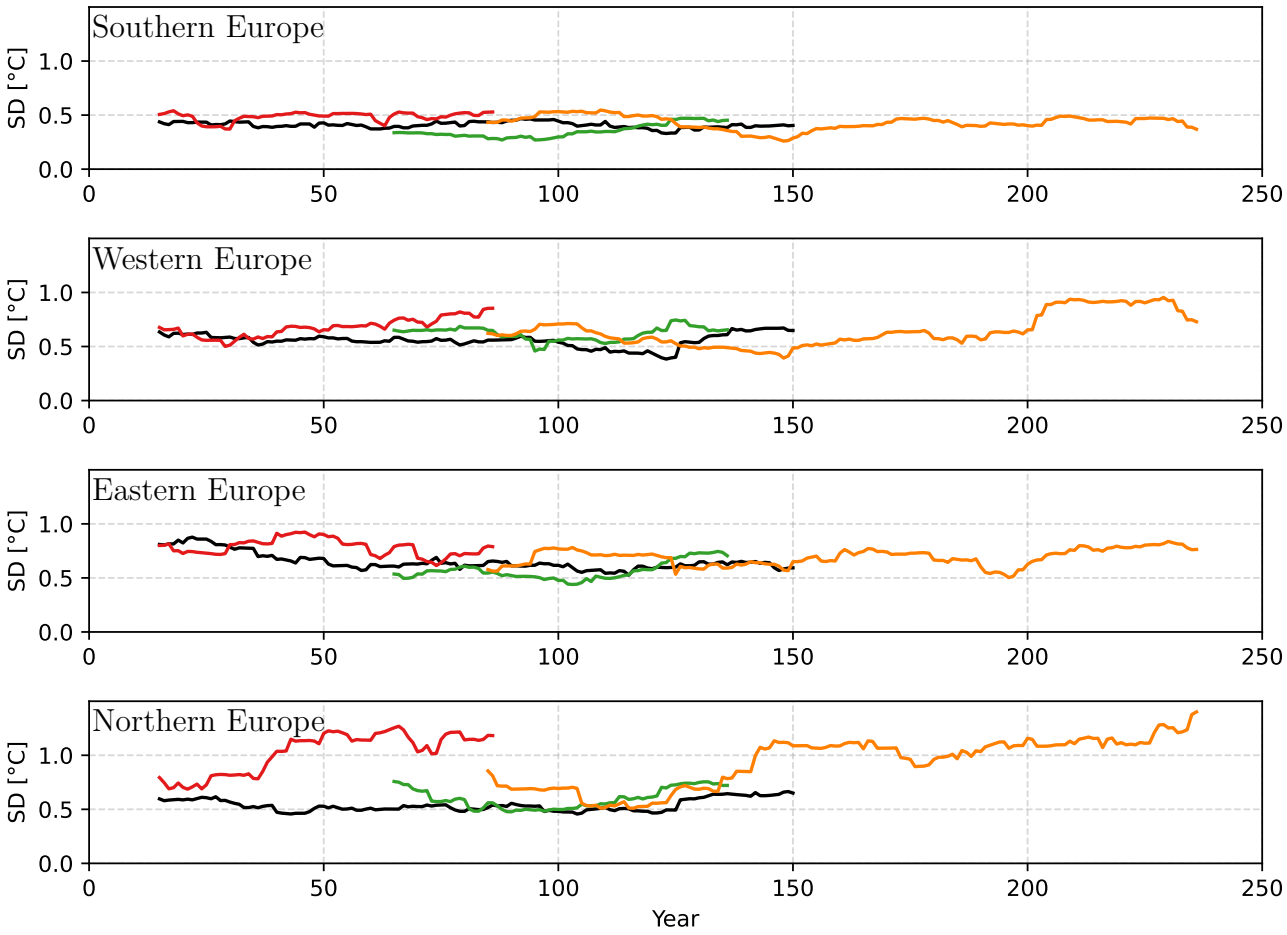


Figure 4.21: Regional decomposition of the European temperature 30-years running standard deviation mean. Scenarios: control (black), hosing (red), r50 (green), r70 (orange).

	Mean standard deviation [°C]			
30-year mean	Southern Europe	Western Europe	Eastern Europe	Northern Europe
control	0.41	0.56	0.65	0.54
hosing	0.49	0.68	0.78	1.03
r50	0.35	0.62	0.57	0.60
r70	0.43	0.65	0.69	0.93

Table 4.7: 30-years running mean standard deviation of European temperature originating from each region across control, hosing, and recovery scenarios.

To provide a complete assessment, Table B.2 presents a regional–seasonal decomposition, revealing a distinct and non-uniform European volatility response across regions. Unlike previous analyses that were masked by spatial or temporal averaging, this breakdown isolates regional dynamics. The lower winter sensitivity observed across Europe in Table 4.6 is primarily driven by Southern, Western, and Eastern Europe, where the increase in winter standard deviation is extremely low, and Eastern Europe even experiences a decrease of winter mean standard deviation. This reduction can be attributed to the intensification of the westerly jet stream,

which suppresses atmospheric blocking events, as explained by Meccia et al. 2024 [47] . In contrast, Northern Europe experiences the largest increase in temperature standard deviation across all seasons, with a particularly enhanced increase during winter, driven by its proximity to the expanding Arctic sea-ice boundary.

Similar to the previous covariance analysis, Table 4.8 evaluates the percentage of European MTG standard deviation (C_i) originating from season i,

$$C_i = \frac{\frac{1}{4} \cdot \mathrm{Cov}(\mathrm{MTG}_i, \mathrm{MTG}_{\mathrm{EU}})}{\mathrm{Var}(\mathrm{MTG}_{\mathrm{EU}})} \quad \text{with} \quad \mathrm{MTG}_{\mathrm{EU}}(t) = \sum_{i=1}^{4} \frac{1}{4} \mathrm{MTG}_i(t) \tag{4.7}$$

Unsurprisingly, Tables 4.2 and 4.8 share a similar pattern in terms of seasonal dominance across the perturbed scenarios. Because the cooling is strongly concentrated at high latitudes rather than low latitudes, this regional contrast directly enhances the $\mathrm{MTG}_{\mathrm{EU}}$ ($\mathrm{MTG}_{\mathrm{EU}} = T_{\mathrm{South}} - T_{\mathrm{North}}$). Consequently, the seasons that govern European mean temperature fluctuations (winter and spring) are the same as those that govern $\mathrm{MTG}_{\mathrm{EU}}$ fluctuations. A deeper analysis, provided in Table B.1, shows that the $\mathrm{MTG}_{\mathrm{EU}}$ is almost entirely driven by fluctuations in the Northern box, accounting for 97.86% of the European MTG variance in the control experiment, and rising to 145.86% in the hosing scenario. The negative values for the Southern box (-45.86% in hosing, -7.58% in r50, -21.38% in r70) indicate that this domain is either anti-correlated or negligible relative to the massive high-latitude variance. This asymmetry aligns with the low Southern European contribution to the temperature variance, as shown in Table 4.2. These results suggest that European baroclinic instabilities are primarily driven by an expanded Arctic sea ice boundary that sharpens the European MTG.

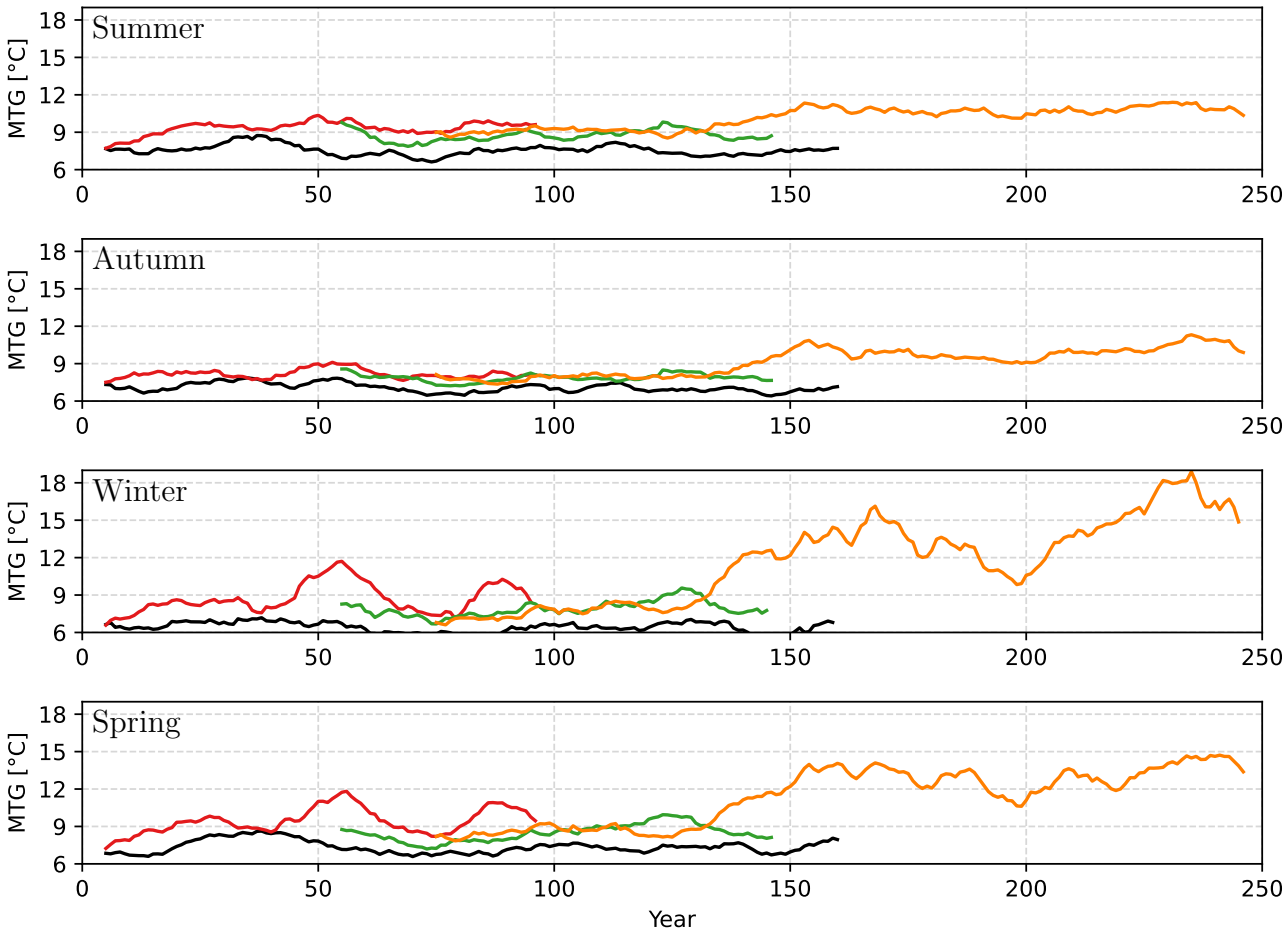


Figure 4.22: Seasonal decomposition of the MTG_{EU} decadal running standard deviation mean. Scenarios: control (black), hosing (red), r50 (green), r70 (orange).

	Weighted covariance decomposition [%]			
10-year mean	Summer (JJA)	Autumn (SON)	Winter (DJF)	Spring (MAM)
control	22.70	19.60	24.67	33.03
hosing	15.31	10.30	40.13	34.26
r50	21.23	13.21	31.28	34.28
r70	11.05	14.25	44.96	29.74

Table 4.8: Percentage of the European MTG originating from each season across control, hosing, and recovery scenarios.

4.3.2 Spatial volatility analysis

In addition to the time series analysis, spatial variance analysis completes the broader assessment of the North Atlantic region across all seasons. The purpose is to characterize the temperature variance of the North Atlantic Ocean and link it to European temperature fluctuations.

Before assessing how AMOC weakening and NAO phases perturb temperature fluctuations, the key features of the linearly detrended seasonal temperature standard deviation in the control experiment are established using Figure B.6. In winter, Europe reveals a clear west-east

standard deviation gradient, which confirms the continentality effect found previously in the regional analysis. Higher standard deviation values are concentrated along the sea ice boundary from spring to autumn, peaking in winter, which is attributed to the seasonal sea ice formation and melting.

Figure 4.23 presents the standard deviation anomalies between negative and positive NAO phases, revealing pronounced positive anomalies in the Nordic Seas in winter. While the NAO is primarily a winter phenomenon, the effect of an altered atmospheric circulation volatility is also visible in autumn and spring. Anomalies across individual periods relative to the control run (see Figures B.7 and B.8) show that an AMOC weakening induces an increase in the standard deviation in the North Seas during winter for both NAO phases. This indicates that under a low-AMOC state, the NAO phase, by governing the atmospheric circulation, can be a source of additional fluctuation. This contrast demonstrates that a negative NAO phase acts as an amplifier of AMOC-induced temperature fluctuations over Europe by shifting the sea ice edge and thermal gradients closer to Northern Europe, whereas a positive NAO phase attenuates these fluctuations.

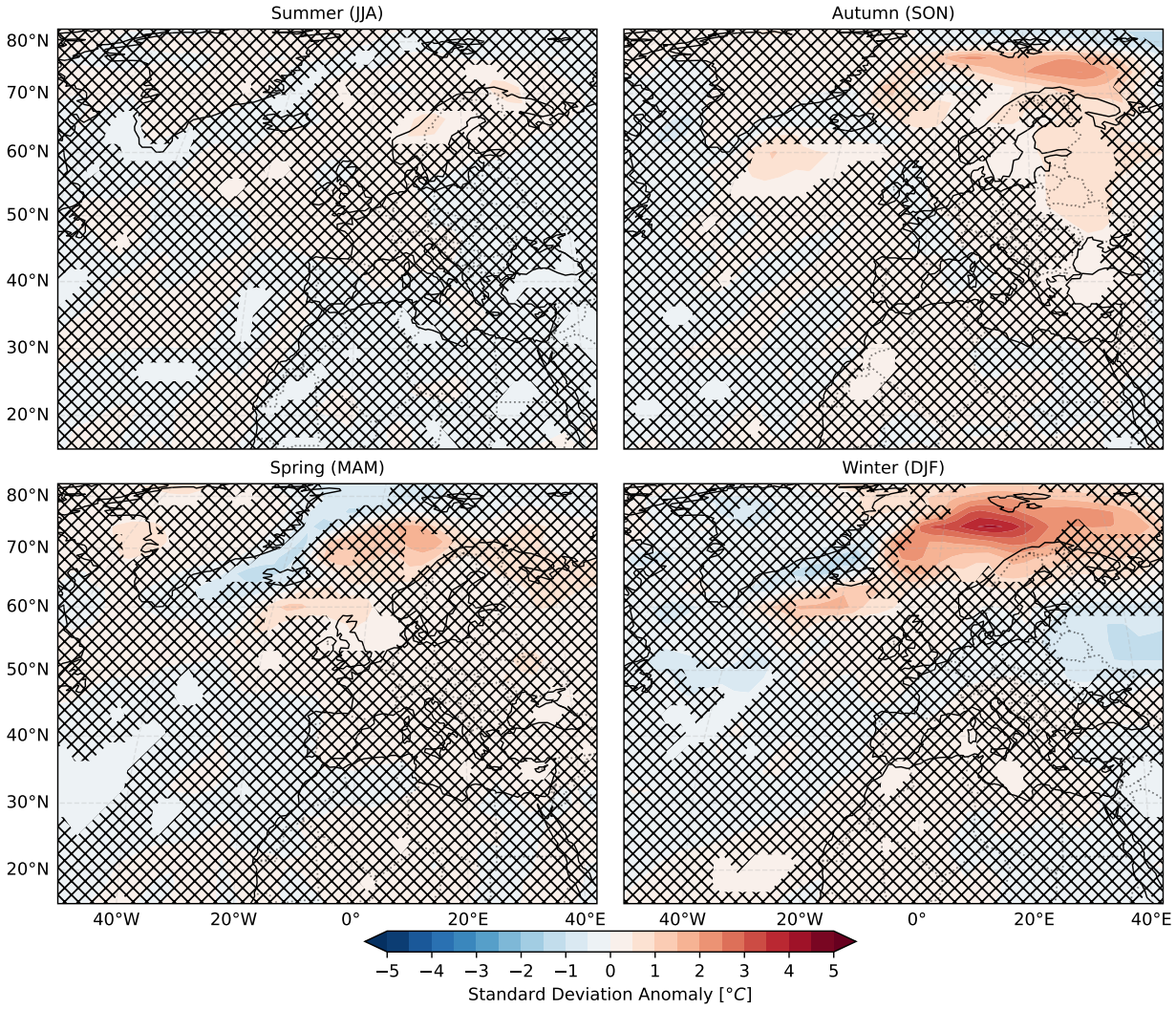


Figure 4.23: Standard deviation anomaly, of the hosing experiment, between two periods representing distinct NAO phases: years 40-66 (negative NAO) and years 67-93 (positive NAO). Anomalies are computed as negative NAO minus positive NAO period. Hatched area corresponds to nonsignificant area.

For long-term anomalies between low-AMOC state and the control run, Figure 4.24 reveals a strong positive anomaly signal from autumn to spring, peaking in winter. The standard deviation of European temperature increases across all seasons with a more pronounced effect in Northern Europe during winter. This aligns with the regional-seasonal analysis presented in Table B.2, confirming that temperature standard deviation increases most in regions and seasons where the cooling effect is most pronounced, triggered by the sea ice boundary. These findings are supported by Patrizio et al. 2026 [48] who studied the subpolar North Atlantic (SPNA) variability under gradually declining AMOC using the Community Earth System Model version 1 (CESM1) and linked this enhanced variability to convection-salinity-sea ice feedbacks. The anomaly amplitude is larger in the Northern European box than the Southern European box (boxes defined in Figure B.5). Consequently, this aligns with the MTG seasonal analysis, confirming that European MTG is almost entirely driven by the Northern box and reinforcing the hypothesis that European baroclinic instabilities are primarily governed by the sea ice boundary.

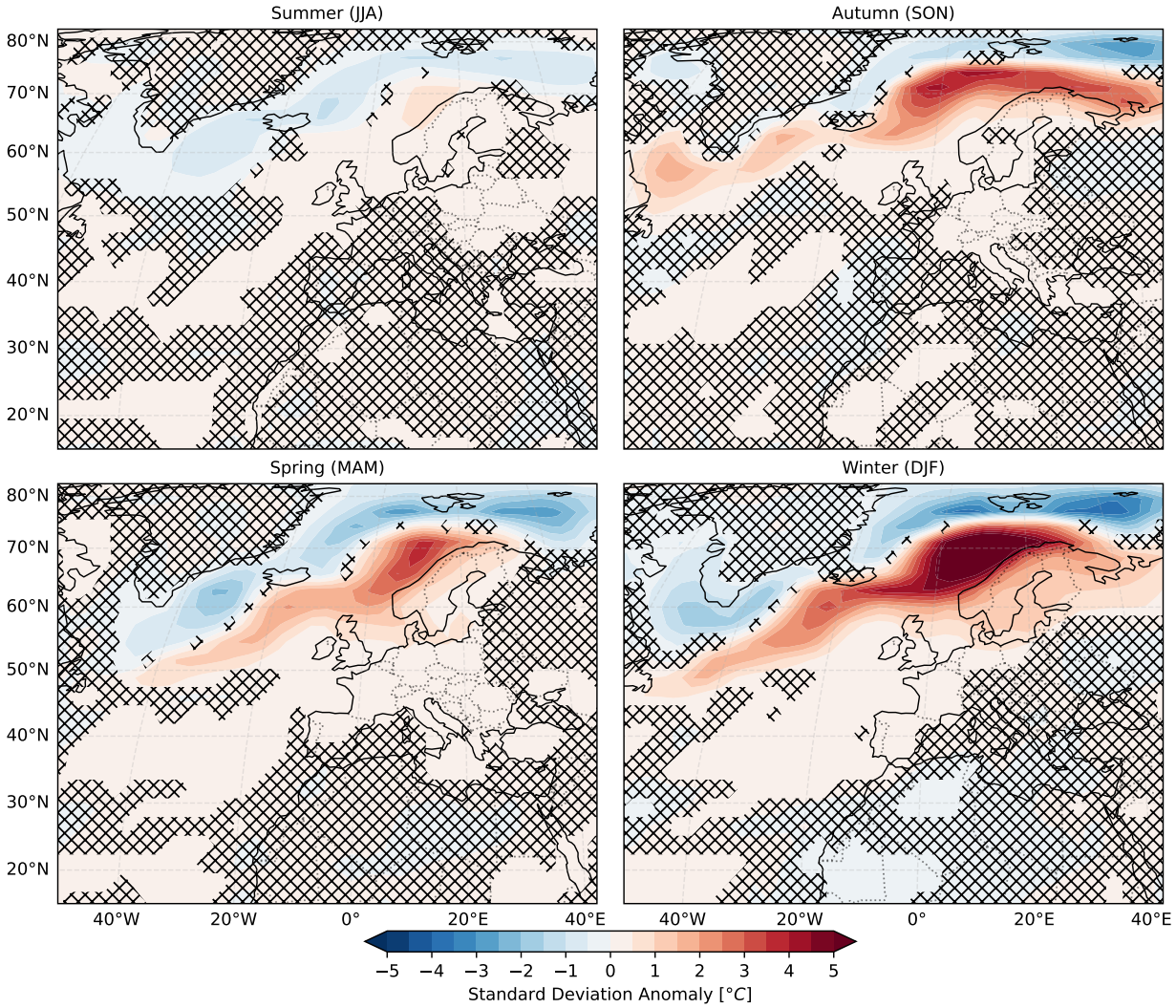


Figure 4.24: Standard deviation anomaly between two periods representing distinct AMOC strength: years 150-250 (r70, low AMOC strength) and years 0-164 (control, high AMOC strength). Anomalies are computed as r70 minus control. Hatched area corresponds to non-significant area.

4.3.3 Advection volatility analysis

In terms of temperature volatility, previous sections identified the key seasons and regions using the seasonal and regional analyses. The advection volatility analysis focuses on the mechanisms underlying these sources of fluctuation in the temperature field. To address this question, the zonal and meridional standard deviation components of the advection Equation 4.8 are used to analyze the cases presented in Figures 4.23 and 4.24 to determine whether fluctuations are dynamically or thermodynamically driven,

$$\begin{aligned} \frac{\partial T}{\partial t} &= -\boldsymbol{V} \cdot \nabla T \\ &= -\left(u_g \frac{\partial T}{\partial x} + v_g \frac{\partial T}{\partial y} \right) \end{aligned} \tag{4.8}$$

This framework separates temperature fluctuations into:

- Dynamical contributions: Fluctuations in the atmospheric circulation, captured by the standard deviations of the zonal (σ_{u_g}) and meridional (σ_{v_g}) geostrophic wind components.
- Thermodynamical contributions: Fluctuations in the temperature field, captured by the standard deviations of the zonal ($\sigma_{\partial T/\partial x}$) and meridional ($\sigma_{\partial T/\partial y}$) temperature gradients.

Case 1: NAO phase dependence

To identify whether temperature fluctuations under different atmospheric regimes (introduced in Figure 4.23) are dynamically or thermodynamically driven, the advection components are decomposed across distinct NAO phases during the hosing experiment in Figures 4.25 and 4.26.

The previous results demonstrate that the standard deviation of winter temperatures is amplified during the negative NAO phase, particularly across the Nordic Seas and Northern Europe (Figure 4.23). Dynamically, the negative NAO phase is characterized by a marked increase in the standard deviation of the geostrophic wind (Figure 4.25), located predominantly in the Nordic Seas and Northern Europe during winter as well. However, the thermodynamic contribution (Figure 4.26) provides a noisy anomaly field with no particular statistically significant regions, indicating that the NAO phase dependence exclusively produces dynamical atmospheric fluctuation over decadal time scale. This dynamical amplification is consistent with the findings of Hurrell and Deser 2010 [49], who showed that while the positive NAO phase is characterized by a stable, persistent westerly flow that continuously buffers Europe with mild maritime air, the negative NAO phase produces a highly volatile jet stream and frequent atmospheric blocking, promoting cold polar air intrusions into lower latitudes.

The decomposition of the wind vector into its zonal and meridional components (Figures 4.27 and 4.28) identifies the primary driver of this substantial dynamical contribution. The results show a dominant signal in the zonal component, demonstrating that, under low-AMOC state, a negative NAO phase amplifies the temperature standard deviation in Northern Europe primarily via larger zonal wind fluctuations during winter. As temperature gradients are displaced southward (Figure 4.13), colder air from Nordic Seas is advected toward Northern Europe with enhanced zonal volatility, resulting in amplified temperature fluctuations.

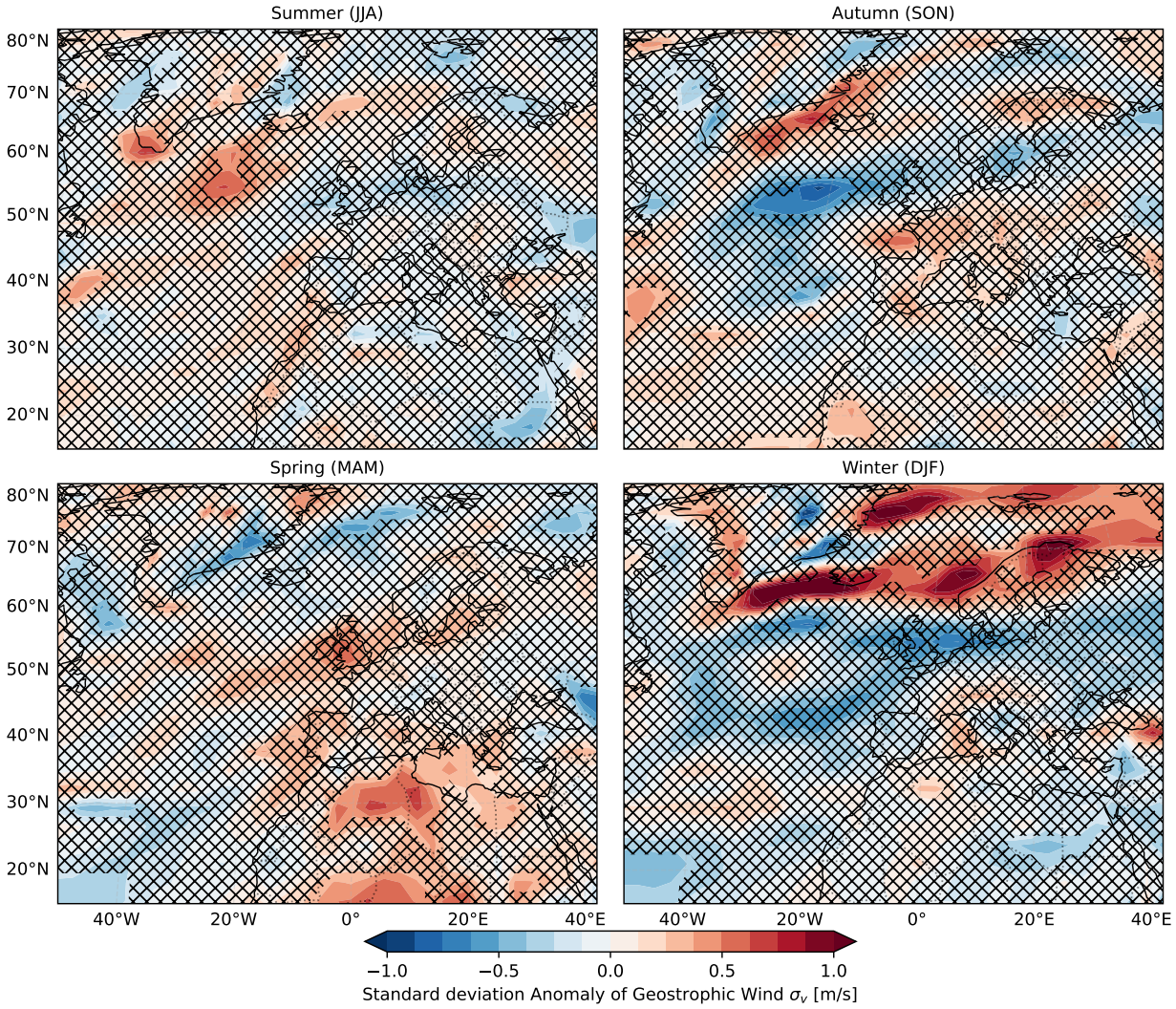


Figure 4.25: Standard deviation anomaly of the geostrophic wind, in the hosing experiment, between two periods representing distinct NAO phases: years 40-66 (negative NAO) and years 67-93 (positive NAO). Anomalies are computed as negative NAO minus positive NAO period. Hatched area corresponds to nonsignificant area.

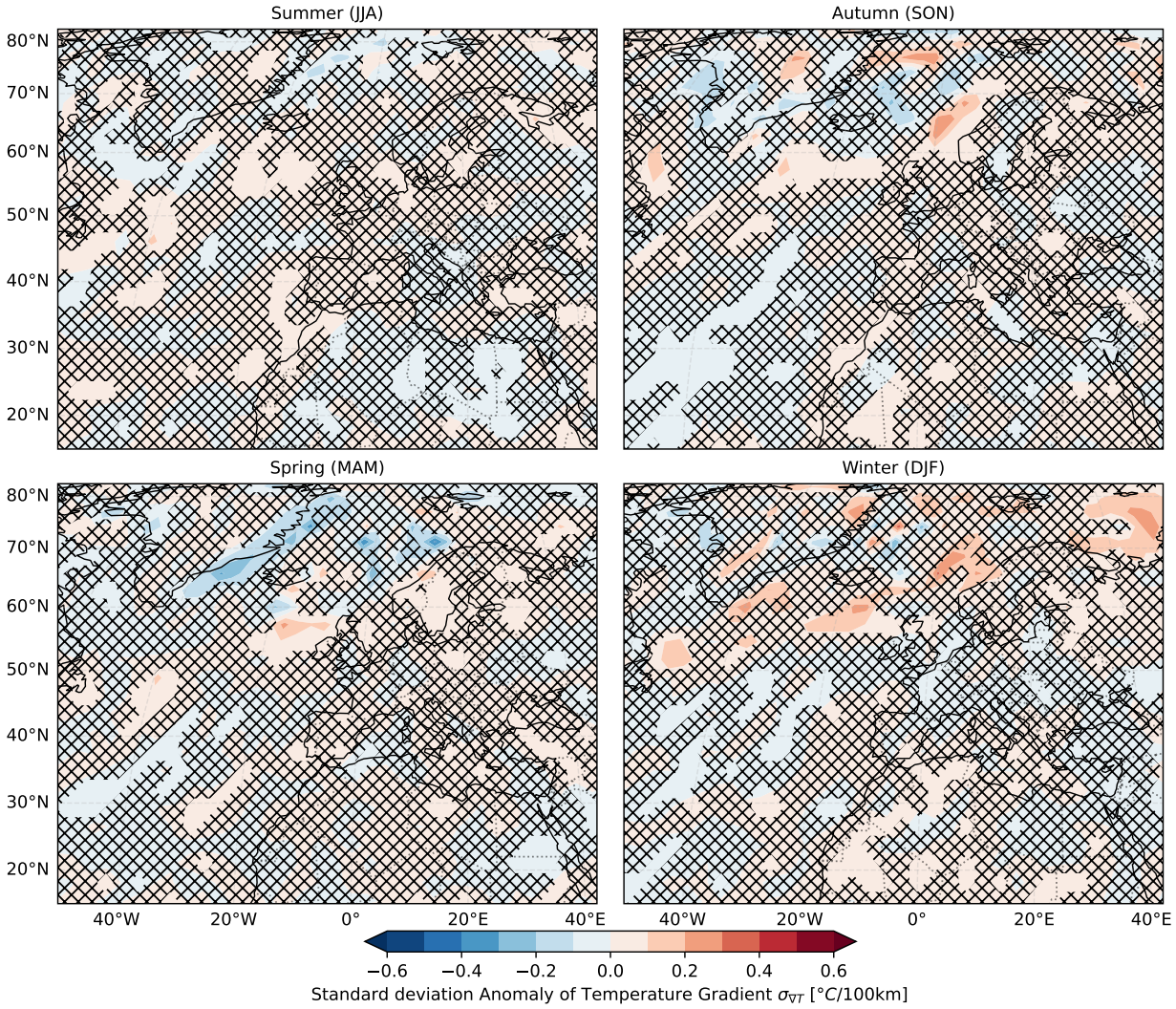


Figure 4.26: Standard deviation anomaly of the temperature gradient, in the hosing experiment, between two periods representing distinct NAO phases: years 40-66 (negative NAO) and years 67-93 (positive NAO). Anomalies are computed as negative NAO minus positive NAO period. Hatched area corresponds to nonsignificant area.

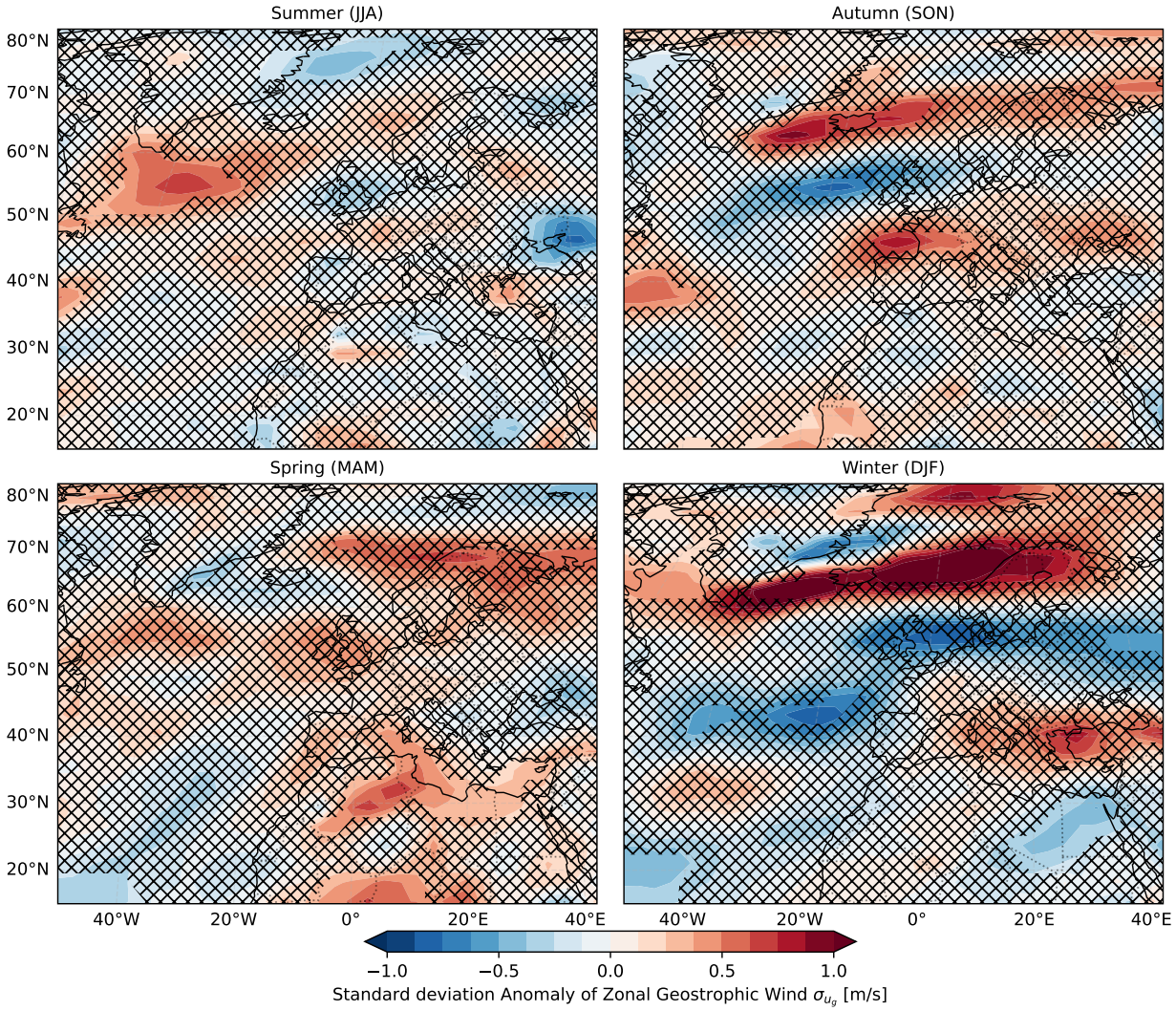


Figure 4.27: Standard deviation anomaly of the zonal geostrophic wind, in the hosing experiment, between two periods representing distinct NAO phases: years 40-66 (negative NAO) and years 67-93 (positive NAO). Anomalies are computed as negative NAO minus positive NAO period. Hatched area corresponds to nonsignificant area.

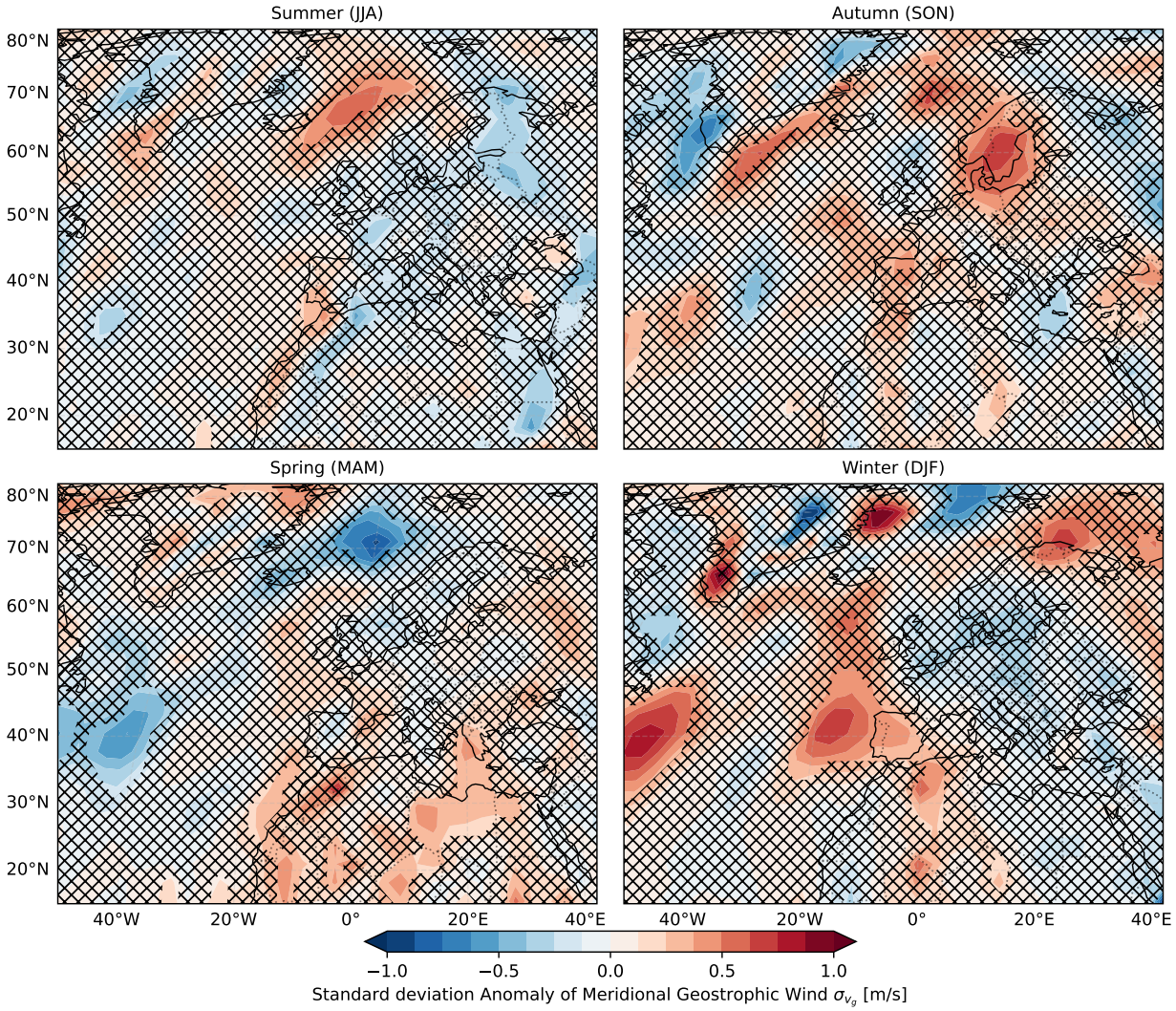


Figure 4.28: Standard deviation anomaly of the meridional geostrophic wind, in the hosing experiment, between two periods representing distinct NAO phases: years 40-66 (negative NAO) and years 67-93 (positive NAO). Anomalies are computed as negative NAO minus positive NAO period. Hatched area corresponds to nonsignificant area.

Case 2: AMOC strength dependence

Similar to case 1, the advection components are decomposed across distinct AMOC strengths between the r70 and control experiments in Figures 4.29 and 4.30 to understand the source of fluctuations revealed in Figure 4.24.

Regarding the dynamical contribution, Figure 4.29 exhibits a broad negative anomaly across the North Atlantic Ocean in winter, and less pronounced negative anomalies at higher latitudes in autumn and spring. The thermodynamic contribution exhibits a spatial pattern similar to that observed in Figure 4.24 with a southward shift in the standard deviation of the temperature gradient and a broad increase in standard deviation across Europe and the North Atlantic Ocean across all four seasons. These findings demonstrate that an AMOC weakening reduces dynamical fluctuations while enhancing thermodynamic fluctuations. This thermodynamic dominance aligns with the findings of Patrizio et al. 2026 [48], who demonstrated that colder

background conditions associated with AMOC decline shift upper-ocean density dynamics toward salinity control, strengthening local convection-salinity-sea ice feedbacks and increasing subpolar decadal temperature variance without an increase in atmospheric wind variance.

The zonal and meridional decompositions of the wind vector (Figures B.13 and B.14) show strong negative anomalies in winter located in the North Atlantic Ocean and parts of Europe, demonstrating that the increase in European temperature volatility is not caused by wind fluctuations. Instead, low-AMOC conditions stabilize the large-scale atmospheric circulation over the North Atlantic, confirming that dynamical wind volatility dampens rather than amplifies temperature volatility over a centennial time scale. This decoupling from atmospheric wind noise is further supported by Patrizio et al. 2026 [48] and Gu et al. 2024 [50], who showed that surface heat fluxes play a damping role, confirming that temperature variance is sustained by oceanic forcing rather than enhanced atmospheric forcing. This wind stabilization occurs because the intense subpolar cooling sharpens the MTG (Figure B.4). Through thermal wind balance, this enhanced baroclinic zone produces a southward-shifted, stronger, and more persistent westerly jet, as shown in Figure B.15. The zonal and meridional temperature gradient decompositions (Figures 4.31 and 4.32) both show spatial patterns consistent with Figure 4.30. Their zonal and meridional anomaly amplitudes are comparable during winter, meaning that both directions contribute equally to the thermodynamic fluctuations during that season. However, autumn and spring display a slight zonal dominance over the meridional direction, suggesting that these transition seasons are mainly driven by zonal temperature gradient fluctuations.

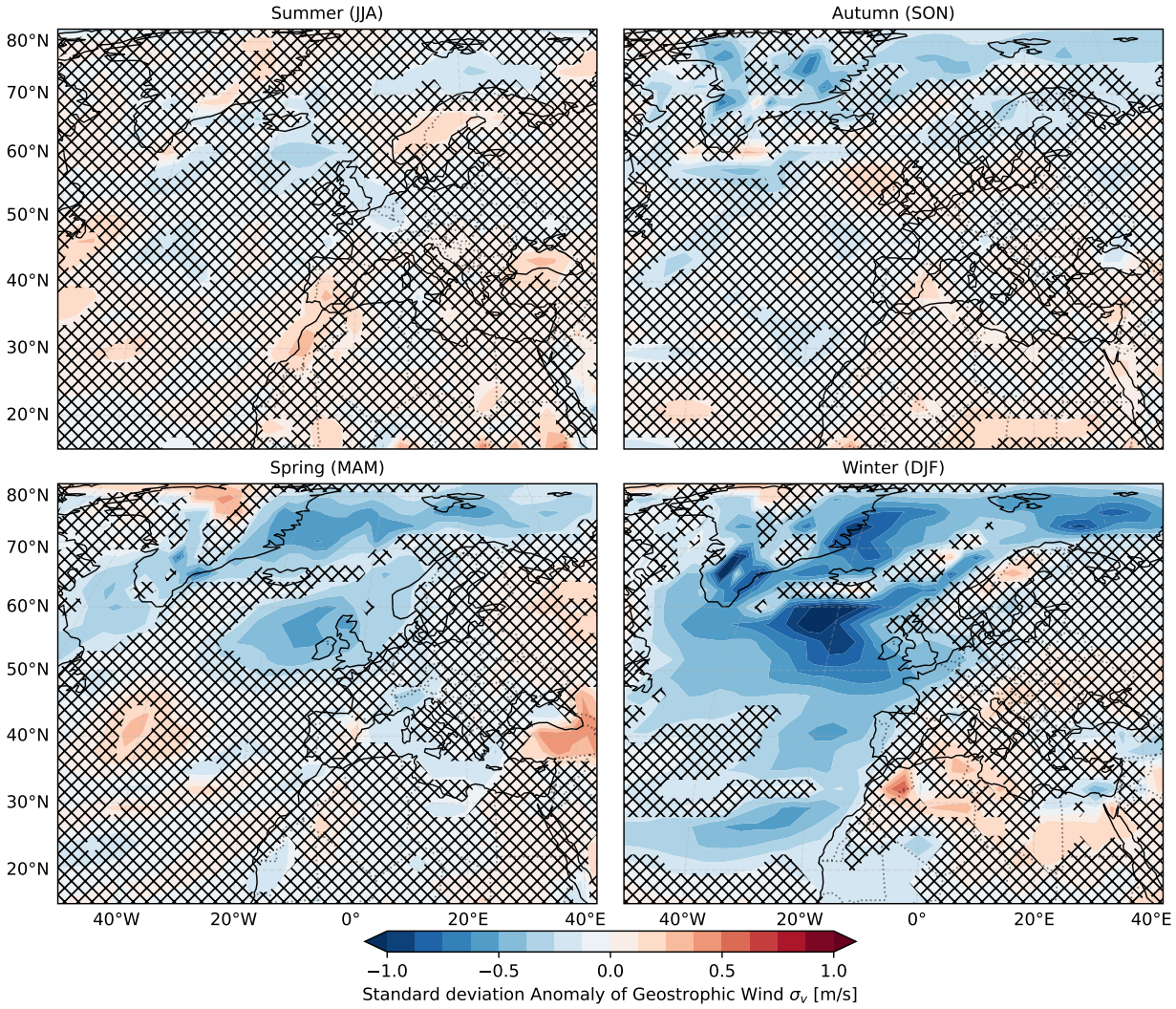


Figure 4.29: Standard deviation anomaly of the geostrophic wind between two periods representing distinct AMOC strength: years 150-250 (r70, low AMOC strength) and years 0-164 (control, high AMOC strength). Anomalies are computed as r70 minus control. Hatched area corresponds to nonsignificant area.

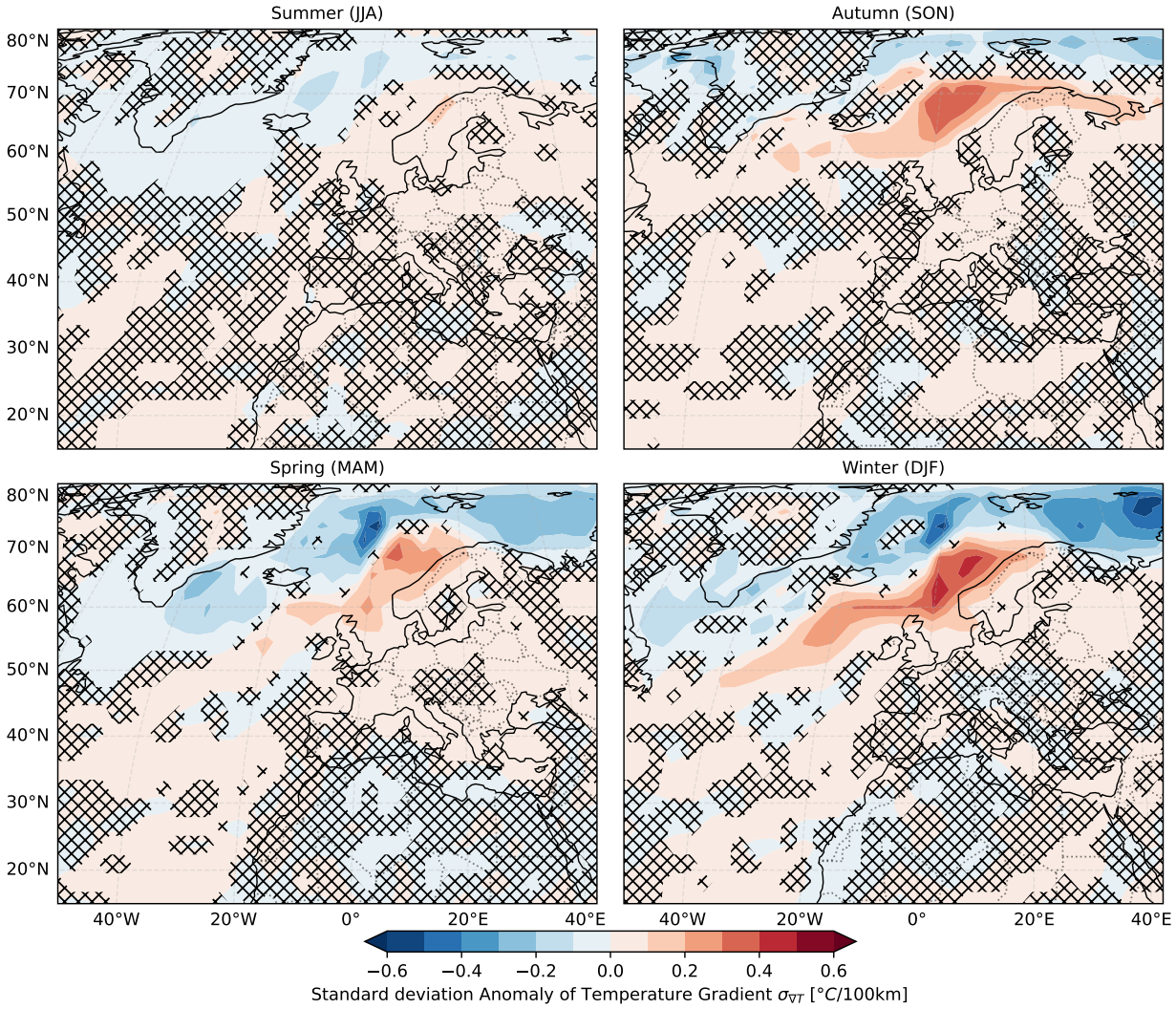


Figure 4.30: Standard deviation anomaly of the temperature gradient between two periods representing distinct AMOC strength: years 150-250 (r70, low AMOC strength) and years 0-164 (control, high AMOC strength). Anomalies are computed as r70 minus control. Hatched area corresponds to nonsignificant area.

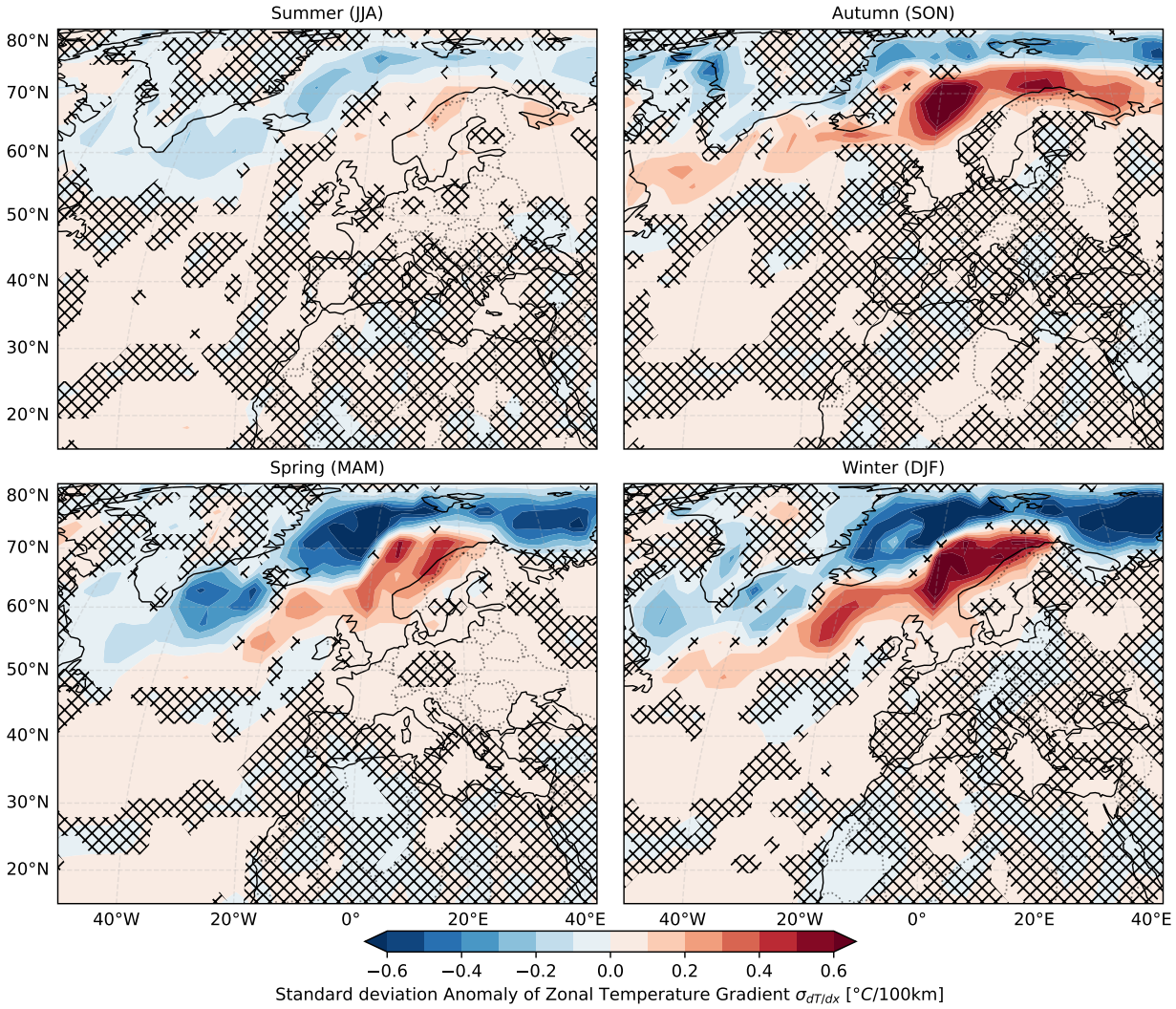


Figure 4.31: Standard deviation anomaly of the zonal temperature gradient between two periods representing distinct AMOC strength: years 150-250 (r70, low AMOC strength) and years 0-164 (control, high AMOC strength). Anomalies are computed as r70 minus control. Hatched area corresponds to nonsignificant area.

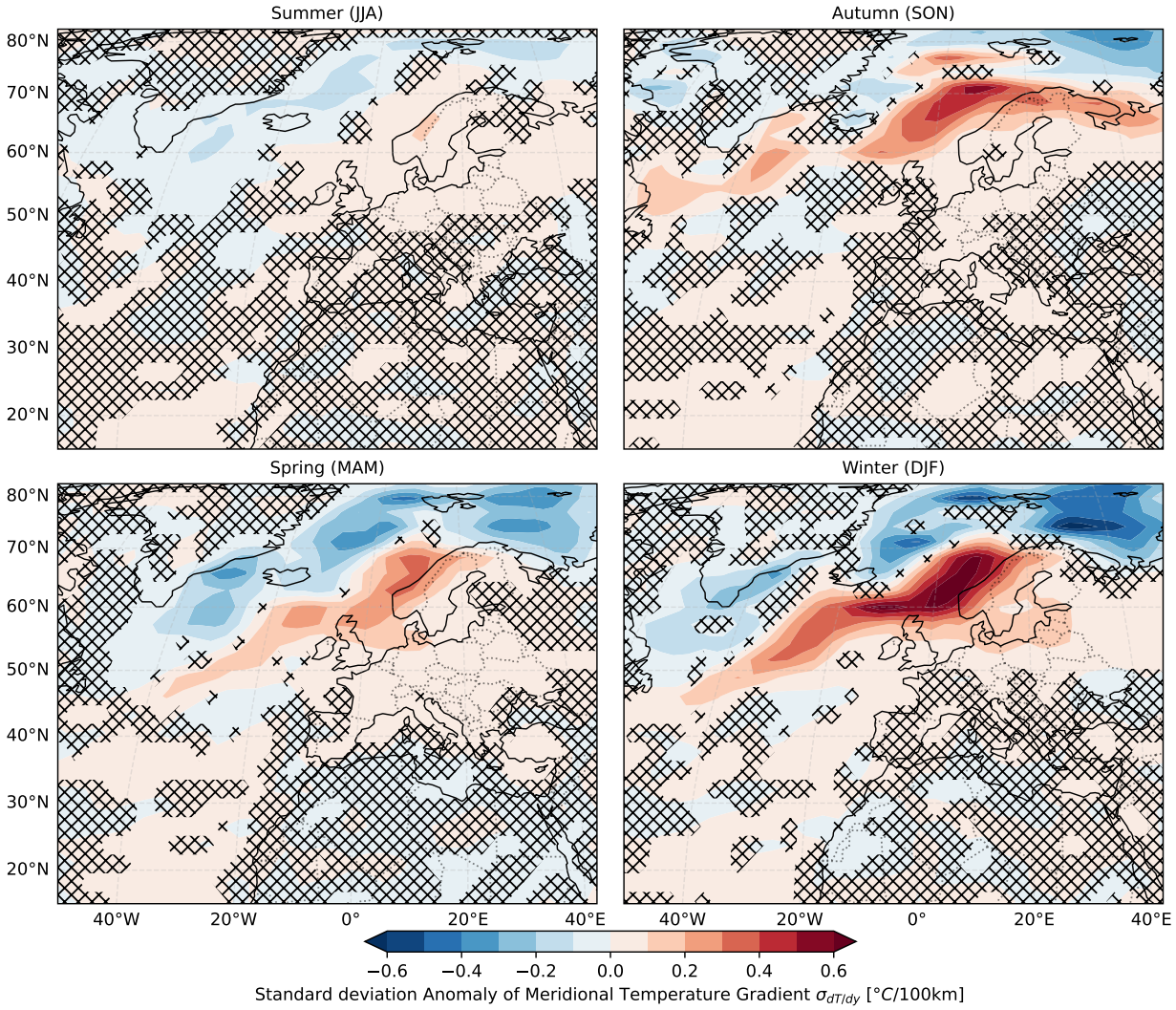


Figure 4.32: Standard deviation anomaly of the meridional temperature gradient between two periods representing distinct AMOC strength: years 150-250 (r70, low AMOC strength) and years 0-164 (control, high AMOC strength). Anomalies are computed as r70 minus control. Hatched area corresponds to nonsignificant area.

4.4 Schematic summary

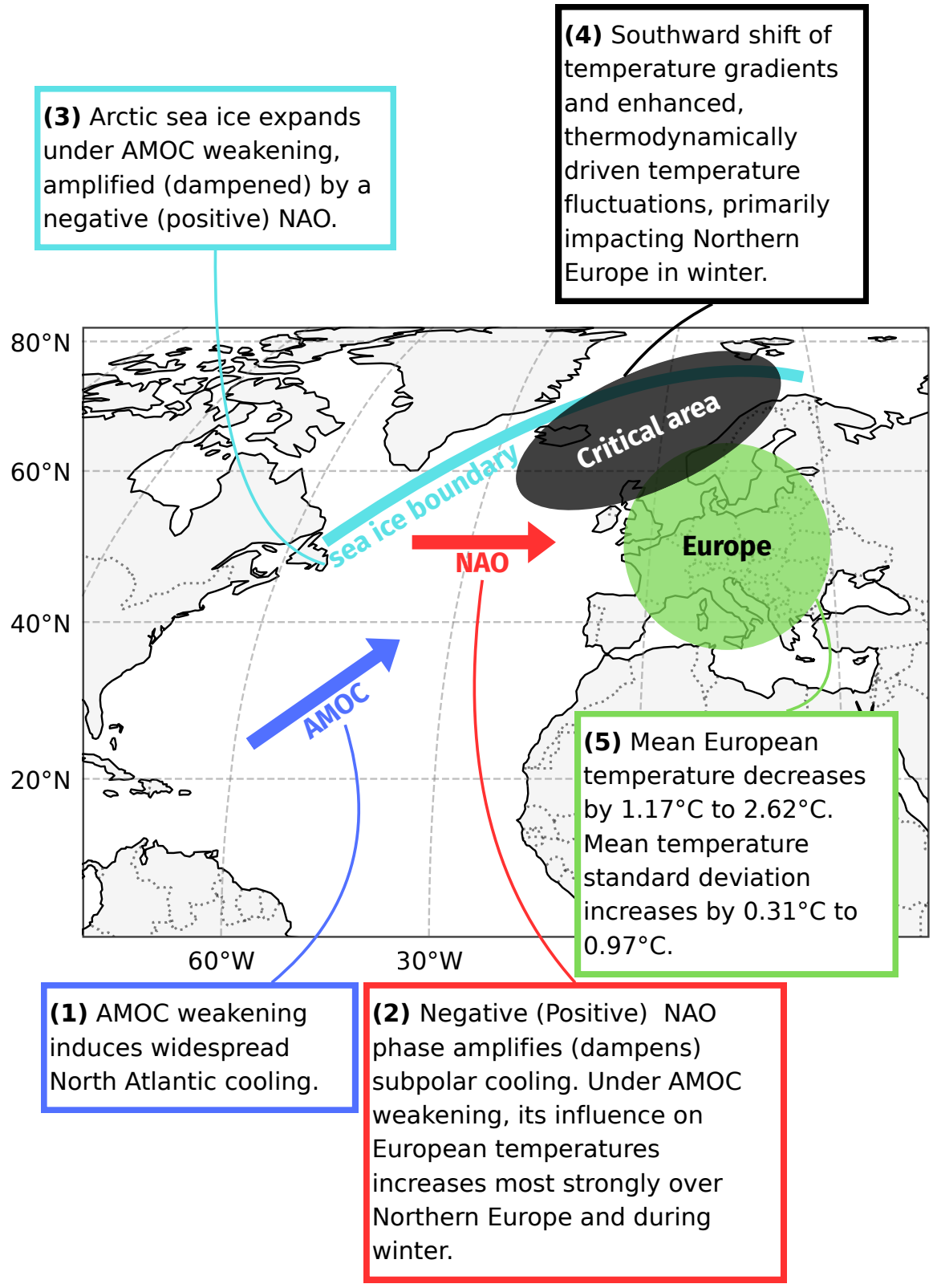


Figure 4.33: Schematic summary of the physical mechanism.

Chapter 5

Conclusions

The objective of this thesis is to evaluate the European climate response induced by an AMOC weakening. This study addresses two research questions: How does the influence of the NAO on European temperatures vary with AMOC strength on decadal timescales ? What physical mechanisms govern changes in European temperature standard deviation under a weakened AMOC state ? For this purpose, data from the CanESM5 model within the NAHosMIP framework were analyzed. The forcing applied to pre-industrial initial conditions consists of an additional freshwater flux into the North Atlantic (uniform hosing). In total, four experiments were examined, a control run, a hosing phase and two recovery phases (after 50 and 70 years of hosing). The four analyzed variables are the maximum AMOC streamfunction at 26.5°N, surface air temperature, precipitation and air pressure at sea-level.

The results show that an AMOC weakening induces a widespread cooling across Europe, ranging from -1.17°C to -2.62°C on average compared to the control run. Seasonal and regional covariance analyses show that European temperature is primarily driven by the winter season and the Northern European region under a low-AMOC state. A more pronounced cooling occurs in the North Atlantic, specifically within the Nordic Seas. Consequently, Arctic sea ice expands, shifting thermal fronts southward, which further amplifies the cooling effect during winter and across Northern Europe.

This study examines the coupling between the AMOC and the NAO. Under a low-AMOC state, a negative NAO phase amplifies the sea ice expansion and enhances the cooling effect by displacing the high-latitude temperature gradient closer to Northern Europe. Conversely, a positive NAO phase dampens the cooling effect. Regarding the perturbed experiments (hosing, r50, and r70), a linear temperature model of the AMOC and NAO signals fits the European temperatures with a mean coefficient of determination (r^2) of 0.69, roughly 1.7× higher than the fit without the NAO contribution, demonstrating that the NAO is a key driver of European temperatures under low-AMOC state. Seasonal and regional analyses of the fit reveal that the NAO contribution is largest during winter and over Northern Europe. Furthermore, it is precisely in this region and season that the NAO's influence increases the most under AMOC weakening.

The findings demonstrate an increased mean temperature standard deviation of Europe, ranging from +0.31°C to +0.97°C on average compared to the control run. The seasonal and spatial analyses of the European temperature standard deviation reveal that AMOC weakening not only cools Europe but also increases temperature volatility during the same seasons and in the

same regions where the cooling effect is the most pronounced. Spatial analysis shows that contrasting NAO phases generate temperature volatility in the Nordic Seas during winter, while variations in AMOC strength produce a stronger and more widespread volatility from autumn to spring. The advection analysis provides the physical mechanism for both cases. The NAO phase dependence is driven by zonal geostrophic fluctuation in the Nordic Seas during winter, while the AMOC strength dependence is driven by zonal and meridional temperature gradients in a similar region during the autumn-to-spring period.

While this thesis provides valuable insights into the European climate response to an AMOC weakening, several limitations outline clear pathways for future research. First, the analysis of baroclinic instabilities is restricted to a single vertical atmospheric level, which may not fully capture the complex vertical structure of storm tracks. Future studies should incorporate multi-level vertical profiles to better resolve these dynamics. Additionally, while sea ice expansion was identified as a critical mechanism in this study using the surface air temperature (*tas*), an investigation incorporating sea ice concentration directly would provide a more complete understanding of sea ice dynamics. Furthermore, employing a higher temporal resolution would improve the characterization of atmospheric circulation by resolving shorter-timescale features such as atmospheric blocking events and easterly intrusions. In addition, developing a more sophisticated temperature model that accounts for nonlinear terms, time lags between oceanic forcing and atmospheric responses, and other external climate drivers would refine our understanding of the AMOC-induced European temperature response. Finally, because this study relies exclusively on the CanESM5 model, the robustness of these findings should be validated through multi-model comparison studies (such as with IPSL-CM6A-LR, CESM2, and HadGEM3-GC3-1MM) to account for model-specific biases.

Appendix A

Nomenclature

AMOC	Atlantic Meridional Overturning Circulation
APE	Available Potential Energy
CanESM5	Canadian Earth System Model version 5
CCSM4	Community Climate System Model version 4
CESM1	Community Earth System Model version 1
CMIP6	Coupled Model Intercomparison Project Phase 6
ECMWF	European Centre for Medium-Range Weather Forecasts
ECS	Equilibrium Climate Sensitivity
EOF	Empirical Orthogonal Function
MOC	Meridional Overturning Circulation
MTG	Meridional Temperature Gradient
NADW	North Atlantic Deep Water
NAHosMIP	North Atlantic Hosing Model Intercomparison Project
NAO	North Atlantic Oscillation
OHT	Oceanic Heat Transport
pr	Precipitation flux
psl	Air pressure at sea level
SSS	Sea Surface Salinity
SST	Sea Surface Temperature
tas	Surface Air Temperature

Appendix B

Additional graphs

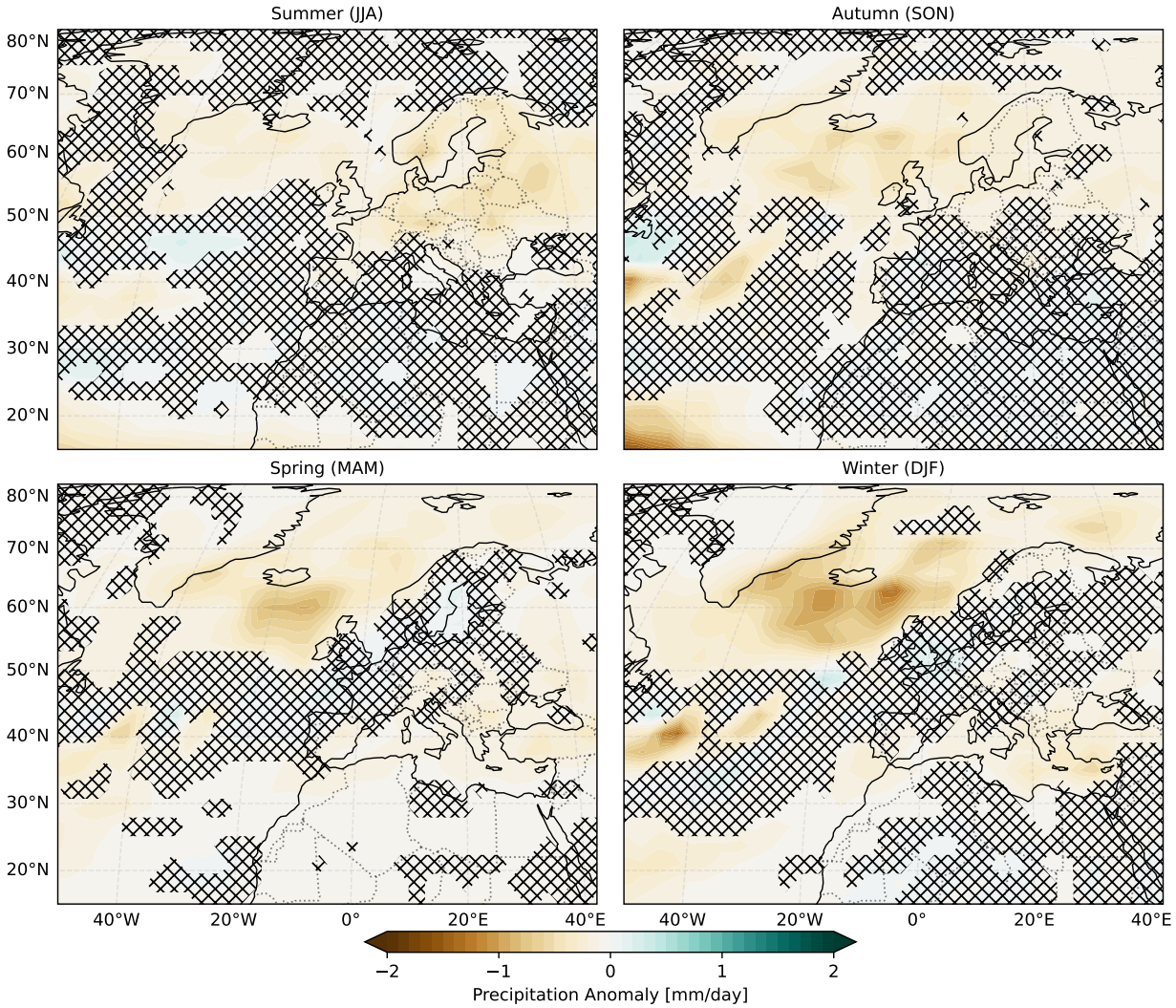


Figure B.1: Seasonal precipitation anomaly between r50 and the control experiment from year 50 to 150 (r50 minus control). Hatched area corresponds to nonsignificant area.

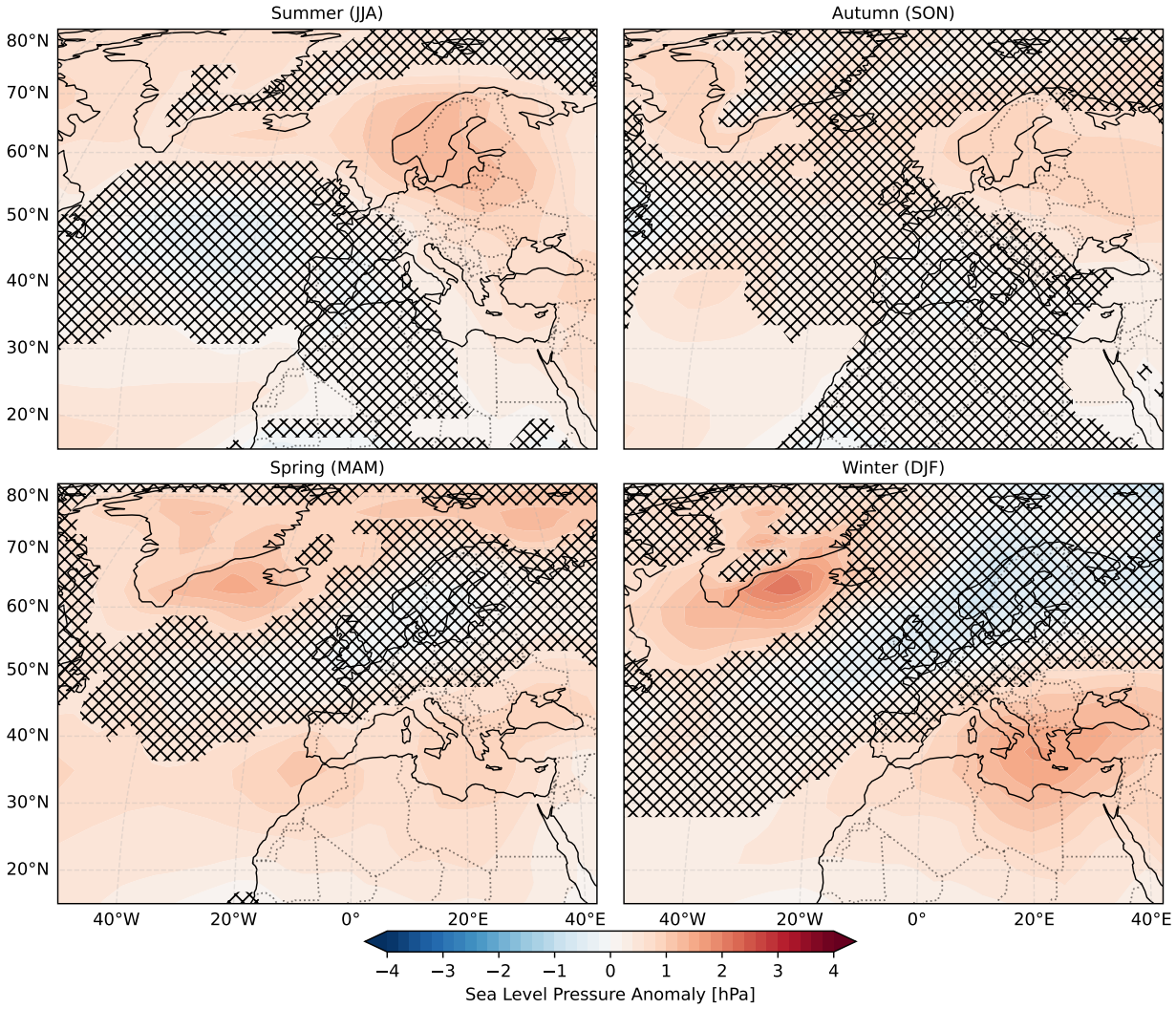


Figure B.2: Seasonal sea-level pressure anomaly between r50 and control experiment from year 50 to 150 (r50 minus control). Hatched area corresponds to nonsignificant area.

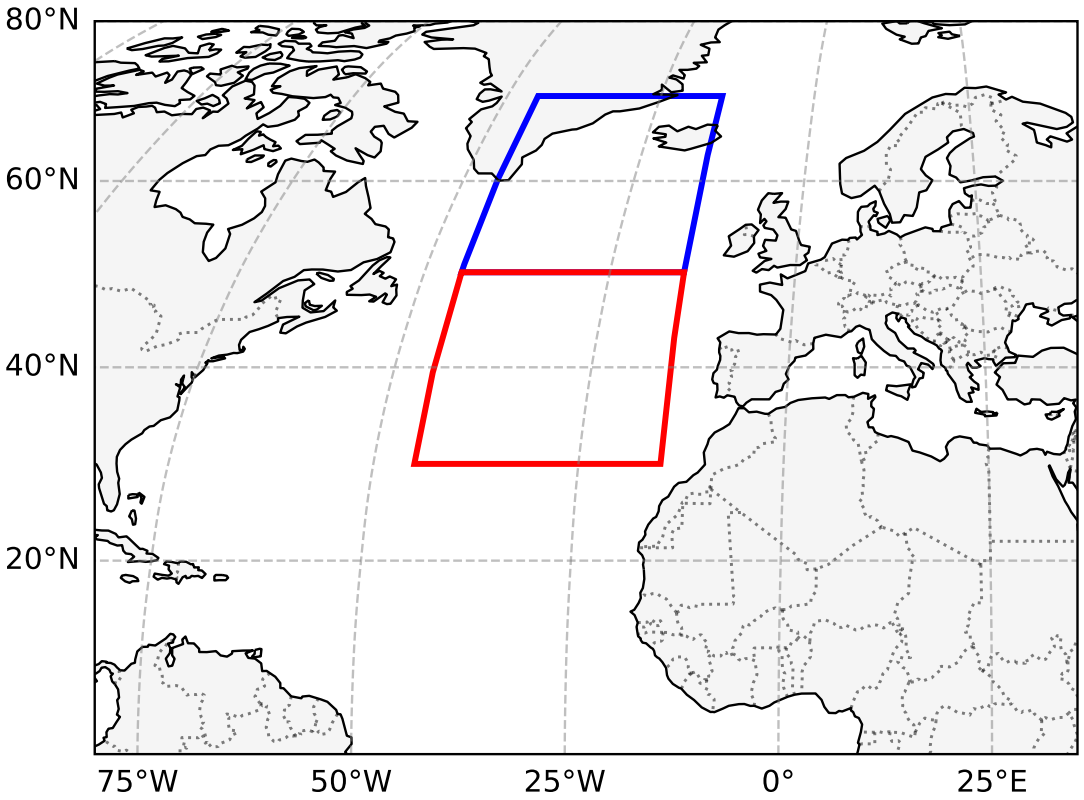


Figure B.3: Meridional Temperature Gradient (MTG) boxes, the gradient is defined as the difference between the red box and blue box.

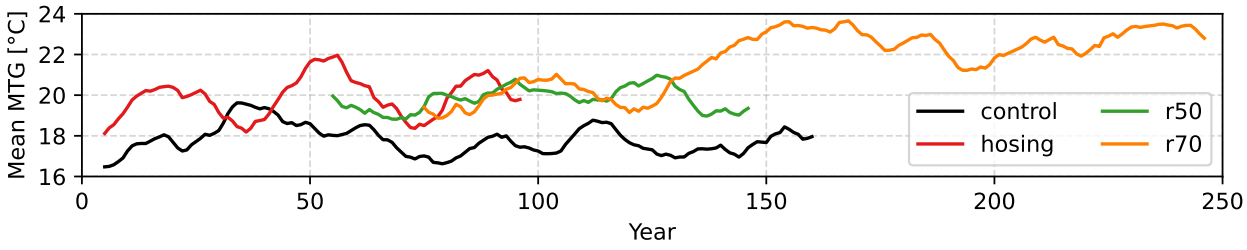


Figure B.4: Decadal running mean of the Meridional Temperature Gradient (MTG).

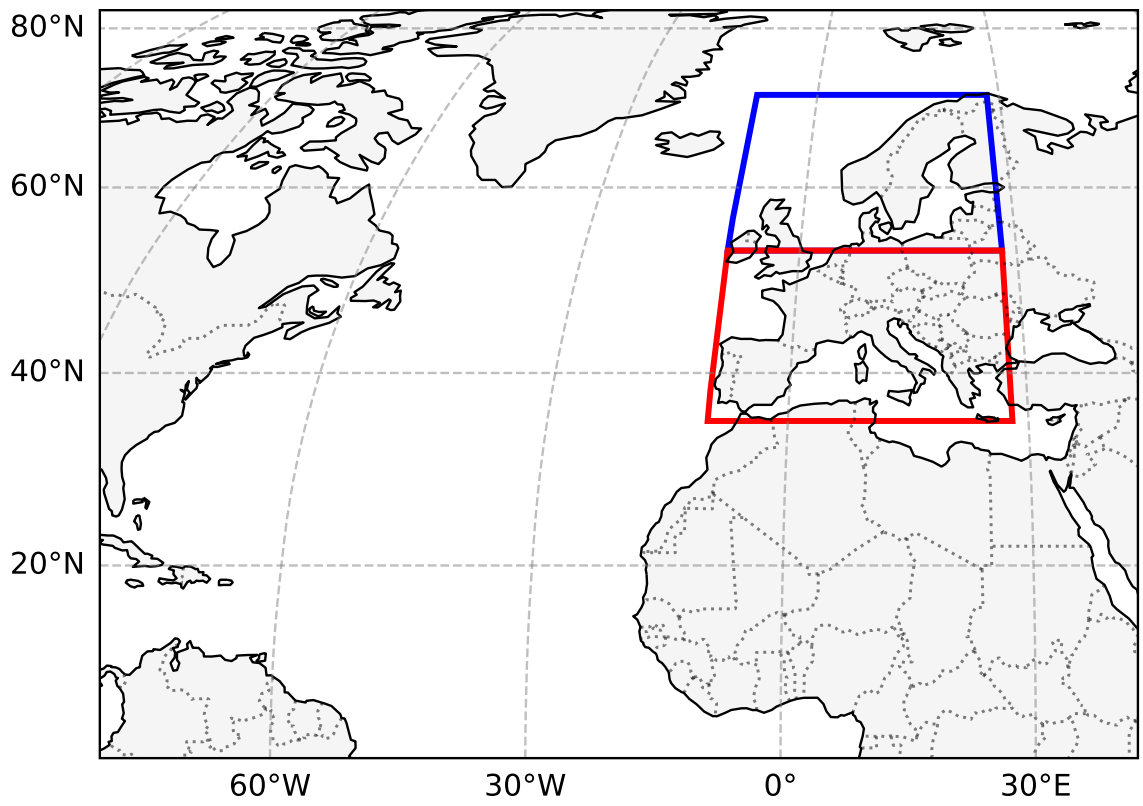


Figure B.5: Meridional Temperature Gradient (MTG) boxes in Europe, the gradient is defined as the difference between the red box (South box) and blue box (North box).

	Weighted covariance decomposition [%]	
10-year mean	South box	North box
control	2.14	97.86
hosing	−45.86	145.86
r50	−7.58	107.58
r70	−21.38	121.38

Table B.1: Percentage of the European MTG variance explained by the North and South boxes across control, hosing, and recovery scenarios.

	Mean standard deviation [°C]			
Southern Europe	Summer (JJA)	Autumn (SON)	Winter (DJF)	Spring (MAM)
control	0.63	0.55	0.73	0.68
hosing	0.71	0.73	0.81	0.82
r50	0.53	0.53	0.71	0.71
r70	0.65	0.64	0.76	0.80
Western Europe	Summer (JJA)	Autumn (SON)	Winter (DJF)	Spring (MAM)
control	0.82	0.85	1.19	0.95
hosing	0.91	1.05	1.26	1.20
r50	0.96	0.90	1.14	1.13
r70	0.89	1.01	1.31	1.21
Eastern Europe	Summer (JJA)	Autumn (SON)	Winter (DJF)	Spring (MAM)
control	0.64	0.96	1.83	1.19
hosing	0.79	1.18	1.71	1.44
r50	0.77	0.95	1.42	1.23
r70	0.79	1.09	1.65	1.27
Northern Europe	Summer (JJA)	Autumn (SON)	Winter (DJF)	Spring (MAM)
control	0.63	0.83	1.55	1.00
hosing	0.83	1.04	2.12	1.48
r50	0.70	0.84	1.44	0.98
r70	0.79	0.97	2.11	1.42

Table B.2: 30-years running mean standard deviation of European temperature originating from each region and each season across control, hosing, and recovery scenarios.

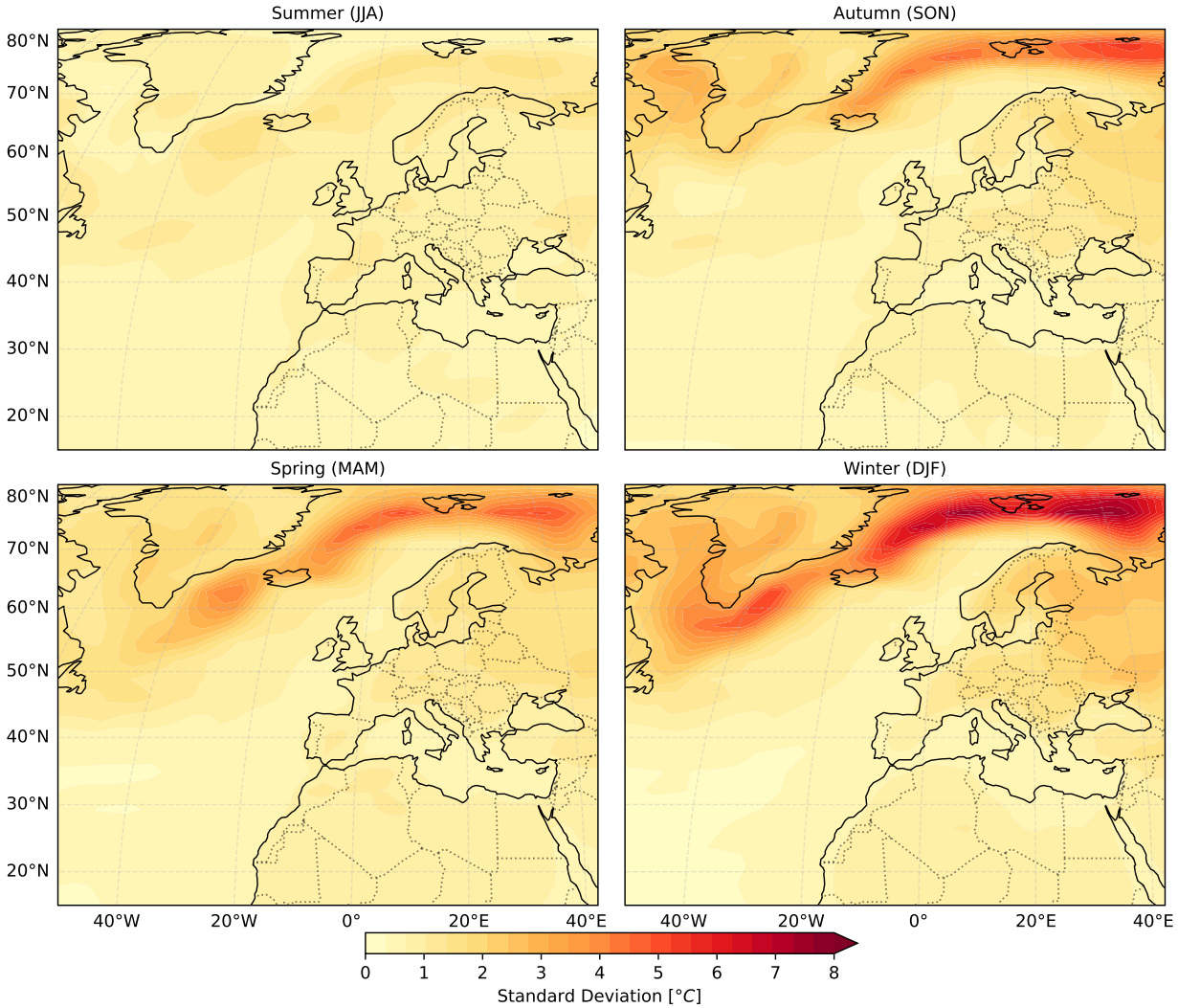


Figure B.6: Linearly detrended Standard Deviation of the control run from year 0 to 164.

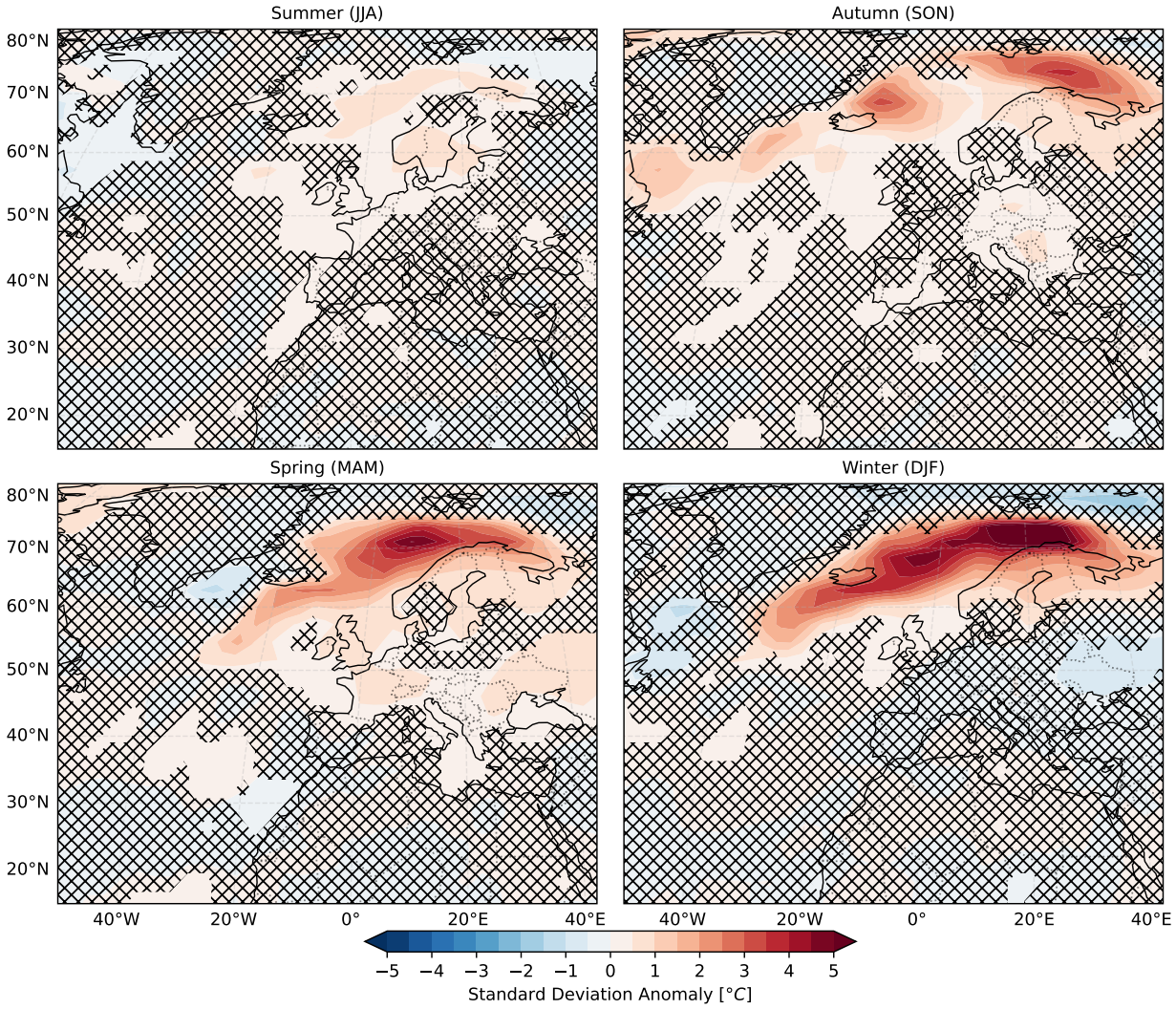


Figure B.7: Seasonal standard deviation temperature anomaly of the negative NAO phase (year 40-70), between two experiments representing distinct AMOC strength: hosing (low AMOC strength) and control (high AMOC strength). Anomalies are computed as hosing minus control. Hatched area corresponds to nonsignificant area.

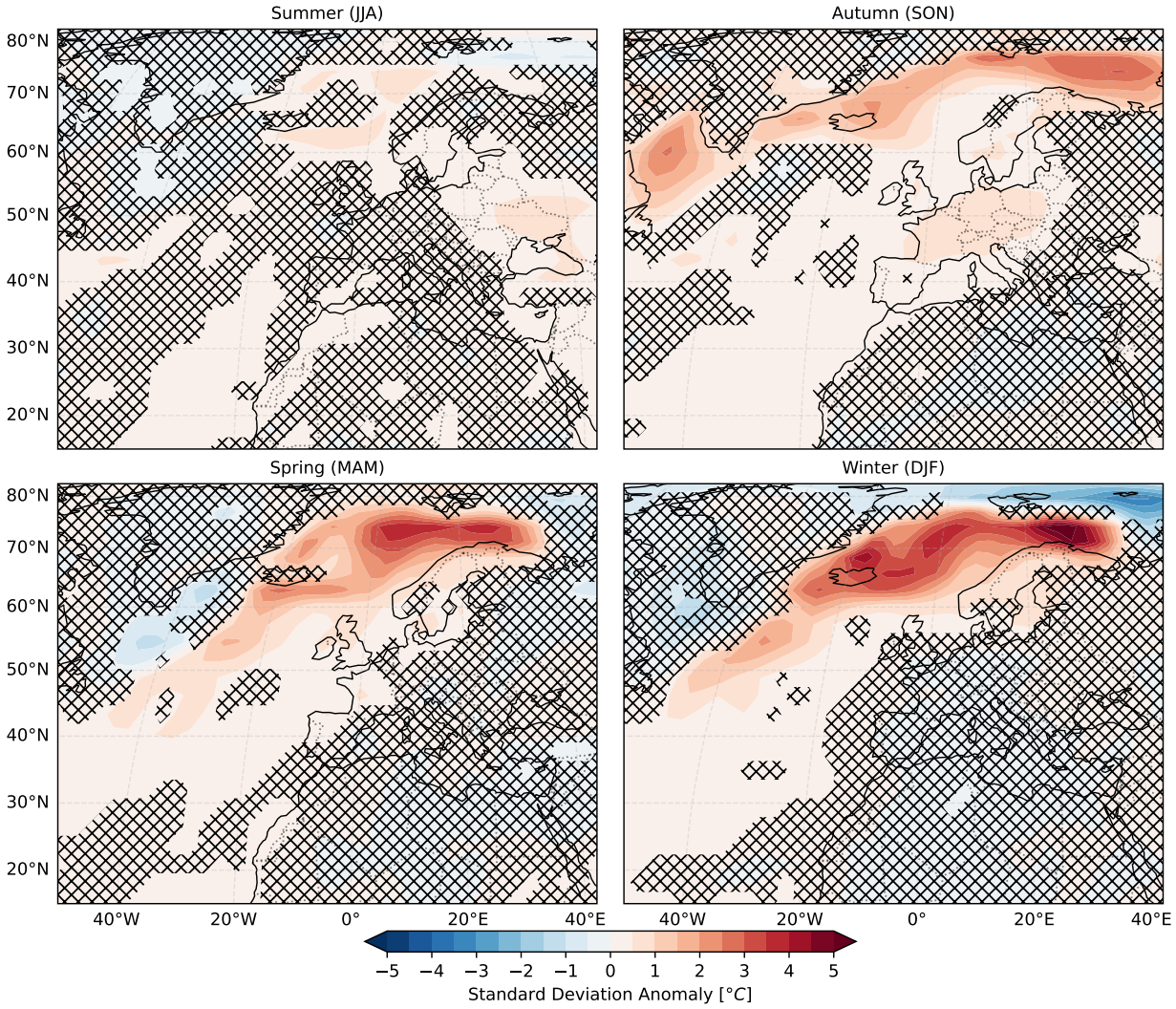


Figure B.8: Seasonal standard deviation temperature anomaly of the positive NAO phase (year 63-93), between two experiments representing distinct AMOC strength: hosing (low AMOC strength) and control (high AMOC strength). Anomalies are computed as hosing minus control. Hatched area corresponds to nonsignificant area.

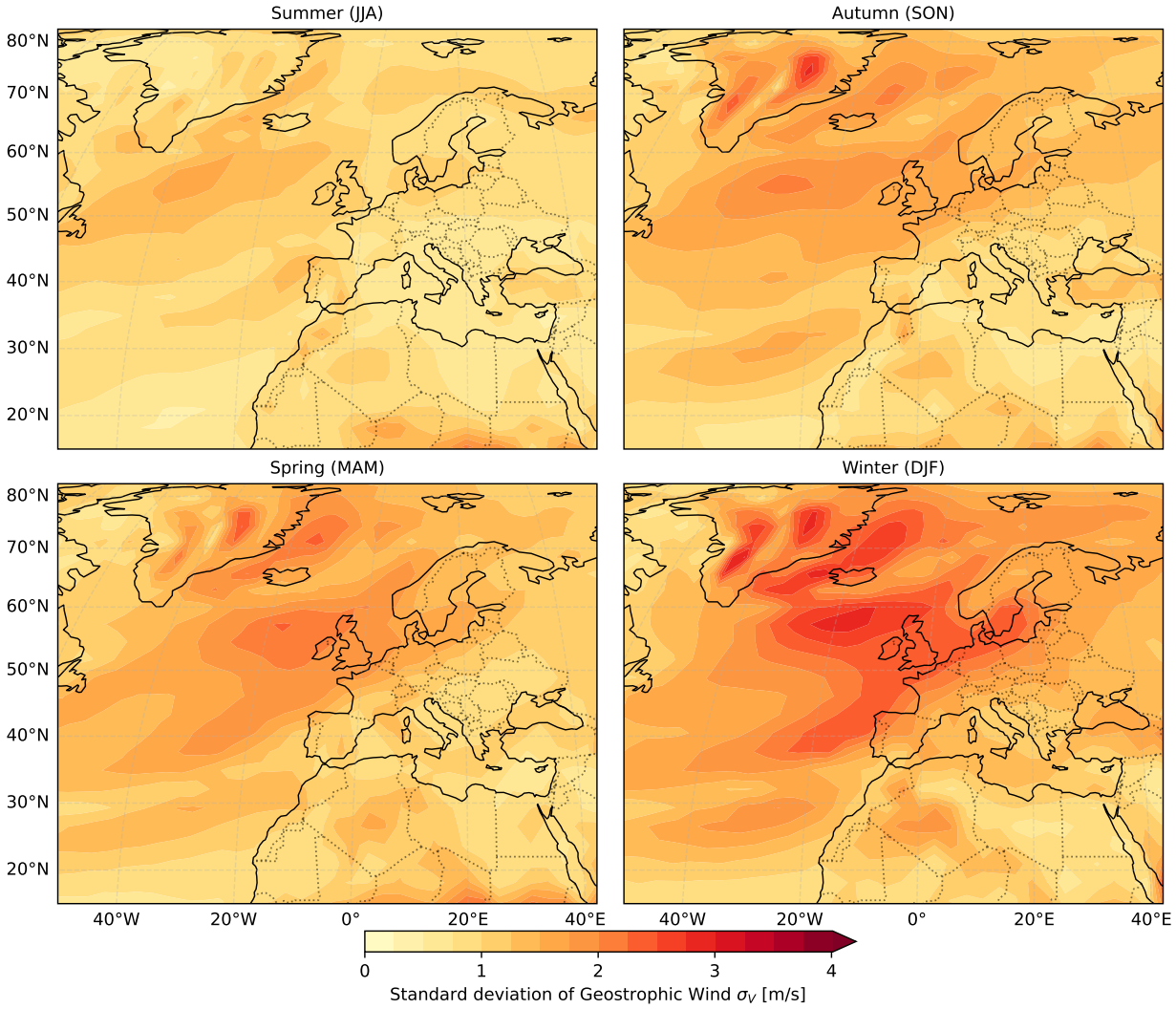


Figure B.9: Linearly detrended standard deviation of the geostrophic wind in the control run from year 0 to 164.

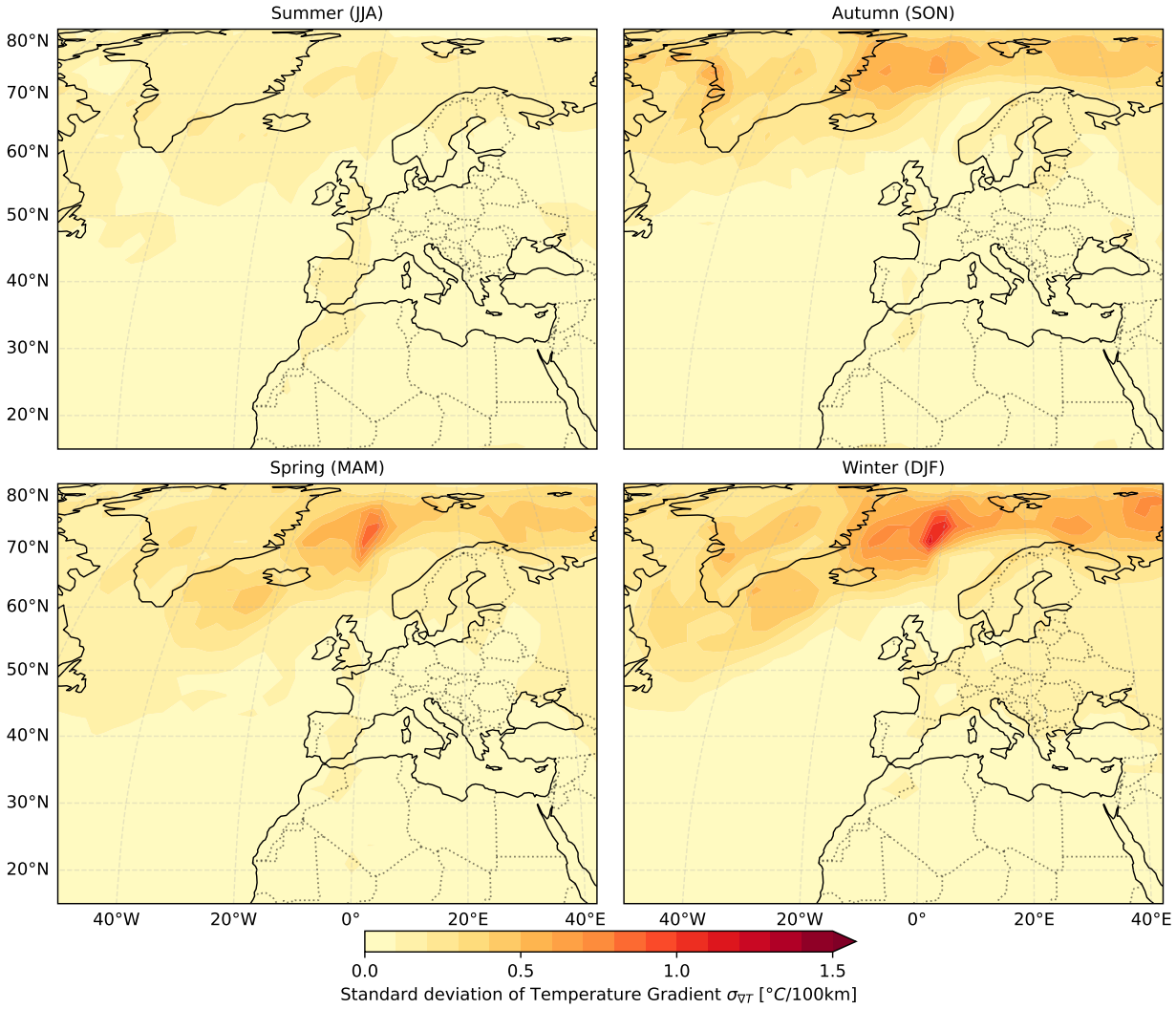


Figure B.10: Linearly detrended standard deviation of the temperature gradient in the control run from year 0 to 164.

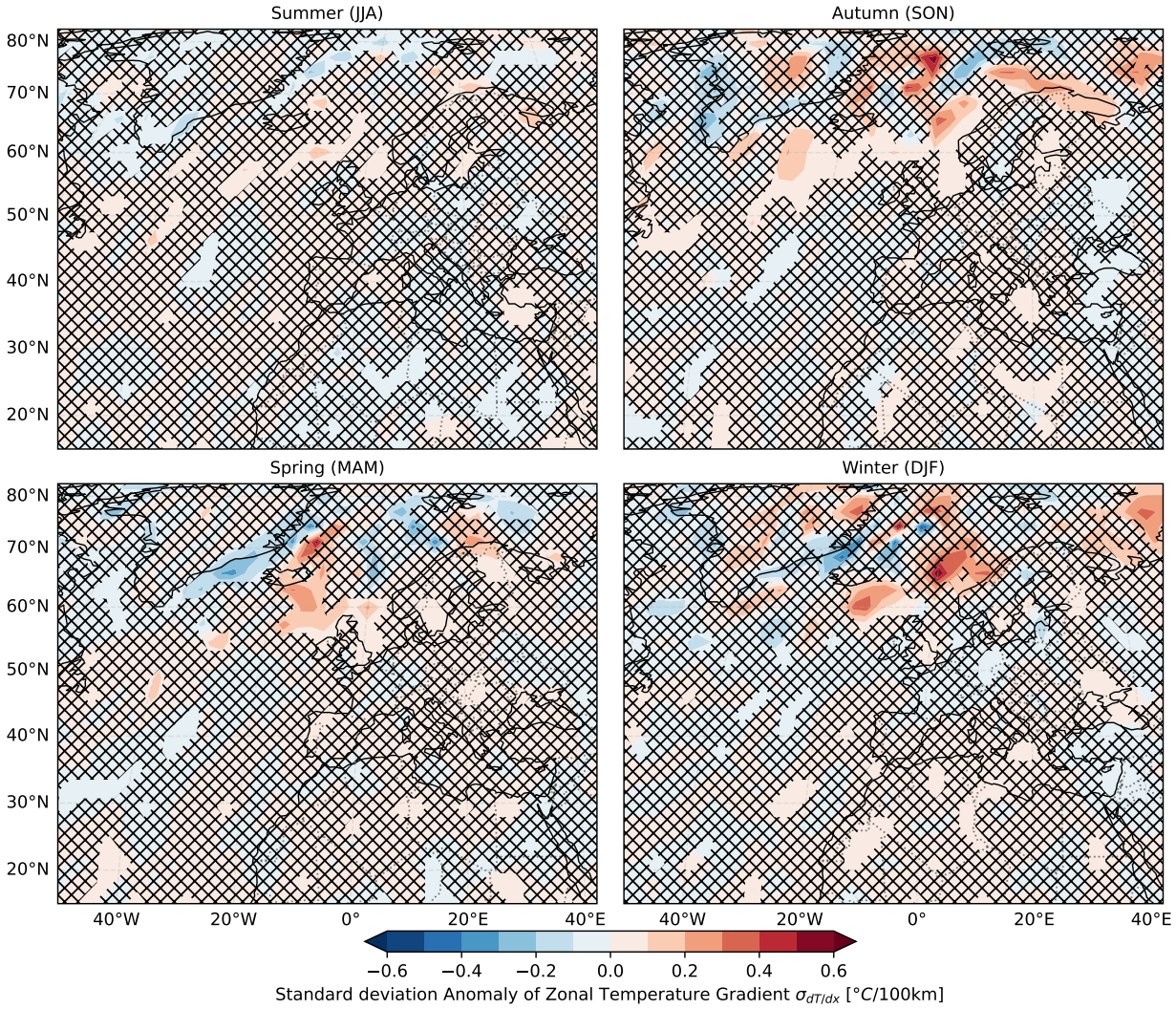


Figure B.11: Standard deviation anomaly of the zonal temperature gradient, in the hosing experiment, between two periods representing distinct NAO phases: years 40-66 (negative NAO) and years 67-93 (positive NAO). Anomalies are computed as negative NAO minus positive NAO period. Hatched area corresponds to nonsignificant area.

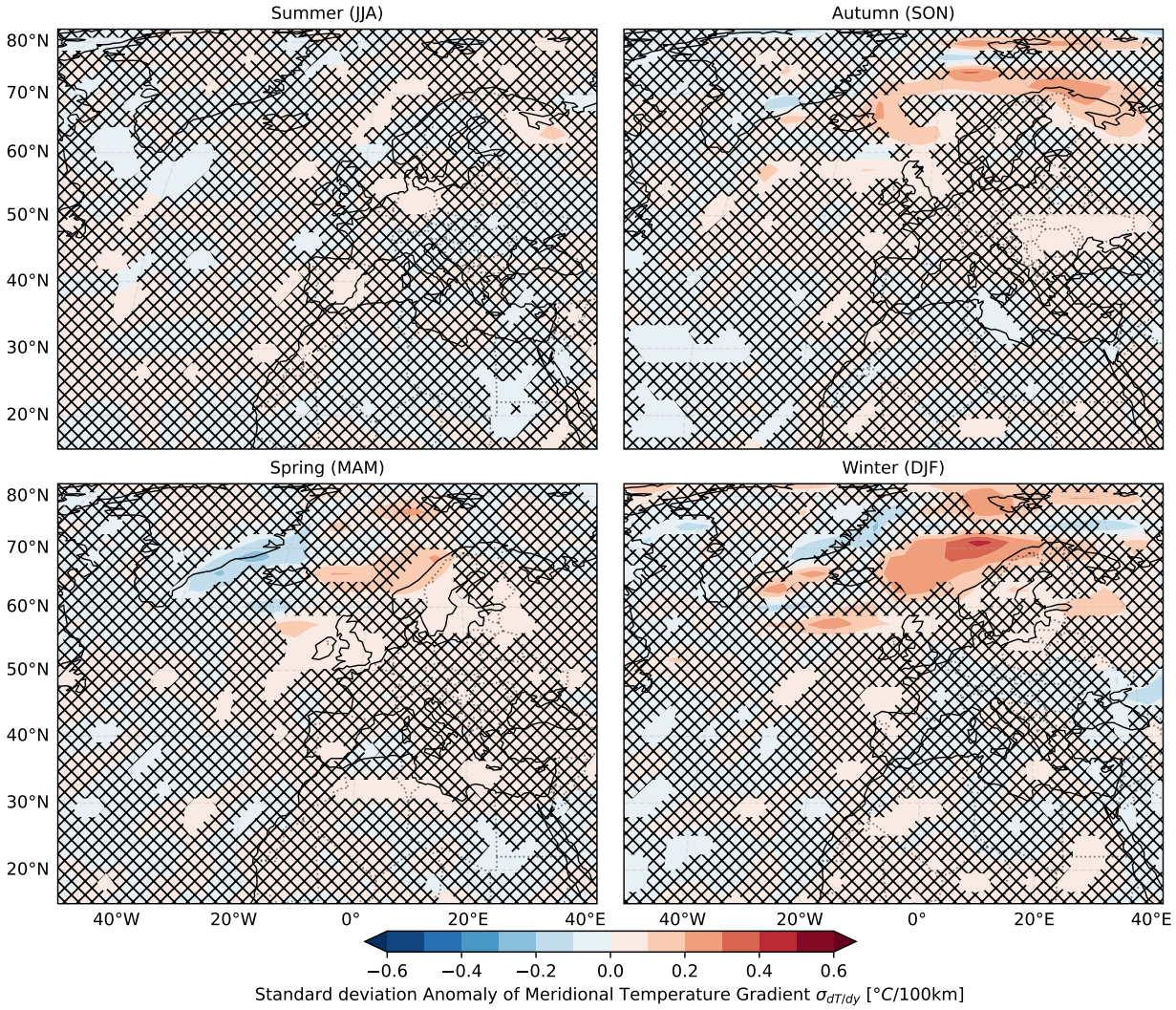


Figure B.12: Standard deviation anomaly of the meridional temperature gradient, in the hosing experiment, between two periods representing distinct NAO phases: years 40-66 (negative NAO) and years 67-93 (positive NAO). Anomalies are computed as negative NAO minus positive NAO period. Hatched area corresponds to nonsignificant area.

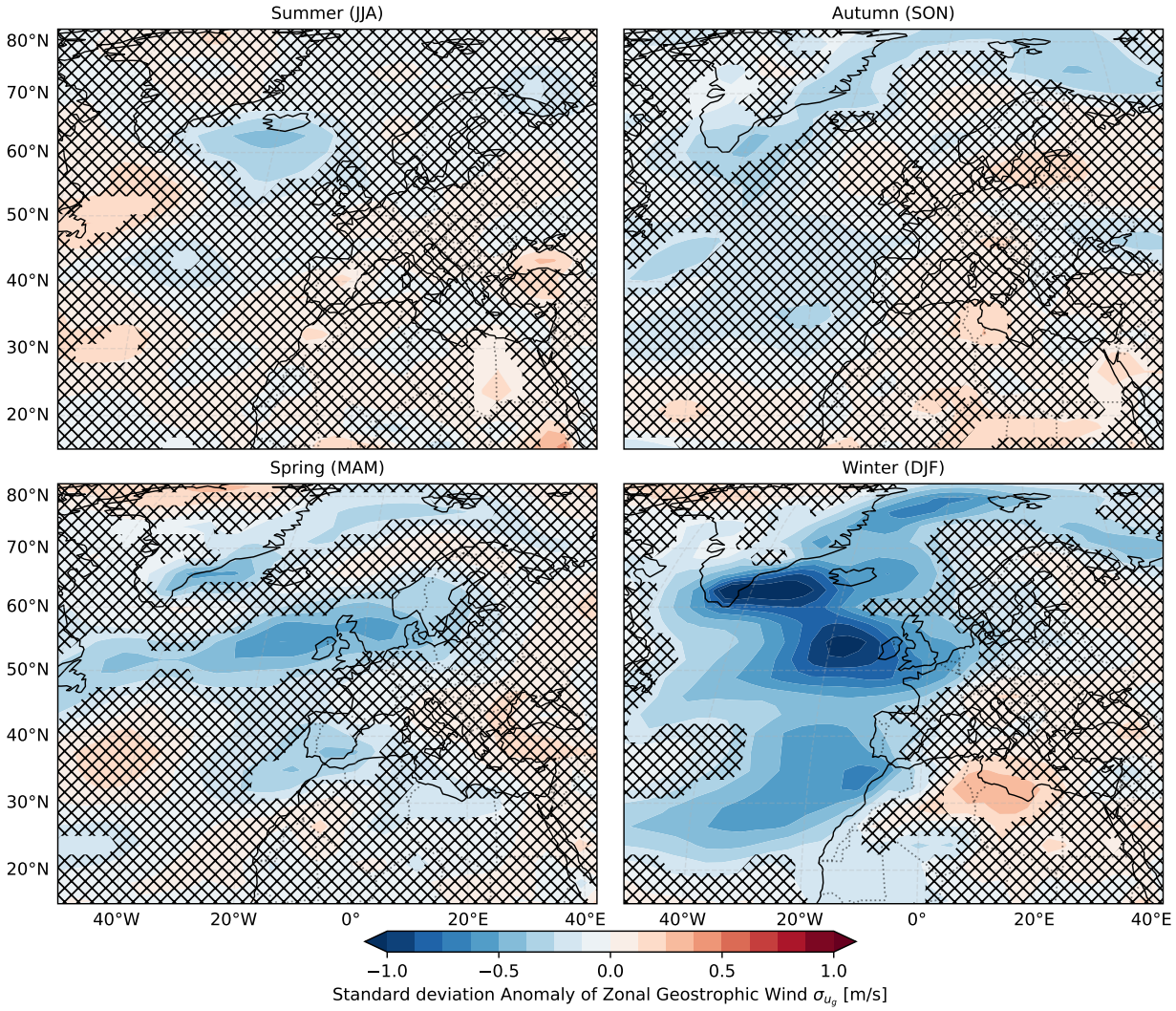


Figure B.13: Standard deviation anomaly of the zonal geostrophic wind between two periods representing distinct AMOC strength: years 150-250 (r70, low AMOC strength) and years 0-164 (control, high AMOC strength). Anomalies are computed as r70 minus control. Hatched area corresponds to nonsignificant area.

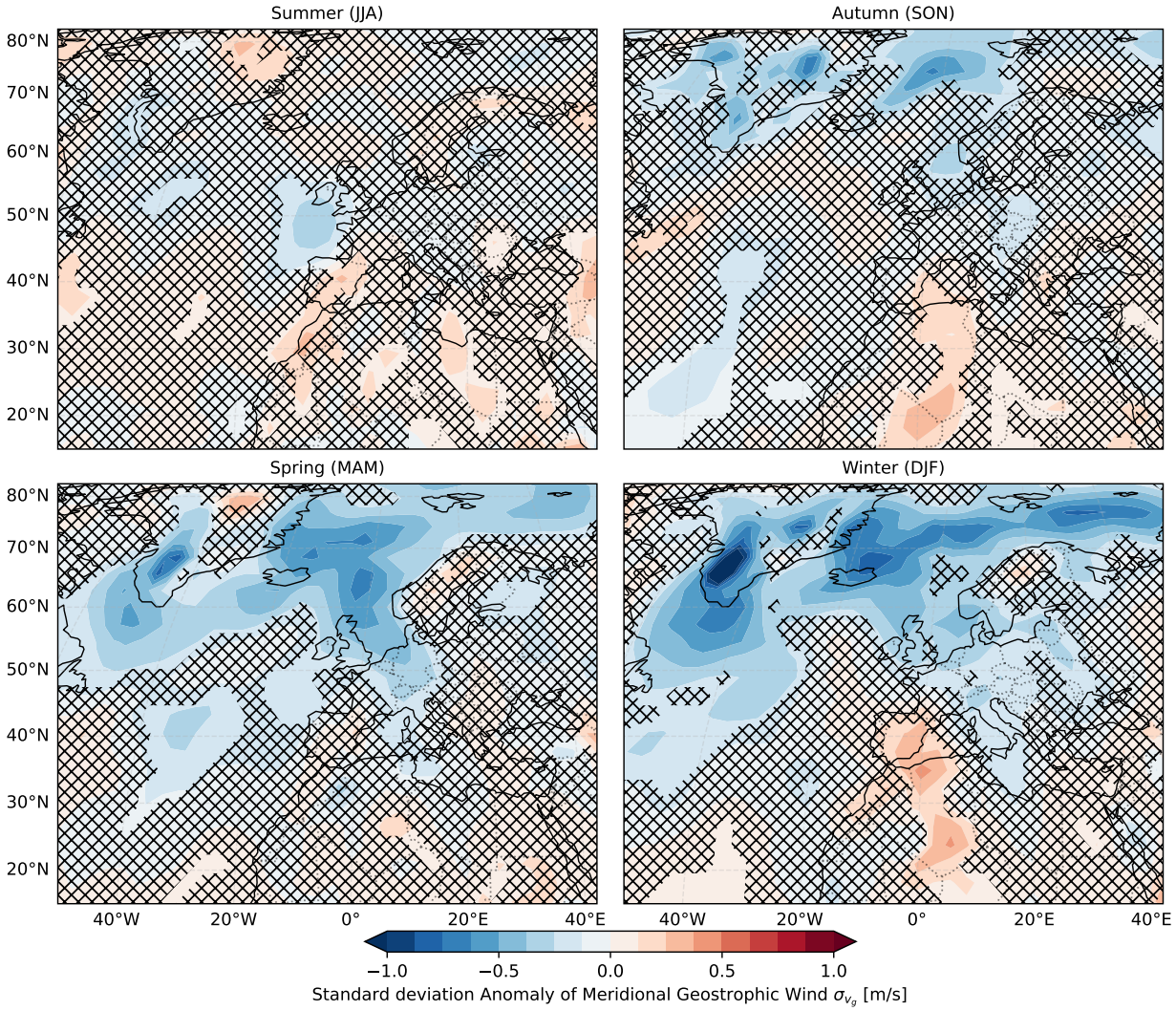


Figure B.14: Standard deviation anomaly of the meridional geostrophic wind between two periods representing distinct AMOC strength: years 150-250 (r70, low AMOC strength) and years 0-164 (control, high AMOC strength). Anomalies are computed as r70 minus control. Hatched area corresponds to nonsignificant area.

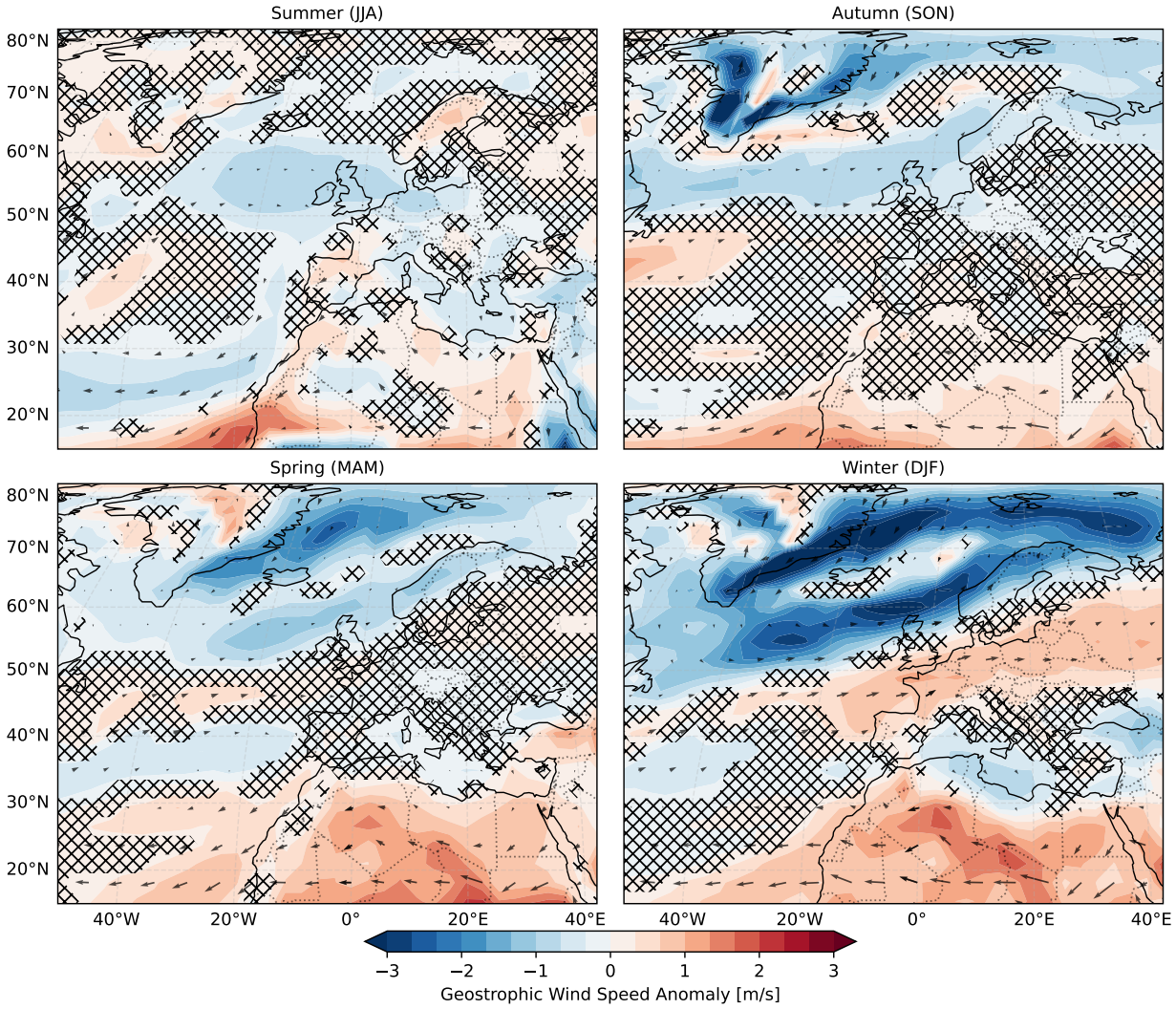


Figure B.15: Geostrophic wind speed anomaly between two periods representing distinct AMOC strength: years 150-250 (r70, low AMOC strength) and years 0-164 (control, high AMOC strength). Anomalies are computed as r70 minus control. Black arrows are the wind vectors of r70. Hatched area corresponds to nonsignificant area.

Bibliography

[1] IPCC. *Climate Change 2021: The Physical Science Basis. Contribution of Working Group I to the Sixth Assessment Report of the Intergovernmental Panel on Climate Change*. Ed. by V. Masson-Delmotte et al. Cambridge, United Kingdom and New York, NY, USA: Cambridge University Press, 2021. URL: https://www.ipcc.ch/report/ar6/wg1/.

[2] Stefan Rahmstorf. "Is the Atlantic overturning circulation approaching a tipping point?" In: *Oceanography* 37.3 (2024), pp. 16–29. URL: https://www.jstor.org/stable/pdf/27333920.pdf.

[3] William E Johns et al. "Towards two decades of Atlantic Ocean mass and heat transports at 26.5 N". In: *Philosophical Transactions of the Royal Society A: Mathematical, Physical and Engineering Sciences* 381.2262 (2023). URL: https://royalsocietypublishing.org/rsta/article/381/2262/20220188/41344.

[4] Laura C Jackson et al. "The evolution of the North Atlantic meridional overturning circulation since 1980". In: *Nature Reviews Earth & Environment* 3.4 (2022), pp. 241–254. URL: https://www.nature.com/articles/s43017-022-00263-2.pdf.

[5] Bette L Otto-Bliesner and Esther C Brady. "The sensitivity of the climate response to the magnitude and location of freshwater forcing: last glacial maximum experiments". In: *Quaternary Science Reviews* 29.1-2 (2010), pp. 56–73. URL: https://www.sciencedirect.com/science/article/pii/S0277379109002340?casa_token=K6XaN50eiWQAAAAA:rLJibMlOSjbc9PgjSAfC1R9XkFYFHOmTFHlrmfMEIAeC6yRSbYrzY--Jcl9ug8sCmsp_4Y20qjg.

[6] Wei Liu et al. "On the stability of the Atlantic meridional overturning circulation during the last deglaciation". In: *Climate Dynamics* 44.5 (2015), pp. 1257–1275. URL: https://link.springer.com/content/pdf/10.1007/s00382-014-2153-1.pdf.

[7] Eleanor Frajka-Williams et al. "Atlantic meridional overturning circulation: Observed transport and variability". In: *Frontiers in Marine Science* 6 (2019), p. 260. URL: https://www.frontiersin.org/journals/marine-science/articles/10.3389/fmars.2019.00260/pdf.

[8] LC Jackson et al. "Global and European climate impacts of a slowdown of the AMOC in a high resolution GCM". In: *Climate dynamics* 45.11 (2015), pp. 3299–3316. URL: https://correctiv.org/wp-content/uploads/2021/09/Jackson-et-al._2015_Global-and-European-climate-impacts-of-a-slowdown-of-the-AMOC-in-a-high-resolution-GCM.pdf.

[9] Felix Schaumann and Eduardo Alastrué de Asenjo. "Weakening AMOC reduces ocean carbon uptake and increases the social cost of carbon". In: *Proceedings of the National Academy of Sciences* 122.9 (2025), e2419543122. URL: https://www.pnas.org/doi/pdf/10.1073/pnas.2419543122.

[10] Scott C Doney et al. “Ocean acidification: the other CO2 problem”. In: *Annual review of marine science* 1 (2009), pp. 169–192. URL: https://digitalcommons.law.uw.edu/cgi/viewcontent.cgi?article=1055&context=wjelp.

[11] Yifei Fan et al. “Disagreement on the North Atlantic cold blob formation mechanisms among climate models”. In: *Journal of Climate* 37.16 (2024), pp. 4061–4078. URL: https://journals.ametsoc.org/view/journals/clim/37/16/JCLI-D-23-0654.1.xml.

[12] Lavinia Patara and Claus W Böning. “Abyssal ocean warming around Antarctica strengthens the Atlantic overturning circulation”. In: *Geophysical Research Letters* 41.11 (2014), pp. 3972–3978. URL: https://agupubs.onlinelibrary.wiley.com/doi/pdfdirect/10.1002/2014GL059923.

[13] Tiago Carrilho Biló et al. “Weakening of the Atlantic meridional overturning circulation abyssal limb in the North Atlantic”. In: *Nature geoscience* 17.5 (2024), pp. 419–425. URL: https://www.nature.com/articles/s41561-024-01422-4.pdf.

[14] Kevin E Trenberth et al. “Estimates of the global water budget and its annual cycle using observational and model data”. In: *Journal of Hydrometeorology* 8.4 (2007), pp. 758–769. URL: https://journals.ametsoc.org/view/journals/hydr/8/4/jhm600_1.xml.

[15] T Petit et al. “Evaluation of a Reduced RAPID Array for Measuring the AMOC”. In: *Journal of Geophysical Research: Oceans* 130.11 (2025), e2025JC023093. URL: https://agupubs.onlinelibrary.wiley.com/doi/pdf/10.1029/2025JC023093.

[16] Lettie A Roach et al. “The impact of winds on AMOC in a fully-coupled climate model”. In: *Geophysical Research Letters* 49.24 (2022), e2022GL101203. URL: https://agupubs.onlinelibrary.wiley.com/doi/pdfdirect/10.1029/2022GL101203.

[17] Rong Zhang et al. “A review of the role of the Atlantic meridional overturning circulation in Atlantic multidecadal variability and associated climate impacts”. In: *Reviews of Geophysics* 57.2 (2019), pp. 316–375. URL: https://agupubs.onlinelibrary.wiley.com/doi/pdfdirect/10.1029/2019RG000644.

[18] Wilbert Weijer et al. “Stability of the Atlantic Meridional Overturning Circulation: A review and synthesis”. In: *Journal of Geophysical Research: Oceans* 124.8 (2019), pp. 5336–5375. URL: https://agupubs.onlinelibrary.wiley.com/doi/pdf/10.1029%2F2019JC015083.

[19] Hugues Goosse. *Climate system dynamics and modeling*. Cambridge University Press, 2015. URL: https://books.google.com/books?hl=fr&lr=&id=aCFTCgAAQBAJ&oi=fnd&pg=PR11&dq=Climate+system+dynamics+and+modelling&ots=9uuUGlbZd9&sig=hIPY0_C-CD5x5u2BfzcRLOXn2Uk.

[20] Gaurav Madan et al. “The weakening AMOC under extreme climate change”. In: *Climate Dynamics* 62.2 (2024), pp. 1291–1309. URL: https://link.springer.com/content/pdf/10.1007/s00382-023-06957-7.pdf.

[21] Katinka Bellomo et al. “Future climate change shaped by inter-model differences in Atlantic meridional overturning circulation response”. In: *Nature Communications* 12.1 (2021), p. 3659. URL: https://www.nature.com/articles/s41467-021-24015-w.pdf.

[22] Peter Ditlevsen and Susanne Ditlevsen. “Warning of a forthcoming collapse of the Atlantic meridional overturning circulation”. In: *Nature Communications* 14.1 (2023), pp. 1–12. URL: https://www.nature.com/articles/s41467-023-39810-w/naz.

[23] Giovanni Sgubin et al. “Abrupt cooling over the North Atlantic in modern climate models”. In: *Nature communications* 8.1 (2017), p. 14375. URL: https://www.nature.com/articles/ncomms14375.pdf.

[24] Henk A Dijkstra and René M van Westen. “The Probability of an AMOC Collapse Onset in the Twenty-First Century”. In: *Annual Review of Marine Science* 18 (2025). URL: https://www.annualreviews.org/content/journals/10.1146/annurev-marine-040324-024822?crawler=true&mimetype=application/pdf.

[25] Emma JV Smolders, René M van Westen, and Henk A Dijkstra. “Probability estimates of a 21st century AMOC collapse”. In: *arXiv preprint arXiv:2406.11738* (2024). URL: https://arxiv.org/abs/2406.11738.

[26] James W Hurrell et al. “An overview of the North Atlantic oscillation”. In: *Geophysical monograph-American geophysical union* 134 (2003), pp. 1–36. URL: https://www.researchgate.net/profile/Geir-Ottersen/publication/304578504_An_overview_of_the_North_Atlantic_Oscillation/links/57c4146308aee465796bff48/An-overview-of-the-North-Atlantic-Oscillation.pdf.

[27] Laura Zubiate et al. “Spatial variability in winter NAO–wind speed relationships in western Europe linked to concomitant states of the East Atlantic and Scandinavian patterns”. In: *Quarterly Journal of the Royal Meteorological Society* 143.702 (2017), pp. 552–562. URL: https://rmets.onlinelibrary.wiley.com/doi/pdfdirect/10.1002/qj.2943.

[28] Maksim Valentinovich Kalashnik, Mikhail Vasil’evich Kurgansky, Otto Guramovich Chkhetiani, et al. “Baroclinic instability in geophysical fluid dynamics”. In: *Phys.-Usp* 65.10 (2022), pp. 1039–1070. URL: https://www.researchgate.net/profile/O-Chkhetiani/publication/354187377_Baroclinic_instability_in_geophysical_hydrodynamics/links/645b8e4e6090c43d0f5e855a/Baroclinic-instability-in-geophysical-hydrodynamics.pdf.

[29] M Jeroen Molemaker, James C McWilliams, and Irad Yavneh. “Baroclinic instability and loss of balance”. In: *Journal of physical oceanography* 35.9 (2005), pp. 1505–1517. URL: https://journals.ametsoc.org/view/journals/phoc/35/9/jpo2770.1.pdf.

[30] W Liu et al. *Climate impacts of a weakened Atlantic meridional overturning circulation in a warming climate. Sci. Adv., 6, eaaz4876.* 2020. URL: https://www.science.org/doi/pdf/10.1126/sciadv.aaz4876.

[31] René M Van Westen et al. “Changing European hydroclimate under a collapsed AMOC in the Community Earth System Model”. In: *Hydrology and Earth System Sciences* 29.22 (2025), pp. 6607–6630. URL: https://hess.copernicus.org/articles/29/6607/2025/hess-29-6607-2025.pdf.

[32] Katinka Bellomo et al. “Impacts of a weakened AMOC on precipitation over the Euro-Atlantic region in the EC-Earth3 climate model”. In: *Climate Dynamics* 61.7 (2023), pp. 3397–3416. URL: https://link.springer.com/content/pdf/10.1007/s00382-023-06754-2.pdf.

[33] Laura C Jackson et al. “Understanding AMOC stability: The North Atlantic hosing model intercomparison project”. In: *Geoscientific Model Development* 16.7 (2023), pp. 1975–1995. URL: https://gmd.copernicus.org/articles/16/1975/2023/gmd-16-1975-2023.html.

[34] Veronika Eyring et al. "Overview of the Coupled Model Intercomparison Project Phase 6 (CMIP6) experimental design and organization". In: *Geoscientific Model Development* 9.5 (2016), pp. 1937–1958. URL: https://gmd.copernicus.org/articles/9/1937/2016/gmd-9-1937-2016.pdf.

[35] Neil C Swart et al. "The Canadian earth system model version 5 (CanESM5. 0.3)". In: *Geoscientific Model Development* 12.11 (2019), pp. 4823–4873. URL: https://gmd.copernicus.org/articles/12/4823/2019/gmd-12-4823-2019.html.

[36] Olivier Boucher et al. "Presentation and evaluation of the IPSL-CM6A-LR climate model". In: *Journal of Advances in Modeling Earth Systems* 12.7 (2020), e2019MS002010. URL: https://agupubs.onlinelibrary.wiley.com/doi/pdfdirect/10.1029/2019ms002010.

[37] Gokhan Danabasoglu et al. "The community earth system model version 2 (CESM2)". In: *Journal of Advances in Modeling Earth Systems* 12.2 (2020), e2019MS001916. URL: https://agupubs.onlinelibrary.wiley.com/doi/pdf/10.1029/2019MS001916.

[38] Keith D Williams et al. "The Met Office global coupled model 3.0 and 3.1 (GC3. 0 and GC3. 1) configurations". In: *Journal of Advances in Modeling Earth Systems* 10.2 (2018), pp. 357–380. URL: https://agupubs.onlinelibrary.wiley.com/doi/pdfdirect/10.1002/2017ms001115.

[39] Amar Halifa-Marín et al. "Too-stable North Atlantic climate system in CMIP6 experiments undermines precipitation projections in Europe". In: *Quarterly Journal of the Royal Meteorological Society* 151.771 (2025), e4999. URL: https://rmets.onlinelibrary.wiley.com/doi/pdf/10.1002/qj.4999.

[40] René M van Westen and Michiel LJ Baatsen. "European temperature extremes under different AMOC scenarios in the community Earth system model". In: *Geophysical Research Letters* 52.12 (2025), e2025GL114611. URL: https://agupubs.onlinelibrary.wiley.com/doi/pdf/10.1029/2025GL114611.

[41] Wei Liu and Alexey Fedorov. "Interaction between Arctic sea ice and the Atlantic meridional overturning circulation in a warming climate". In: *Climate Dynamics* 58.5 (2022), pp. 1811–1827. URL: https://link.springer.com/content/pdf/10.1007/s00382-021-05993-5.pdf.

[42] Andrew P Schurer et al. "Role of multi-decadal variability of the winter North Atlantic Oscillation on Northern Hemisphere climate". In: *Environmental Research Letters* 18.4 (2023), p. 044046. URL: https://iopscience.iop.org/article/10.1088/1748-9326/acc477/pdf.

[43] Rasmus A Pedersen et al. "The impact of regional Arctic sea ice loss on atmospheric circulation and the NAO". In: *Journal of Climate* 29.2 (2016), pp. 889–902. URL: https://journals.ametsoc.org/view/journals/clim/29/2/jcli-d-15-0315.1.pdf.

[44] Andrea Vito Vacca et al. "On the role of AMOC weakening in shaping wintertime Euro-Atlantic atmospheric circulation: A. Vito Vacca et al." In: *Climate Dynamics* 63.6 (2025), p. 273. URL: https://link.springer.com/content/pdf/10.1007/s00382-025-07747-z.pdf.

[45] René M Van Westen, Michael Kliphuis, and Henk A Dijkstra. "Physics-based early warning signal shows that AMOC is on tipping course". In: *Science advances* 10.6 (2024), eadk1189. URL: https://www.science.org/doi/pdf/10.1126/sciadv.adk1189?.

[46] Dietmar Dommenget. "The ocean's role in continental climate variability and change". In: *Journal of Climate* 22.18 (2009), pp. 4939–4952. URL: https://journals.ametsoc.org/downloadpdf/view/journals/clim/22/18/2009jcli2778.1.pdf.

[47] Virna L Meccia et al. "Extreme cold events in Europe under a reduced AMOC". In: *Environmental Research Letters* 19.1 (2024), p. 014054. URL: https://iopscience.iop.org/article/10.1088/1748-9326/ad14b0/pdf.

[48] Casey R Patrizio et al. "Enhanced decadal variance in Nordic Seas with AMOC weakening in CESM". In: *Geophysical Research Letters* 53.8 (2026), e2025GL118635. URL: https://agupubs.onlinelibrary.wiley.com/doi/pdf/10.1029/2025GL118635.

[49] James W Hurrell and Clara Deser. "North Atlantic climate variability: the role of the North Atlantic Oscillation". In: *Journal of marine systems* 79.3-4 (2010), pp. 231–244. URL: https://www.sciencedirect.com/science/article/pii/S0924796309003224?casa_token=UR4adWZ-FwIAAAAA:jMmlZ4Z9aqxvAPxxuPkFXfP--1SIZUJcJTO1tBTjAEF8ZKvzA6v4P_ratkRXe1izAkSgHoCYyVQ.

[50] Qinxue Gu et al. "Wide range of possible trajectories of North Atlantic climate in a warming world". In: *Nature communications* 15.1 (2024), p. 4221. URL: https://www.nature.com/articles/s41467-024-48401-2.pdf.

UNIVERSITE CATHOLIQUE DE LOUVAIN

Faculté des sciences

Place des sciences, 2 bte L6.06.01, 1348 Louvain-la-Neuve, Belgique — **www.uclouvain.be/sc**